

**CHARACTERIZATION OF AXIAL TURBINES FOR PRESSURE GAIN
COMBUSTION**

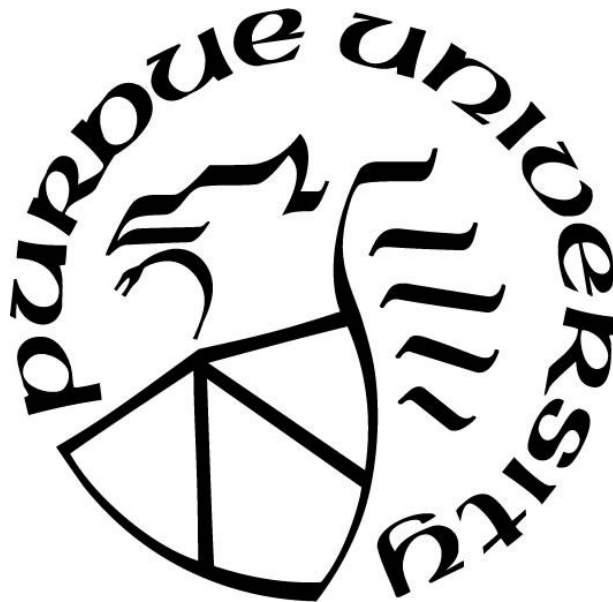
by
Zhe Liu

A Dissertation

Submitted to the Faculty of Purdue University

In Partial Fulfillment of the Requirements for the degree of

Doctor of Philosophy



School of Mechanical Engineering

West Lafayette, Indiana

December 2019

**THE PURDUE UNIVERSITY GRADUATE SCHOOL
STATEMENT OF COMMITTEE APPROVAL**

Dr. Guillermo Paniagua

School of Mechanical Engineering

Dr. Terrence Meyer

School of Mechanical Engineering

Dr. Alina Alexeenko

School of Aeronautics and Astronautics

Dr. Sally Bane

School of Aeronautics and Astronautics

Dr. Jose Ramon Serrano

Polytechnic University of Valencia

Dr. Donald Ferguson

National Energy Technology Laboratory

Approved by:

Dr. Eckhard Groll

Head of the Graduate Program

To my parents for their love. To myself for the perseverance.

ACKNOWLEDGMENTS

I would like to thank my Parents, Hongfen Sun and Degang Liu, for their love and support on my graduate study in United States. I'm proud to be their son.

I would like to thank my advisor, Guillermo Paniagua, for his patient and professional advisory. The PhD journey could not be a success, without the full support of Guillermo. You made the right decision in selecting PhD candidates back to 2015.

I would like to thank my best teammate, James Braun, for his time spent with me, from the cubicle to the famous Zucrow Chaf 231. I could write a book for our interesting stories. I'll remember our jokes and funny messages. James when you go back to Belgium, make a statue of me in Brussels. I will do the same in China.

I would like to thank Valeria Andreoli and David Cuadrado, for their countless help on my PhD. Valeria cooks the best barbeque chicken in West Lafayette. I like them a lot.

I would like to thank Francisco Lozano, Jorge Saavedra, Paht Juangphanich, Udit Vyas, Lakshya Bhatnagar, Iman Rahbari, Nyansafo Aye-Addo, Swapnil Ingale, Yutao Zheng, Lukas Inhestern, Jorge Sousa, and Cis De Maesschalck, for their kind assistance on my PhD. Jorge, Papa, and Udit, we need to keep playing basketball. Ball is life.

I would like to thank Matthew Nichols, Jordan Fisher, Nick Long, Daniel Inman, Paul Clark, and Santiago Salinas. We don't have much time to talk to each other, but I'm happy to have you all stand by me.

I would like to thank my friend, Pei-yun Yeh, for her mental support. I will miss your dog Pocky. In the end, I would like to thank myself, for being persistent and positive during this PhD journey. I have encountered tough times, but I prevailed and continued this journey till the end.

TABLE OF CONTENTS

LIST OF TABLES	8
LIST OF FIGURES	9
NOMENCLATURE	15
ABSTRACT.....	19
1. INTRODUCTION	20
1.1 Literature Review of Pressure Gain Combustion	20
1.2 Research Objectives.....	22
1.2.1 Develop a compact expansion system	22
1.2.2 Develop an efficient expansion system	22
1.2.3 Develop flow measurement tools	23
1.3 Research Methodology	24
1.3.1 Develop a Supersonic Axial Turbine.....	24
1.3.2 Retrofit an Existing Subsonic Axial Turbine through Endwall Contouring.....	24
1.3.3 Develop Fast-response Multi-hole Directional Probes.....	25
1.4 Dissertation Outline	25
2. DEVELOPMENT OF A SUPERSONIC AXIAL TURBINE.....	27
2.1 Turbine Geometry and Boundary Conditions.....	27
2.1.1 Turbine Inlet Condition	27
2.1.2 Computational Domain.....	29
2.1.3 Grid Sensitivity.....	30
2.1.4 Steady State Performance	32
2.1.5 Periodic Convergence	32
2.2 Time-Resolved Analysis.....	34
2.2.1 Time-Resolved Stator Characterization.....	34
2.2.2 Influence of the Reduced Frequency and Amplitude	38
2.2.3 Time-Resolved Rotor Performance	39
2.2.4 Time-Resolved Turbine Stage Assessment	43
2.3 Performance Map.....	47
2.4 Unsteady Heat Transfer Assessment	48

2.4.1	Span-wise Heat Flux Fluctuations	49
2.4.2	Stream-wise Heat Flux Variation	51
2.4.3	Time-Resolved Adiabatic Wall Temperature	52
2.4.4	Budgeting of the Unsteady Heat Flux Mechanism	55
3.	RETROFIT AN EXISTING SUBSONIC AXIAL TURBINE WITH ENDWALL CONTOURING	58
3.1	Turbine Geometry and Boundary Conditions	58
3.1.1	Computational Domain	58
3.1.2	Grid Sensitivity	59
3.1.3	Time Step Convergence	60
3.1.4	Periodic Convergence	61
3.2	Endwall Contouring to Ingest High Subsonic Flow	62
3.2.1	Axisymmetric Endwall Contouring to Prevent Choking	62
3.2.2	Performance Analysis	63
3.3	Effect of Inlet Fluctuations on Efficiency and Damping	67
3.3.1	Horlock Estimation	68
3.3.2	URANS Stage Simulations: Mixing Plane Approach	69
3.3.3	URANS Stage Simulations: Full Unsteady Approach	73
3.4	Optimization Strategy	74
3.5	Results	76
3.5.1	Steady Optimization	76
3.5.2	Unsteady Optimization	78
3.5.3	Full Unsteady Assessment of Optimized Endwall Geometries	80
3.5.4	Engine Model with a Rotating Detonation Combustor and an Optimized Turbine Profile	82
3.6	Performance Map	83
3.7	Design of Experiments	84
3.7.1	Facility Introduction and Test Article Design	84
3.7.2	Proposed Measurement Techniques	87
3.7.2.1	Low-Frequency Measurements	87
3.7.2.2	High-Frequency Measurements	87

4. DEVELOPMENT OF FLOW MEASUREMENT TOOLS FOR EXPANSION SYSTEMS	88
4.1 Directional Probes for Pressure Measurements in Subsonic Flow	88
4.1.1 Probe Shape and Computational Domain	88
4.1.2 Grid Sensitivity	89
4.1.3 Unsteady Convergence Assessment	90
4.2 Probe Shape Characterization	91
4.3 Two-Dimensional Evaluation of Oval Probe Performance	99
4.4 Three-Dimensional Design	102
4.4.1 Angular Calibration of Probe	106
4.4.2 Unsteady Performance Assessment of Directional Probe	109
4.5 Biomimicry-Inspired Design to Attenuate Vortex Shedding Unsteadiness	111
5. CONCLUSION	113
REFERENCES	117
APPENDIX. SOLVER VALIDATION	127
PERMISSION LETTER	133
VITA	134
PUBLICATIONS	135

LIST OF TABLES

Table 2.1: Turbine geometric parameters at mean radius.....	30
Table 2.2: Evaluation of periodic convergence.	34
Table 2.3: Performance assessment and instantaneous rotor damping ($f=0.24$, $A=1$).....	43
Table 2.4: Instantaneous stage damping ($f=0.24$, $A=1$).	46
Table 2.5: Budgeting of the unsteady total pressure loss due to shock waves, viscous, mixing, and secondary flow across the stator and rotor ($f=0.24$, $A=1$).	47
Table 2.6: Comparison of the integral heat load between steady and unsteady simulations.....	52
Table 3.1: Turbine geometric parameters at mean radius.....	58
Table 3.2: Evaluation of turbine efficiency at steady state.....	64
Table 3.3: Budgeting of loss mechanism at steady state for EW2 and EW3.....	66
Table 3.4: Budgeting of loss mechanism operating at a total pressure fluctuation of $A=37.5\%$ for EW2 ($f=1.38$) and EW3 ($f=1.26$).	68
Table 3.5: Comparison of turbine efficiency for EW2 and EW3 between steady and full unsteady simulations.	74
Table 4.1: Total pressure recovery for two characterized probe shapes at two inlet Mach numbers.....	96
Table 4.2: Vortex shedding frequency in functions of inlet Mach numbers and yaw angles for two characterized probe shapes.	98
Table 4.3: Accuracy assessment of the calibration algorithm.	108
Table 4.4: Vortex shedding frequency evaluated by St-Re correlation for a Mach number of 0.3.	110
Table 5.1: Sutherland law parameters for viscosity and thermal conductivity of air.	129

LIST OF FIGURES

Figure 1.1. Development of expansion systems for RDCs.....	23
Figure 1.2. Development of flow measurement tools.....	23
Figure 2.1. a) Geometry of the RDC and nozzle. b) 3D optimized nozzle geometry.....	27
Figure 2.2. a) Instantaneous static temperature contour of the 2D RDC. Nozzle outlet profile: b) static pressure, c) static temperature, d) Mach number, and e) flow angle as a function of the azimuthal angle.	28
Figure 2.3. Turbine profile at mid-span: a) supersonic stator and b) supersonic rotor.....	29
Figure 2.4. a) Channel variation. b) Numerical grid with a close up of the stator trailing edge. .	30
Figure 2.5. a) Rotor relative total pressure loss in function of grid size. b) Torque in function of the convergence. Contour of relative total pressure at rotor outlet for the c) medium mesh and d) fine mesh. e) Local discretization error of the medium mesh.....	31
Figure 2.6. Steady flow field of the supersonic turbine at midspan for an inlet Mach number of 2.	32
Figure 2.7. URANS stator simulation exposed to oblique shocks for three consecutive phases at mid-span ($f=0.24$, $A=1$): a) Mach contour and b) total pressure contour. c) Close up of the instantaneous shock pattern during phase 3.....	35
Figure 2.8. Instantaneous contour of stator outlet at phase 3: a) Mach number, b) total pressure, and c) total temperature ($f=0.24$, $A=1$).....	37
Figure 2.9. Instantaneous stator fluctuations in function of the azimuthal angle at phase 3: a) flow angle, b) static pressure, c) Mach number, and d) static temperature ($f=0.24$, $A=1$).....	38
Figure 2.10. Stator total pressure loss in function of reduced frequency and non-dimensional amplitude.....	39
Figure 2.11. a) Flow field of a URANS rotor simulation at mid-span for three consecutive phases ($f=0.24$, $A=1$). b) Close up of the instantaneous shock pattern during phase 3.	40
Figure 2.12. Instantaneous contour of rotor outlet at phase 3: a) relative Mach number, b) relative total pressure, and c) relative total temperature ($f=0.24$, $A=1$).	41
Figure 2.13. Instantaneous rotor fluctuations in function of the azimuthal angle at phase 3: a) relative flow angle, b) static pressure, c) relative Mach number, and d) static temperature ($f=0.24$, $A=1$).	42
Figure 2.14. a) Flow field of a URANS stage simulation at mid-span exposed to oblique shocks for three consecutive phases. b) Close up of the instantaneous shock pattern during phase 2. c) 3D flow structure within the stage during phase 2. d) Static temperature of stator vanes and rotor blades for three phases ($f=0.24$, $A=1$).	44

Figure 2.15. Instantaneous stage fluctuations in function of the azimuthal angle: a) flow angle, b) static pressure, c) Mach number, and d) static temperature ($f=0.24$, $A=1$).....	45
Figure 2.16. a) Instantaneous flow field of the URANS stage simulation at midspan ($f=0.24$, $A=1$). b) Frequency spectrum of static pressure at the stator inlet and rotor inlet.	46
Figure 2.17. a) Total-to-total pressure ratio in function of the corrected mass flow. b) Non-dimensional total temperature difference in function of the product of corrected mass flow and corrected speed.....	48
Figure 2.18. Instantaneous heat flux pattern for a wall temperature of 1800K.	49
Figure 2.19. At a wall temperature of 1400K: a) Snapshot of the stator and rotor. Span-wise heat flux variation at: b) stator leading edge and c) rotor leading edge.	50
Figure 2.20. At a wall temperature of 1400K: a) Snapshot of the stator and rotor. Span-wise heat flux variation at: b) stator trailing edge and c) rotor trailing edge.....	50
Figure 2.21. At a wall temperature of 1400K: stream-wise heat flux variation at mid-span of a) stator and b) rotor.....	51
Figure 2.22. Stator leading edge at mid-span: a) Time-resolved heat flux. Linear interpolation of b) the instantaneous heat flux and c) at all time instants. d) Time-resolved adiabatic wall temperature.	53
Figure 2.23. Verification of the adiabatic wall temperature at mid-span of a) stator and b) rotor.	53
Figure 2.24. Instantaneous adiabatic wall temperature.....	54
Figure 2.25. Stator at mid-span for a wall temperature of 1400K: a) Measurement locations. At PS ₁ : b) Unsteady static pressure and unsteady adiabatic heat transfer coefficient and c) unsteady Reynolds number and unsteady adiabatic heat transfer coefficient.....	56
Figure 2.26. Stator at mid-span for a wall temperature of 1400K: Contribution to Q' at a) PS ₁ and b) PS ₂	56
Figure 2.27. Rotor at mid-span for a wall temperature of 1400K: a) Measurement locations. b) Contribution to Q' at PS ₃	57
Figure 3.1. a) Computational domain of the turbine stage for a Mach 0.6 inflow. A close-up view of the b) stator leading edge and c) rotor trailing edge.	59
Figure 3.2. a) Rotor outlet total temperature in function of the cell count. b) Log-log plot of the numerical extrapolated error of rotor outlet total temperature in function of the representative grid size. c) Evolution of the mass flow rate at stator inlet and rotor outlet.	60
Figure 3.3. Fluctuation of a) total pressure at $f=100\text{Hz}$ and $A=15\%$ and b) total temperature at $A=3.5\%$ imposed at the stator inlet.....	61
Figure 3.4. One period ($f=1\text{kHz}$, $A=15\%$) with a) 20 vs. 30 discretized time steps and b) 30 vs. 60 discretized time steps.	61

Figure 3.5. a) Cross sections of the three different endwall designs. b) Throat-to-local area ratio. c) Throat-to-inlet area ratio in function of the inlet Mach number.	63
Figure 3.6. a) EW1 choked at $M1=0.3$. b) Started operation: EW2; c) EW1 choked at $M1=0.6$. d) Started operation: EW3. e) Mach number distribution along the midpitch for EW1 and EW2. f) Mach number distribution along the mid-pitch for EW1 and EW3.....	66
Figure 3.7. Minor flow separation in EW2: a) and b). Increased flow separation in EW3: c) and d).	67
Figure 3.8. Horlock estimation in function of amplitude and reduced frequency for a) EW2 and b) EW3.	69
Figure 3.9. Flow field of a URANS stage simulation (mixing plane approach) of EW2 exposed to a total pressure fluctuation ($A=37.5%$, $f=0.15$).	70
Figure 3.10. Turbine efficiency in function of amplitude and reduced frequency for a) EW2 and b) EW3.	71
Figure 3.11. Stage damping in function of reduced frequency and amplitude for a) EW2 and b) EW3.	72
Figure 3.12. Instantaneous stator axial velocity contour of EW3 in function of the reduced frequency at a) $A=15%$ and b) $A=37.5%$	72
Figure 3.13. Flow field of a full unsteady stage simulation of EW2 exposed to a total pressure fluctuation ($A=37.5%$, $f=1.38$).....	73
Figure 3.14. Multi-step optimization strategy.....	75
Figure 3.15. Turbine channel endwall parametrization for the steady optimization.	76
Figure 3.16. Pareto front of the steady optimization.	77
Figure 3.17. a) Axial velocity contour of the baseline stator. b) Pareto front colored by the separation intensity.	78
Figure 3.18. a) Pareto front colored by stage damping. b) Total pressure traces from the stator inlet and rotor outlet.....	79
Figure 3.19. Meridional view of a) baseline stator, b) profile 3 in Fig. 3.16, and c) profile 2 in Fig. 3.18a. d) Throat-to-local area ratio in function of the normalized surface curvilinear coordinate.....	80
Figure 3.20. Instantaneous axial velocity contour at $f=0.23$ and $A=37.5%$ of a) profile 3 in Fig. 3.16 and b) profile 2 in Fig. 3.18a.....	80
Figure 3.21. a) Flow field from a full unsteady turbine simulation (profile 3, Fig. 7) at $A=37.5%$ and $f=0.23$. b) Turbine efficiencies of the baseline and selected optimized configurations.....	81
Figure 3.22. a) Engine model. b) Pressure gain in function of the overall compression ratio of the engine.....	82
Figure 3.23. Thermal efficiency (a) and thrust (b) in function of pressure ratio.	83

Figure 3.24. a) Total-to-total pressure ratio in function of the corrected mass flow. b) Turbine efficiency in function of the product of corrected mass flow and corrected speed.	84
Figure 3.25. PETAL facility linear test section.	85
Figure 3.26. a) Frontal view of the test article. b) Top view of the pressure tappings.	86
Figure 3.27. a) Test article assembled in the linear test section. b) Flow field of the test section. c) Diffuser end: snapshot of flow separation.	86
Figure 3.28 Static pressure distribution along the test section.....	86
Figure 4.1. a) Trapezoidal probe, and b) the computational domain of the trapezoidal probe. c) Oval probe, and d) the computational domain of the oval probe.....	89
Figure 4.2. Non-dimensional pressure at point ‘c’ on the oval probe in function of grid cell amount.....	90
Figure 4.3. Non-dimensional pressure at point ‘c’ on the oval probe in function of the turbulence model.....	90
Figure 4.4. a) Non-dimensional pressure retrieved by point ‘a’ on the trapezoidal probe in function of periodic cycles. b) Zoomed portion of the last 7 periodic cycles. c) Overlap of the last 3 cycles.....	91
Figure 4.5. Steady Mach contours in function of yaw angles for an inlet Mach number of 0.3 and two characterized probe shapes: a) trapezoidal, and b) oval.	92
Figure 4.6. Non-dimensional pressure as functions of the probe curvilinear coordinate and yaw angles for an inlet Mach number of 0.3 and two characterized probe shapes: a) trapezoidal, and b) oval.	93
Figure 4.7. Iso-contours of C_{pi} in functions of yaw angles and probe coordinate for an inlet Mach number of 0.3 and two characterized probe shapes: a) trapezoidal, and b) oval. Angle sensitivity as a function of yaw angles for an inlet Mach number of 0.3 and two characterized probe shapes evaluated at c) point ‘a’, and d) point ‘c’.....	93
Figure 4.8. Steady Mach contours in function of yaw angles for an inlet Mach number of 0.75 and two characterized probe shapes: a) trapezoidal, and b) oval.....	94
Figure 4.9. Non-dimensional pressure as functions of the probe curvilinear coordinate and yaw angles for an inlet Mach number of 0.75 and two characterized probe shapes: a) trapezoidal, and b) oval.	95
Figure 4.10. Iso-contours of C_{pi} in functions of yaw angles and probe coordinate for an inlet Mach number of 0.75 and two characterized probe shapes: a) trapezoidal, and b) oval. Angle sensitivity as a function of yaw angles for an inlet Mach number of 0.75 and two characterized probe shapes evaluated at c) point ‘a’, and d) point ‘c’.....	95
Figure 4.11. Instantaneous vortex shedding at two time frames for an inlet Mach number of 0.3 and 0 yaw angle downstream of the two characterized probe shapes: a) trapezoidal, and b) oval.	97

Figure 4.12. Instantaneous vortex shedding at two time frames for an inlet Mach number of 0.75 and 0 yaw angle downstream of the two characterized probe shapes: a) trapezoidal, and b) oval.	97
Figure 4.13. MinMax in function of probe coordinate for a) an inlet Mach number of 0.3 and 0 yaw angle, b) an inlet Mach number of 0.3 and -12° yaw angle, c) an inlet Mach number of 0.75 and 0 yaw angle, d) an inlet Mach number of 0.75 and -12° yaw angle.	99
Figure 4.14. a) Computation domain. b) Oval probe with pressure tapings.	100
Figure 4.15. Frequency spectrum for an inlet Mach number of 0.3 retrieved by a) downstream velocity sensor, b) recessed sensor 1, c) recessed sensor 2. Frequency spectrum for an inlet Mach number of 0.6 retrieved by d) downstream velocity sensor, e) recessed sensor 1, f) recessed sensor 2.	101
Figure 4.16. a) Non-dimensional pressure retrieved by reference and recessed sensor for an inlet Mach number of 0.3. b) Transfer function identification.	102
Figure 4.17. a) 3D design of the directional probe. b) Internal structures of the pressure tapings.	103
Figure 4.18. a) 3D computational domain. b) Top view, and c) front view of the computational domain. d) Numerical grid. e) 2D mid-cut of the numerical grid.	104
Figure 4.19. a) Convention of yaw and pitch angle. b) Steady Mach contours in function of yaw angle for an inlet Mach number of 0.3 and 0 pitch angle.	105
Figure 4.20. C_{pk} in function of yaw and pitch angles for an inlet Mach number of 0.3 evaluated at: a) Tube 1, b) Tube 2, c) Tube 3, d) Tube 4, and e) Tube 5.	106
Figure 4.21. Data reduction algorithm [73].	107
Figure 4.22. Contour of pressure coefficient in function of yaw and pitch angle.	108
Figure 4.23. Instantaneous vortex shedding downstream of the directional probe at two time frames for an inlet Mach number of 0.3.	109
Figure 4.24. Frequency spectrum for an inlet Mach number of 0.3 retrieved by a) Kulite 1, b) Kulite 2, c) Kulite 3, d) Kulite 4, and e) Kulite 5.	110
Figure 4.25. a) Schematic sketch of the line-cavity system. b) Resonance frequency of all five tube-cavity systems inside the directional probe.	111
Figure 4.26. Whisker probe: a) Frontal view and b) Rear view. c) Comparison of the frequency spectrum retrieved by Kulites between the cylindrical probe and the whisker probe.	112
Figure 5.1. At mid-span: a) the Mach contour of the transonic vane. b) Isentropic Mach number distribution.	130
Figure 5.2. a) Steady Mach contour. b) Comparison of skin friction and c) wall static pressure.	130

Figure 5.3. a) ONERA shock tube [27]. b) Numerical grid of the shock tube with a zoomed view of line-cavity schematic sketch. c) Normalized pressure from the reference and recessed sensor. d) Resonance frequency of different tube-cavity configurations..... 132

NOMENCLATURE

α		Absolute flow angle [°]
a		Sonic speed [m/s]
A		Amplitude [-]
\bar{A}		Non-dimensional amplitude [-]
β		Relative flow angle [°]
C		Chord length [mm]
C_p	Constant pressure specific heat [J/(kg.K)]	
$ \Delta C_p $		Angle sensitivity [-]
D		Probe diameter [mm]
D_t		Tube diameter [mm]
F		Thrust [N]
f		Excitation frequency [kHz]
\bar{f}		Reduced frequency [-]
f_A	Fuzzy set for DFT amplitude convergence [-]	
f_m	Fuzzy set for time-mean convergence [-]	
f_n		Resonance frequency [kHz]
f_s	Fuzzy set for convergence of signal shape [-]	
f_ϕ	Fuzzy set for DFT phase convergence [-]	
g		Pitch [mm]
h		Channel height [mm]
L		Tube length [mm]
\dot{m}		Mass flow rate [kg/s]
M		Absolute Mach number [-]
M_{rel}		Relative Mach number [-]
\bar{m}		Corrected mass flow [$ms^2 K^{0.5}$]
n		Number of rotor passages
\bar{n}		Corrected speed [$s^{-1} K^{0.5}$]
$\eta_{Horlock}$		Horlock estimation [-]

$\eta_{\text{Thermodynamic}}$	Thermodynamic efficiency [-]
P_s	Static pressure [bar]
P_0	Total pressure [bar]
Q_l	Lower heating value [J/kg]
R	Radius [mm]
Re	Reynolds number [-]
S	Area [mm ²]
SS	Probe curvilinear coordinate [-]
St	Strouhal number [-]
t	Time [s]
t_{periodic}	Time to form a periodic cycle [s]
τ	Torque [N.m]
T_s	Static temperature [K]
T_0	Total temperature [K]
U	Rotor peripheral speed [m/s]
V	Absolute velocity [m/s]
V_c	Cavity volume [mm ³]
V_t	Tube volume [mm ³]
W	Relative velocity [m/s]
ω	Angular velocity [rad/s]
θ	Azimuthal angle [°]
ξ	Damping [-]
x	Design parameter
y^+	Non-dimensional wall distance [-]
Y	Total pressure loss coefficient [-]
λ	Normalized torque residual [-]
ε	Local grid discretization error [-]
ζ	Kinetic energy loss coefficient [-]

Abbreviations

AR	Area ratio [-]
----	----------------

CADO	Computed aided design and optimization
CCF	Cross correlation coefficient [-]
CFD	Computational fluid dynamics [-]
DFT	Discrete Fourier transform
DoE	Design of experiments
FFT	Fast Fourier transfer
GCI	Grid convergence index [-]
k- ϵ	Standard k-epsilon
k- ω	k-omega
MOC	Method of characteristics
PDC	Pulse detonation combustor
RDC	Rotating detonation combustor
RANS	Reynolds-Averaged Navier-Stokes
RMSD	Root mean square deviation [-]
S-A	Spalart-Allmaras
SST	Shear stress transport
T-MATS	The toolbox of the modeling and analysis of thermodynamic systems
URANS	Unsteady Reynolds-Averaged Navier-Stokes

Subscripts

ax	Axial direction
c	Chord
current	Current sinusoidal cycle
f	fuel
h	Hub
i	Grid point
in	Probe inlet
is	Isentropic
j	Measurement location on 2D probe
k	Measurement location on 3D probe

m	Mean value
previous	Previous sinusoidal cycle
R	Rotor
S	Stator
sensor	Sensor location
t	Tip
0	Engine inlet
1	Stator inlet
2	Stator outlet / Rotor inlet
3	Rotor outlet
5	Engine outlet

ABSTRACT

Pressure gain combustion is beneficial for engine cycle efficiency, compactness, and less emissions. In this dissertation, two classes of fluid expansion systems were developed to harness power from the high-speed flow delivered by the pressure gain combustor: a compact expansion system and an efficiency expansion system. In addition, a new class of pressure probes for expansion systems is developed.

A numerical methodology is carried out to design and characterize these expansion devices and measurement systems via steady and unsteady Reynolds Averaged Navier Stokes simulations. Firstly, the compact expansion system is achieved by developing a supersonic axial turbine. Performance of the supersonic axial turbine exposed to fluctuations from a nozzle downstream of a rotating detonation combustor is assessed with an increased level of complexity, including time-resolved stator, time-resolved rotor, and time-resolved turbine stage characterization. Power extraction, damping of fluctuations, and loss budgeting are evaluated. Unsteady heat transfer assessment is performed to investigate the convective heat flux distribution and decomposition. A performance map is constructed to explore the operating limit. Afterwards, the efficient expansion system is achieved by retrofitting an existing subsonic axial turbine. Without redesigning turbine airfoils, the stator endwall contour was modified to integrate the subsonic axial turbine to a diffuser and a rotating detonation combustor. Performance of the retrofitted subsonic axial turbine exposed to fluctuations from a diffuser is evaluated at several frequencies, amplitudes and inlet Mach numbers, with an increased level of model fidelity, including unsteady stator alone, unsteady turbine stage with a reduced model, full unsteady turbine stage assessment. Turbine efficiency, damping of oscillations, and loss budgeting are assessed. A multi-step optimization strategy is utilized to enhance turbine efficiency by improving the endwall contouring. A performance map is created to examine the operating range. Finally, a new type of pressure probes was developed and angular calibration was performed. A whisker-inspired design enabled the reduction of the vortex shedding effect.

1. INTRODUCTION

1.1 Literature Review of Pressure Gain Combustion

Two types of pressure gain combustors are under investigation around the world. They deliver higher total inlet pressure to the downstream turbine compared to conventional Brayton cycle-based combustion. Pulse detonation combustors (PDC), in which the gas is periodically filled, burnt and purged at low frequencies [1], deliver mixed subsonic and supersonic flow at the outlet. Rotating detonation combustors (RDC) in which a rotating detonation wave burns the fresh fuel continuously offer compactness, ease of operation and only one single detonation initiation of the air-fuel mixture [2][3]. RDCs have been experimentally studied since the 60s up to present [4][5] and numerous CFD studies were performed with increasing complexity, ranging from two dimensional fully premixed to three-dimensional non-premixed hybrid LES-URANS simulations [6][7][8][9][10][11][12]. Recently, reduced RDC models based on the method of characteristics were proposed by Fievisohn and Yu [13] and Sousa et al. [14] to perform fast evaluations and results displayed good agreements with 2D URANS simulations. Braun et al. [15] showed that the outlet of RDCs suffered from peak-to-peak total pressure fluctuations up to a factor of 6. Additionally, Braun et al. [16] used the outlet conditions of a 2D reacting RDC simulation, which was mostly supersonic as unsteady inlet boundary condition for the 3D non-reacting nozzle simulations, to decrease the computational burden. The flow angle fluctuations can be mitigated by more than 50% with optimized nozzle designs.

Flow exhausted by a RDC is transonic with Mach number fluctuating between 0.8 and 1.5 [15], hence either the isentropic limit (for subsonic flow) or Kantrowitz limit (for supersonic flows) need to be respected such that turbines could be self-started. One option is to mount a subsonic axial turbine. However, direct coupling of a subsonic axial turbine with a RDC resulted in unstarted operation, leading to unsatisfactory aerodynamic performance as demonstrated in [17]. Therefore, a diffuser is required to be placed upstream of the subsonic axial turbine to decelerate the low supersonic flow to the subsonic regime. A wide range of axial turbine efficiencies were retrieved from numerous experimental and numerical studies, depending on the fluctuating frequencies and amplitudes [18][19][20][21][22][23], from 53% for high frequency investigations up to 87% for low amplitude and low frequency investigations. Another option is to mount a supersonic axial

turbine. In this case, a nozzle [16] is attached upstream of the turbine to accelerate low supersonic flow to the high supersonic regime. A new class of supersonic turbines was proposed with a design methodology based on the method of characteristics (MOC) to operate at supersonic inflows [17][24]. Such supersonic turbines are able to attenuate angular fluctuations by 90% at high frequencies[25]. In a perspective of the system integration, a detonation-based engine model predicted an 8 percentage-points of thermal efficiency gain and 5 percentage-points decrease of specific fuel consumption at low pressure ratios compared to the deflagration-based engine [26].

Aerodynamic probes are ubiquitous in gas turbine monitoring due to their robustness and easiness of operation. However, the intrusion into the flow path creates the steady-state pressure distortion and unsteady phenomena associated to the vortex shedding. To protect the sensor from the harsh environment (hot flow and particles) and allow for a higher spatial resolution (the smallest sensor is in the mm-scale), sensors are usually mounted within the probe, recessed from the surface. However, these sub-surface mounted sensors cause a reduction in the time resolution of the probe, compared to flush-mounted sensors. The resonance frequency of hole-cavity-sensor arrangements depends on the length, diameter, shape of the hole and the volume of the cavity in front of the sensor[27]. During the past decades, advances in sensor technology and manufacturing techniques have allowed the continuous development of smaller and faster directional probes. Comprehensive reviews on the state of the art in high-frequency aerodynamic probes were provided by Ainsworth et al[28], and Sieverding et al[29].

A multi-hole probe can be classified by shape [30] as either pyramid, conical, or hemispherical. Dominy and Hodson [31] evaluated the steady aerodynamic performance of different five-hole probe geometries and observed the appearance of recirculation bubble at low Reynolds number close to the leading edge. Several researchers have developed seven-hole probes for large angles of attack. Villafane et al [32] compared the angle sensitivity of conical and hemispherical probes, as well as the error propagation of the calibration data during the post-processing. Numerical investigations have aided in the calibration and development of aerodynamic probes. For instance, Delhaye et al [33] used CFD to characterize the performance of a pyramidal probe with flush-mounted sensors, and the computational results aided to characterize the vortex shedding as well as the need to use a multi-zonal calibration procedure to account for the separations bubble occurring in the wedge probe.

Probe measurements suffer from vortex shedding unsteadiness due to the probe intrusion with the flow field. To suppress the vortex induced vibration (VIV), biomimicry has been used to explore whisker-like geometries. Hanke et al. [34] numerically demonstrated that whisker-like vibrissa reduced the lift forces by 90% compared to the cylinder-like model. Hans et al. [35] proved that undulations on both the major and minor axis of the stem are essential to attenuate the lift force and suppress the vortex shedding. Kottapalli et al. [36] tested the whisker-like flow sensors and reduced the amplitude of the vortex shedding by 50 times. In addition, whisker-like sensors displayed high sensitivity to the underwater environments thanks to its low self-induced vibrating noise [37]. Beem et al. [38] discovered that whisker-like flow sensors are better than cylindrical sensors to detect wake-induced vibrations because of reduced interference of the vortex shedding in their underwater tests. Such unique detection mechanism is also used by seals to capture preys [39]. Additionally, in terms of heat transfer, a numerical investigation of whisker-like pin fins augmented heat transfer by 20% compared to the cylindrical pin fins at a Reynolds number of 104 [40].

1.2 Research Objectives

1.2.1 Develop a compact expansion system

In the quest to develop more compact systems, one option would be to directly expand the transonic-supersonic flow downstream of the RDCs. Conventional fluid expansion devices have shown to be inadequate to directly cope with the supersonic flow exiting from the RDCs. On the contrary, the supersonic turbine unveils benefits in terms of engine compactness and aerodynamic performance when subjected to high supersonic pulsating flow. Additionally, optimized nozzles could be integrated with the RDCs to minimize the flow fluctuations and maximize the power extraction of the entire system.

1.2.2 Develop an efficient expansion system

Another option would be to implement a subsonic system designed to deliver the maximum possible turbine efficiency. Direct coupling of a subsonic conventional turbines and RDCs, without any diffuser, results in unstated operation, which leads to deficient aerodynamic performance.

Hence, in this case a diffuser is required to decelerate the transonic-supersonic flow from RDCs to the subsonic regime and integrated with the subsonic fluid machinery.

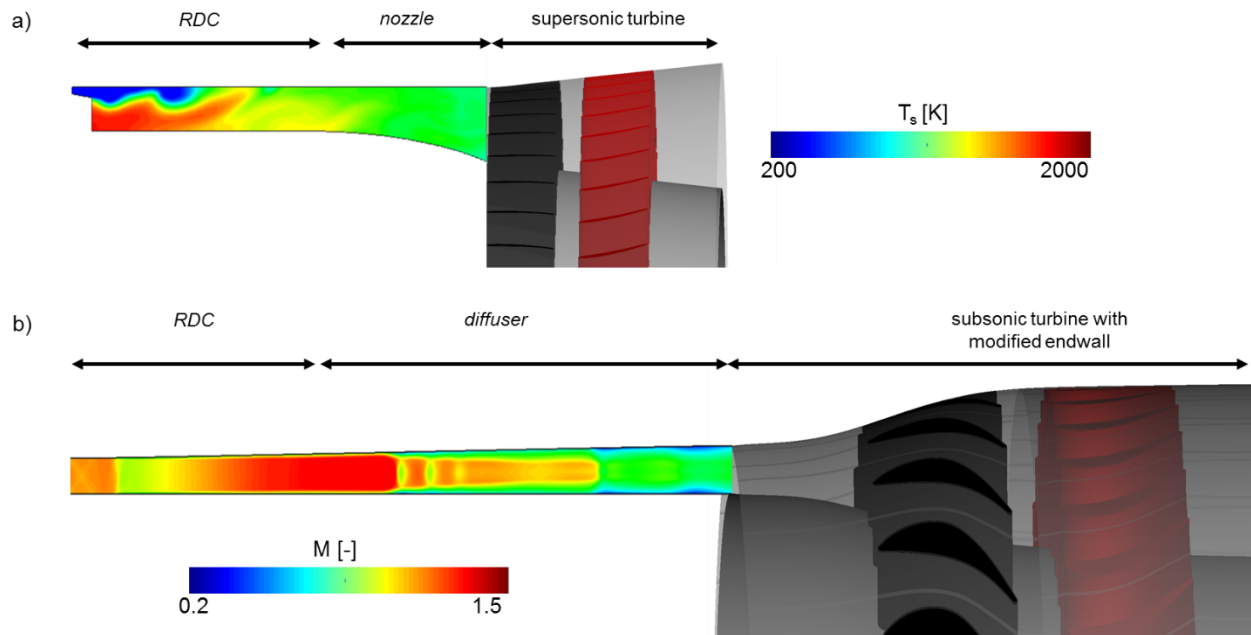


Figure 1.1. Development of expansion systems for RDCs.

1.2.3 Develop flow measurement tools

The flow field downstream of RDCs is characterized by high-frequency and large-amplitude fluctuations. Accurate tracking of pressure, flow angles, and Mach numbers is essential to evaluate the performance of the fluid expansion systems. Hence, appropriate flow measurement tools are needed.

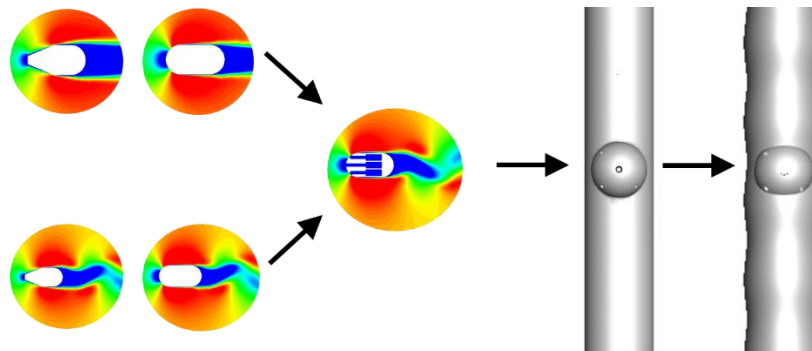


Figure 1.2. Development of flow measurement tools.

1.3 Research Methodology

To achieve the aforementioned three objectives, the following methodology is implemented.

1.3.1 Develop a Supersonic Axial Turbine

A supersonic axial turbine is designed and characterized when exposed to fluctuations from a nozzle downstream of a rotating detonation combustor without any dilution via the numerical methodology. CFD++ from Metacomp is selected to solve the three-dimensional unsteady Reynolds Averaged Navier Stokes (URANS) equations. The turbine inlet conditions are acquired from a 3D URANS simulation of a nozzle attached to a RDC. The methodology starts with turbine design, mesh sensitivity study, and periodic convergence assessment. Afterwards, the time-resolved performance of the supersonic turbine is investigated in an increased level of complexity. In a first step, unsteady simulations of stator passages exposed to periodic oblique shocks is performed. Total pressure loss is evaluated for several oblique shock frequencies and amplitudes. The unsteady stator outlet profile is extracted and used as inlet condition for the unsteady rotor simulations. In the end, a full stage unsteady simulation is performed to characterize the flow field across the entire turbine stage. Power extraction and total pressure losses are assessed, together with the estimation of the unsteady loss mechanism in the supersonic turbine. The performance map is explored and unsteady heat transfer assessment is carried out.

1.3.2 Retrofit an Existing Subsonic Axial Turbine through Endwall Contouring

A subsonic axial turbine is retrofitted by modifying the stator endwall contouring without redesigning turbine airfoils to achieve an efficient integration to a diffuser and a RDC. Full characterization and optimization of the subsonic axial turbine when exposed to fluctuations from a diffuser is presented via the detailed numerical methodology. CFD++ from Metacomp is selected as URANS solver. The turbine inlet boundary conditions are obtained from a diffuser coupled with a RDC. The methodology starts with mesh sensitivity study and periodic convergence assessment. Afterwards, the endwalls of the conventional subsonic turbine are modified to ingest high subsonic flow. In a first step, the time-resolved performance of the modified subsonic turbines is characterized in an increased level of fidelity: URANS stator simulations, URANS stage

simulations with the mixing plane approach and full unsteady stage simulations. The turbine efficiency is assessed at a wide range of pulsating frequencies and amplitudes. Budgeting of the unsteady loss mechanism is performed to dissect the loss contributions. Based on the performance of the baseline configuration, in the second step a multi-step optimization strategy of the endwall contouring is carried out to enhance the turbine efficiency. The optimization routine starts with a steady optimization, which includes the channel parametrization, mesh automation, RANS simulations, and post-processing. The critical design parameters identified from the steady optimization is fed into the next phase unsteady optimization, where the URANS stage simulations with the mixing plane approach is adopted. Full unsteady simulations of selected turbines are carried out. Finally, an overall gas turbine engine analysis demonstrates the superiority of pressure gain combustion coupled with the optimized subsonic axial turbine. The reduced-order gas turbine model integrates the combustion process of the rotating detonation combustor, losses through the diffuser, and turbine losses. Turbine performance map is created and design of experiments is proposed to replicate the physics in a linear wind tunnel.

1.3.3 Develop Fast-response Multi-hole Directional Probes

A multi-hole directional probe is developed via a numerical methodology. ANSYS Fluent is selected to solve the flow field. The methodology starts with grid sensitivity study and periodic convergence assessment. Afterwards, two different probe architectures (oval and trapezoidal) are characterized at several yaw angles and Mach numbers via 2D URANS simulations. A multi-hole directional probe is designed. Angular calibration is conducted and 3D URANS simulations are performed to evaluate the time-resolved performance. In addition, a whisker-inspired design is explored aiming to attenuate the effect of the induced vortex shedding.

1.4 Dissertation Outline

Chapter one proposes research objectives and methodology. Starting from chapter two, each chapter addresses a corresponding objective based on the order described in Section 1.2. Chapter two describes the design of a supersonic axial turbine and the full characterization of the turbine exposed to large fluctuations from a nozzle attached to a RDC at an increased level of complexity. Chapter three illustrates the retrofitting strategy of efficiently integrating an existing subsonic

axial turbine to a diffuser and a RDC and time-resolved turbine performance is analyzed in an increased level of fidelity. Chapter four outlines the design and characterization of directional probes. Chapter five summarizes the completion of each research objective. The appendix details the validation of numerical solvers, fluid model, and thermodynamic properties.

2. DEVELOPMENT OF A SUPERSONIC AXIAL TURBINE

In this chapter, firstly a supersonic axial turbine capable of ingesting Mach 2 inflow is designed. Afterwards, the time-resolved performance of the supersonic axial turbine exposed to fluctuations from a nozzle downstream of a RDC is characterized in an increased level of complexity. A performance map is generated to evaluate the supersonic turbine at off-design condition. In the end, unsteady heat transfer assessment is performed to dissect different contributions to the unsteady heat flux, by applying the concept of adiabatic wall temperature.

2.1 Turbine Geometry and Boundary Conditions

2.1.1 Turbine Inlet Condition

The turbine inlet condition was obtained from a nozzle downstream of a RDC. Thermally perfect gas (air) was selected as working fluid. Figure 2.1a plots an axial cut of the cylindrical RDC attached to a nozzle geometry optimized to damp the Mach number fluctuations and maximize the unsteady force via a one-dimensional approach outlined by Braun et al. [16]. The nozzle was designed for a mass-flow averaged Mach number of 2 at the outlet, via an outlet-to-inlet area increase of 2.76. The optimized nozzle is depicted in Fig. 2.1b.

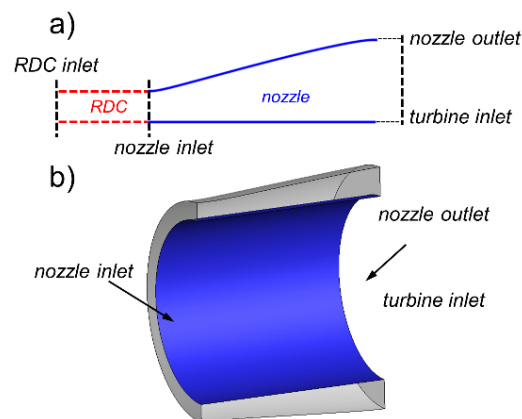


Figure 2.1. a) Geometry of the RDC and nozzle. b) 3D optimized nozzle geometry.

Figure 2.2a depicts the instantaneous static temperature flow field of an unfolded two-dimensional RDC verified in prior work [14] with a single step reaction mechanism of

stoichiometric hydrogen-air. The unsteady outlet conditions of the RDC were then applied at the inlet of the nozzle (Fig. 2.1a) which significantly decreased the simulation time. Figures 2.2b-e plot the instantaneous fluctuations of radially mass-flow-averaged static pressure (Fig. 2.2b), static temperature (Fig. 2.2c), Mach number (Fig. 2.2d), and flow angle (Fig. 2.2e) along a range of azimuthal angle ($0\sim 40^\circ$) at the nozzle outlet.

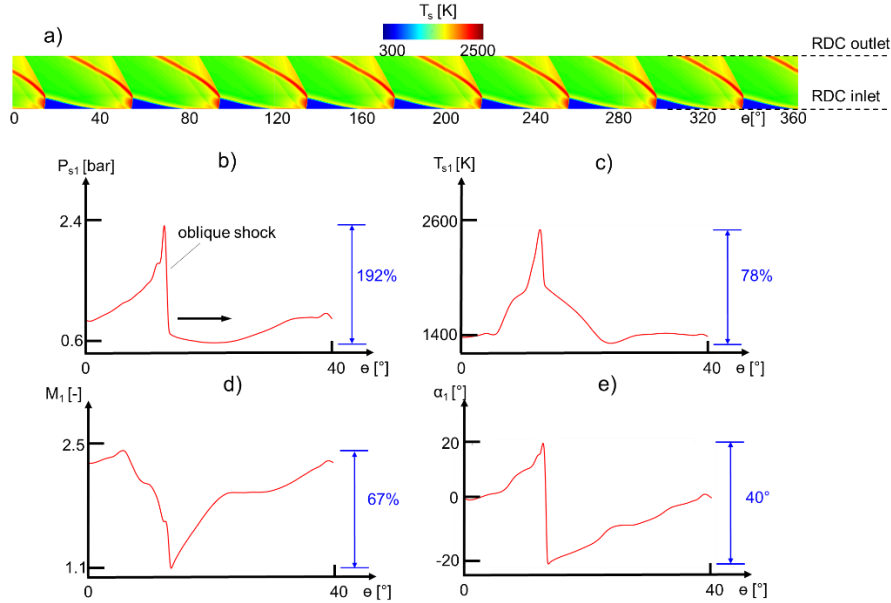


Figure 2.2. a) Instantaneous static temperature contour of the 2D RDC. Nozzle outlet profile: b) static pressure, c) static temperature, d) Mach number, and e) flow angle as a function of the azimuthal angle.

The azimuthal angle is defined as:

$$\theta = \arctan \frac{y}{x} \quad (2.1)$$

The amplitude of fluctuations are defined as:

$$A = \frac{\max - \min}{\text{mean}} \quad (2.2)$$

Static pressure ranges from 0.6 to 2.4 bar with peak-to-peak variations of 192% at the nozzle outlet while this was 235% at nozzle inlet (outlet of the RDC). Mach number ranges between 1.1

and 2.5 with a mass-flow averaged Mach number around 2. While the oblique shock propagated along the azimuthal direction, the flow angle is positive behind of the oblique shock while negative flow angles are present in front of the oblique shock.

2.1.2 Computational Domain

The supersonic turbine stage needs to handle a mass-flow averaged inlet Mach number of 2 and the design starts with a one-dimensional analysis to ensure starting of the turbine [24] at the specified inlet Mach number and flow angle. The flow turning is restricted by the Kantrowitz limit which is 20° for the stator and less than 30° for the rotor. The inlet flow angle to the stator was assumed to be 0° as the mass flow averaged flow angle exiting RDCs is 0° according to Fig. 2.2e. The designed stator vane is depicted in Fig. 2.3a and Fig. 2.3b plots the rotor profile at mid-span. The leading edge and trailing edge are parameterized by specifying the thickness and wedge angle. The pressure and suction side of the blade are formed by Bezier curves, where the number of control points and the normal distance between control points to the camber line are user-defined parameters, as detailed by Sousa and Paniagua [24].

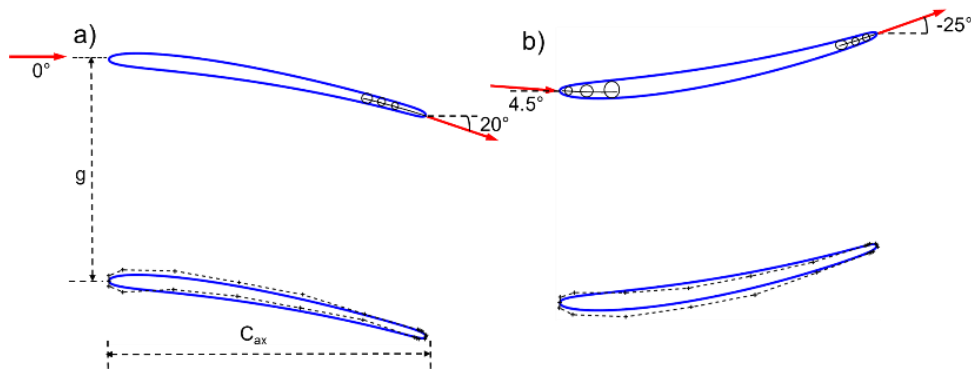


Figure 2.3. Turbine profile at mid-span: a) supersonic stator and b) supersonic rotor.

Table 2.1 shows the geometric parameters of the supersonic turbine. Figure 2.4a plots the meridional view of the stage channel. To enhance the power extraction and ensure swallowing of the flow, the stage channel height is gradually increased ($H_2/H_1=1.2$) to augment the flow turning. Figure 2.4b depicts the numerical grid of the designed supersonic turbine, with a close up of the stator trailing edge grid topology. 1 out of the 72 stage passages is displayed. A three-dimensional

hexahedral mesh was generated with Autogrid5 developed by NUMECA International, including a total of 3.9M grid points

Table 2.1: Turbine geometric parameters at mean radius.

	stator	rotor
C_{ax} [mm]	60	60
g/C_{ax} [-]	0.7	0.7
h/C_{ax} [-]	1.09	1.31
RPM [-]	-	6282

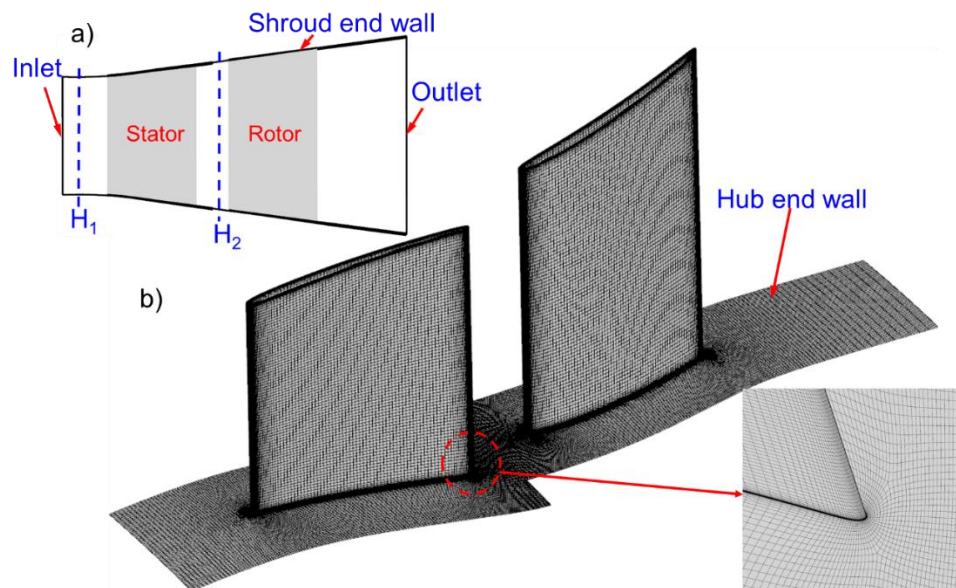


Figure 2.4. a) Channel variation. b) Numerical grid with a close up of the stator trailing edge.

2.1.3 Grid Sensitivity

A grid sensitivity study based on the method of Celik [41] was performed on a steady simulation with four different grid levels ranging from a cell size of around 1.3 million (coarse) to 5 million (fine). Figure 2.5a displays the decreasing trend of the rotor relative total pressure loss with the increasing amount of computational cells. The relative total pressure loss decreases by around 0.02% from the medium to the fine mesh and the computed grid convergence index (GCI) from the fine to the medium mesh was 0.65%, indicative of a good grid convergence. Therefore, the medium mesh of around 3.9 million cells was selected for a single passage. The growth rate of the boundary layer for the medium mesh is 1.35 and local refinement was ensured close to wall to

resolve the viscous sublayer. Figure 2.5b shows the mechanical torque for each iteration. After 1000 iterations, the torque deviation was less than 0.28%, indicative for the convergence of the simulation.

The local discretization error of each grid point ‘i’ at rotor outlet is defined as:

$$\varepsilon(i) = \frac{P_{03R_medium_interp}(i) - P_{03R_fine}(i)}{P_{03R_fine}(i)} \quad (2.3)$$

Where $P_{03R_fine}(i)$ represents the relative total pressure of each discretized point of the fine mesh at the rotor outlet and $P_{03R_medium_interp}(i)$ depicts the interpolated relative total pressure of each discretized point from the medium mesh to the fine mesh at rotor outlet. Figure 2.5c and 2.5d display the relative total pressure contour at rotor outlet retrieved from the grid sensitivity study. Figure 2.5e depicts the contour of local discretization errors of the medium mesh at the rotor outlet. Higher local discretization errors are located in the wake of the rotor pressure side near the shroud.

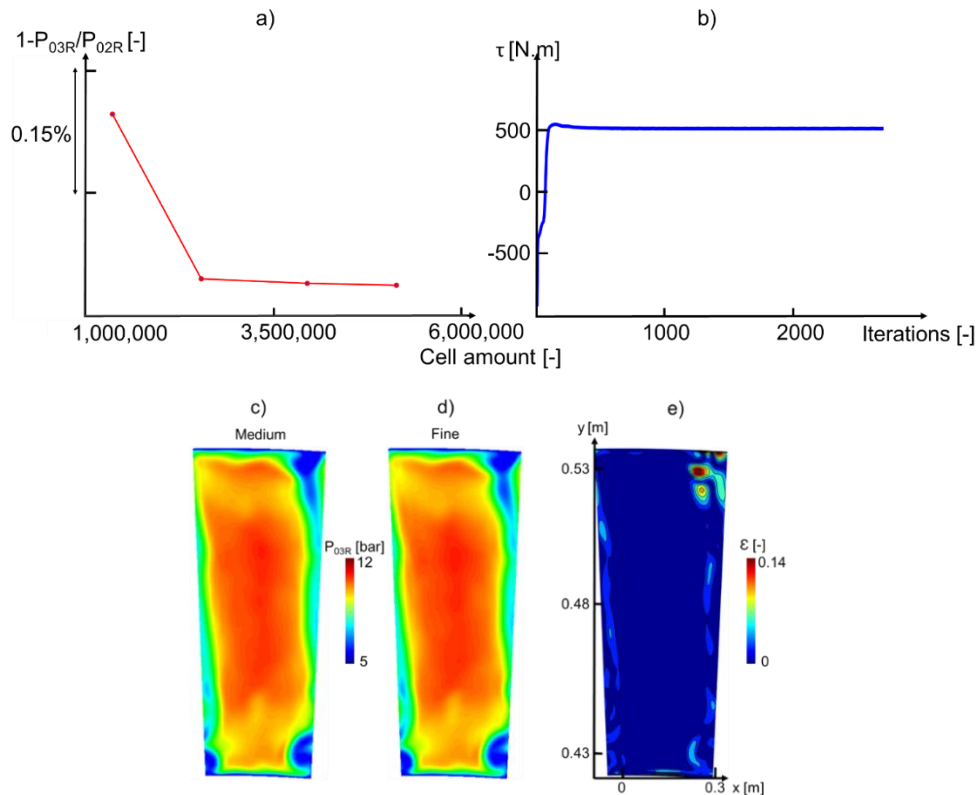


Figure 2.5. a) Rotor relative total pressure loss in function of grid size. b) Torque in function of the convergence. Contour of relative total pressure at rotor outlet for the c) medium mesh and d) fine mesh. e) Local discretization error of the medium mesh.

2.1.4 Steady State Performance

The steady performance is quantified by two parameters: stator absolute total pressure loss ($1 - P_{02}/P_{01}$) and rotor relative total pressure loss ($1 - P_{03R}/P_{02R}$). Figure 8 depicts the relative Mach contour of the supersonic turbine at midspan. At stator and rotor leading edge, subsonic pockets are observed due to the strength of the shock on the stator and reflected shock waves travelling throughout the passage. Due to the shock boundary layer interactions, small low Mach zones are visible both in the rotor and stator passage on the pressure side. The stator exit Mach number was 2 and the outlet flow angle was 18° compared to the targeted 20° from the 1D design. Throughout the stator, total pressure loss is 11.9% while this is 15.5% within the rotor.

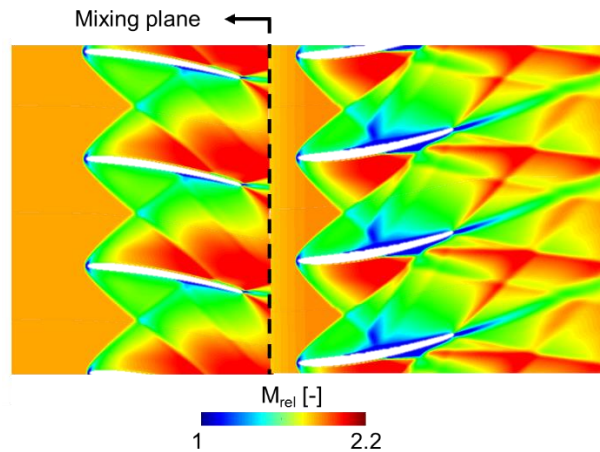


Figure 2.6. Steady flow field of the supersonic turbine at midspan for an inlet Mach number of 2.

2.1.5 Periodic Convergence

With the method of Clark and Grover [42], the periodic convergence in time was quantified and a series of fuzzy sets was generated for the mass-flow-averaged static pressure ($\bar{P}_{2_current}(t)$, Equation 2.4) at the stator outlet. Mean-level fluctuations (f_m , Equation 2.5), Discrete Fourier Transform (DFT) amplitude (f_A , Equation 2.6), phase (f_ϕ , Equation 2.7) and cross-correlation coefficient (CCF, Equation 2.9) were calculated for two consecutive cycles to evaluate the membership grade of periodic convergence for each fuzzy set. An overall fuzzy set (f_c , Equation 2.10) was generated by applying a multi-valued logic. For a comprehensive review on the fuzzy set theory, the reader is referred to Klir and Yuan [43].

$$\bar{P}_{2_current}(t) = \frac{\sum_{i=1}^n P_{2_current}(t) \rho_i |\overrightarrow{V_{ax_i}} \cdot \overrightarrow{S_i}|}{\sum_{i=1}^n \rho_i |\overrightarrow{V_{ax_i}} \cdot \overrightarrow{S_i}|} \quad (2.4)$$

$$f_M = 1 - \left| 1 - \frac{\bar{P}_{2_current}(t)}{\bar{P}_{2_previous}(t)} \right| \quad (2.5)$$

$$f_A = 1 - \left| 1 - \frac{A_{current}}{A_{previous}} \right| \quad (2.6)$$

$$f_\emptyset = 1 - \left| \frac{\emptyset_{current} - \emptyset_{previous}}{\pi} \right| \quad (2.7)$$

$$CCF = \frac{\sum_{n=1}^N \bar{P}_{2_previous}(t) \bar{P}_{2_current}(t)}{[\sum_{n=1}^N \bar{P}_{2_previous}(t)^2 \sum_{n=1}^N \bar{P}_{2_current}(t)^2]^{\frac{1}{2}}} \quad (2.8)$$

$$f_S = CCF(\bar{P}_{2_previous}(t), \bar{P}_{2_current}(t)) \quad (2.9)$$

$$f_C = \min(f_M, f_A, f_\emptyset, f_S) \quad (2.10)$$

The URANS stator simulation was selected for the convergence analysis. The full wheel counts 72 stators and allows for 9 oblique shock waves traveling throughout the passage, indicative for eight stator passages per oblique shock wave and covers 40° in terms of the azimuthal angle (from 0 to 40°). The membership grade of each fuzzy set is detailed in Table 2.2, where the overall periodic convergence is achieved when $f_C \geq 0.95$. The computational time of each URANS stator simulation was 72 hours on 16 cores of one Intel Xeon-E5 processor.

Table 2.2: Evaluation of periodic convergence.

Fuzzy set	Membership grade
f_m	0.9996
f_s	1
f_A	0.9904
f_ϕ	0.9841
fc	0.9841

2.2 Time-Resolved Analysis

2.2.1 Time-Resolved Stator Characterization

Figure 2.7 illustrates the Mach contour (Fig. 2.7a) and total pressure contour (Fig. 2.7b) at midspan of a supersonic stator exposed to the rotating oblique shock from the RDC for three consecutive time steps (phases). The metal angle of the stator vanes was selected to be opposite to the incoming oblique shock angle (which sets the flow angle) so that the high momentum flow behind the oblique shock had the same direction as the outlet metal angle of the stator. The high Mach number flow behind the oblique shock, also characterized by high momentum (high total pressure), remained supersonic throughout the passage. However downstream in the axial direction, regions of lower Mach number and regions of subsonic flow are observed. In front of the oblique shock, flow angles are opposed to the outlet metal angle (Fig. 2.2e), hence stronger shocks are needed to turn the flow through the stator passage. Furthermore, the single continuous oblique shock at the inlet (Fig. 2.7b) breaks down into several oblique shock structures across 2-3 passages. Figure 2.7c details the shock patterns within the stator passage at phase 3. At point ‘A’, a weaker shock interacts with two stronger reflected shocks from the leading edge and results into two oblique shocks downstream of point ‘A’. One shock impinges on the trailing edge of the suction side triggering an early boundary layer separation on the wake and one triggers a weak interaction without boundary layer separation [44] on the pressure side (Point ‘B’). At point ‘C’, downstream of the trailing edge, the reflected shock from the pressure side (Point ‘B’) and the reflected shock from point ‘A’ merge and reflect off as a single shock towards the stator outlet.

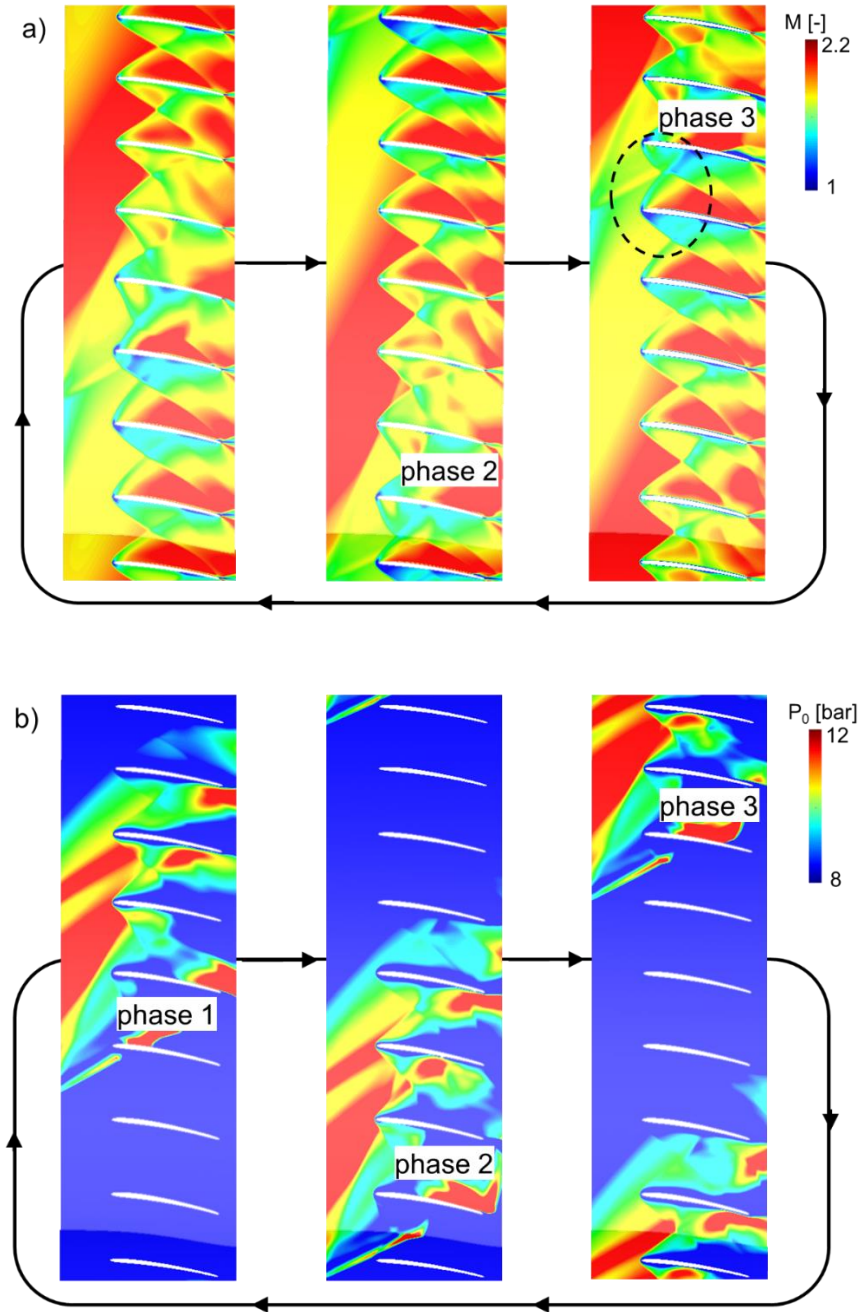
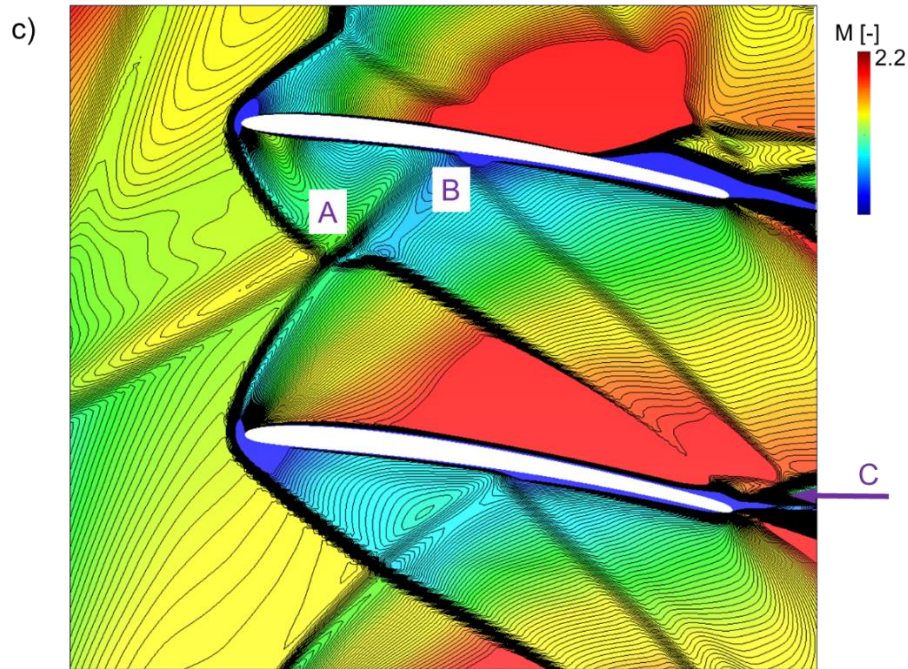


Figure 2.7. URANS stator simulation exposed to oblique shocks for three consecutive phases at mid-span ($\bar{f}=0.24$, $\bar{A}=1$): a) Mach contour and b) total pressure contour. c) Close up of the instantaneous shock pattern during phase 3.

Figure 2.7. Continued.



The instantaneous stator outlet Mach number flow field at phase 3 is depicted in Fig. 2.8a, total pressure in Fig. 2.8b, and total temperature in Fig. 2.8c. In the figures, 8 out of the 72 stage passages are shown, which is equivalent to an azimuthal angle of 40° . Due to the viscous effect of the end walls, low Mach zones are observed closed to the hub and shroud in Fig. 2.8a, particularly in the right five stator passages, in which secondary flow features are more dominant due to the higher turning of the flow in front of the oblique shock (Fig. 2.2e). The wakes are characterized by vertical low Mach strips, as flow turning through the vanes was limited to 20° in contrast to the flow field in subsonic turbines. The instantaneous mass-flow-averaged outlet Mach number was 1.96 compared to 2.06 at inlet, indicating that the supersonic flow was slightly diffused across the stator passages. In Fig. 2.8b, peak total pressure decreases from 17.6 bar to 13.1 bar. The contour of total temperature in Fig. 2.8c displays a radially uniform distribution

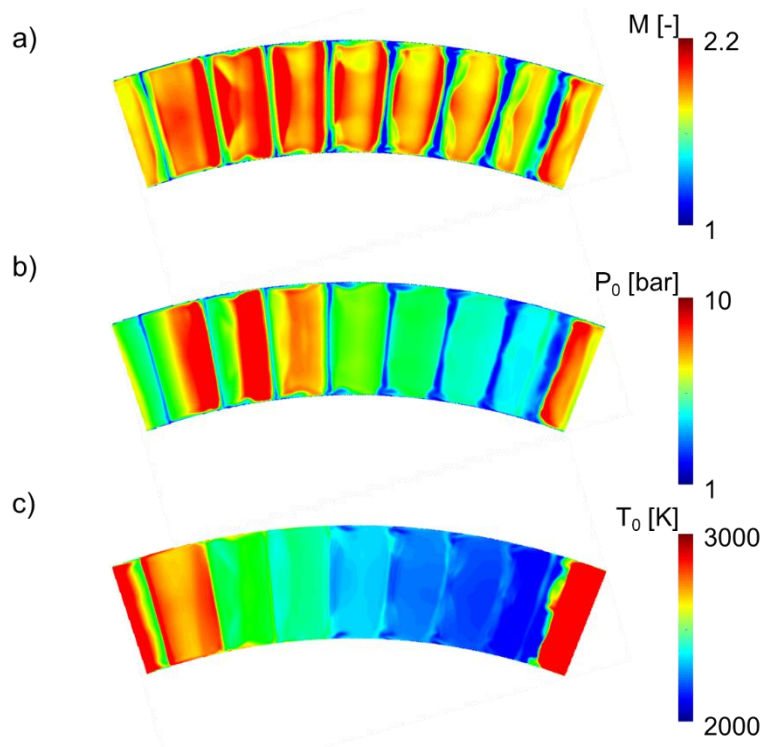


Figure 2.8. Instantaneous contour of stator outlet at phase 3: a) Mach number, b) total pressure, and c) total temperature ($\bar{f}=0.24$, $\bar{A}=1$).

Figure 2.9a plots the instantaneous fluctuations of the radially mass-flow-averaged flow angle at the stator outlet (black line) and at the stator inlet (red line) along the azimuthal direction. The instantaneous mass-flow-averaged outlet flow angle was 16.4° compared to the designed 20° . From inlet to outlet, flow angle evolved from containing both negative and positive components to a uniform orientation (containing predominantly positive components). This is important as negative and positive flow components at the rotor inlet would counterbalance and result in low power extraction. It is observed that fluctuations of static pressure (Fig. 2.9b) are attenuated but fluctuations of Mach number (Fig. 2.9c) and static temperature (Fig. 2.9d) are all amplified. The increase of Mach number fluctuations is explained by the viscous effects acting on the blade which result in a wake with low Mach number flow. The instantaneous stator damping is evaluated via Equation (2.11) to quantify the attenuation (positive damping) and enhancement (negative damping) of fluctuations.

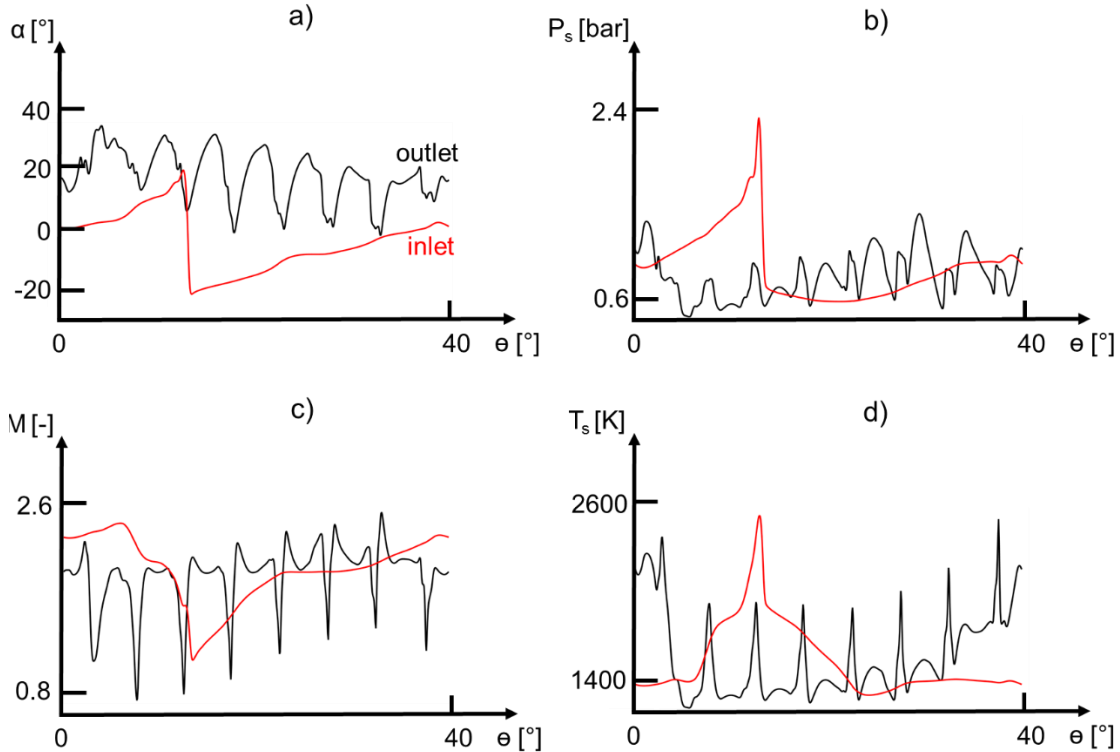


Figure 2.9. Instantaneous stator fluctuations in function of the azimuthal angle at phase 3: a) flow angle, b) static pressure, c) Mach number, and d) static temperature ($\bar{f}=0.24$, $\bar{A}=1$).

The instantaneous stator damping is defined as:

$$\xi_s(t) = \frac{A_1 - A_2}{A_1} \quad (2.11)$$

The angular fluctuations were attenuated by 82% across the stator passage, which ensured a more uniform flow angle delivery to the downstream rotor. The static pressure fluctuations were damped by 37.4%. The Mach number fluctuations were amplified by 43.3% due to the end wall effects in which zones of low Mach number are present (Fig. 2.8a).

2.2.2 Influence of the Reduced Frequency and Amplitude

The cycle-mass-averaged of the mass-flow-averaged total pressure loss was evaluated at several reduced frequencies and non-dimensional amplitudes to quantify the aerodynamic performance of the supersonic stator. Figure 2.10 plots the total pressure loss at different reduced

frequencies (evaluation is illustrated in Appendix) and non-dimensional amplitudes. At low reduced frequencies (<0.15), the total pressure loss was locked between 21.5% and 23%. However, for increased reduced frequencies, the effect of non-dimensional amplitude was enhanced. At high reduced frequencies (≈ 0.5), doubling the non-dimensional amplitude resulted in a total pressure loss up to 34%, highlighting the importance of well-designed nozzles that minimize flow fluctuations

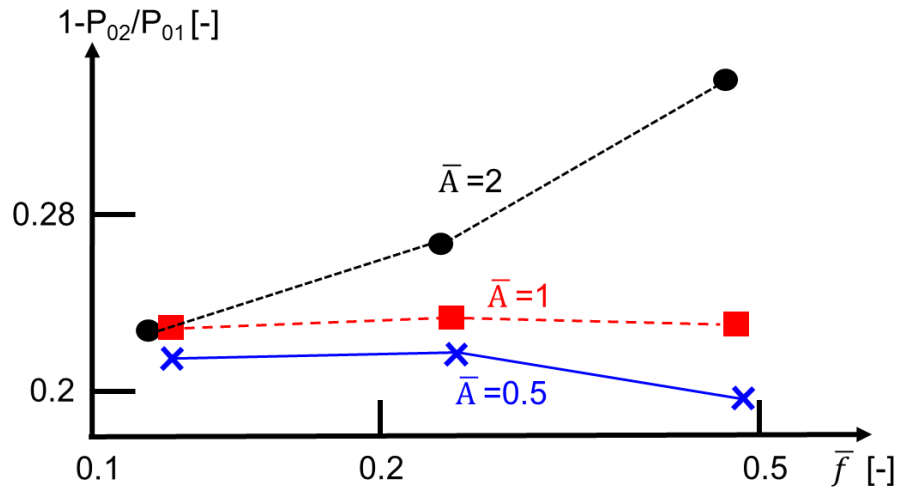


Figure 2.10. Stator total pressure loss in function of reduced frequency and non-dimensional amplitude.

2.2.3 Time-Resolved Rotor Performance

For the unsteady rotor simulation, eight rotor passages (16 million grid points) were modeled and the unsteady stator outlet profiles (retrieved in section 2.2.2) were extracted, mass-flow averaged along the radial direction and imposed at the rotor inlet. The RPM was 17% of the speed of the inlet oblique shock wave. For a URANS rotor simulation, the computational burden was 120 hours on 24 cores of two Intel Xeon-E5 processors.

Figure 2.11a illustrates the flow field of the supersonic rotor exposed to the upstream stator outlet conditions for three time steps (phases). Several oblique shocks are observed at the rotor inlet, induced from the upstream stator. Interestingly, regions of subsonic flow emerged at the rotor pressure side around mid-chord with increasing strength and size in regions where the instantaneous rotor inlet contained low momentum flow. Figure 2.11b details shock patterns within the rotor passages during phase 3. Point 'A' is the intersection of the two leading edge shocks and

results in two reflected shocks: one impinging on the rotor suction side and one on the pressure side. The shock impinging on the pressure side results in a terminating normal shock beyond which the flow is subsonic (region ‘C’). In region ‘B’, expansion fans are observed due to the curvature of the blade. Downstream of the trailing edge, trailing edge vortices are formed and at point ‘D’, the two shocks from the trailing edge of two adjacent rotor blades interact.

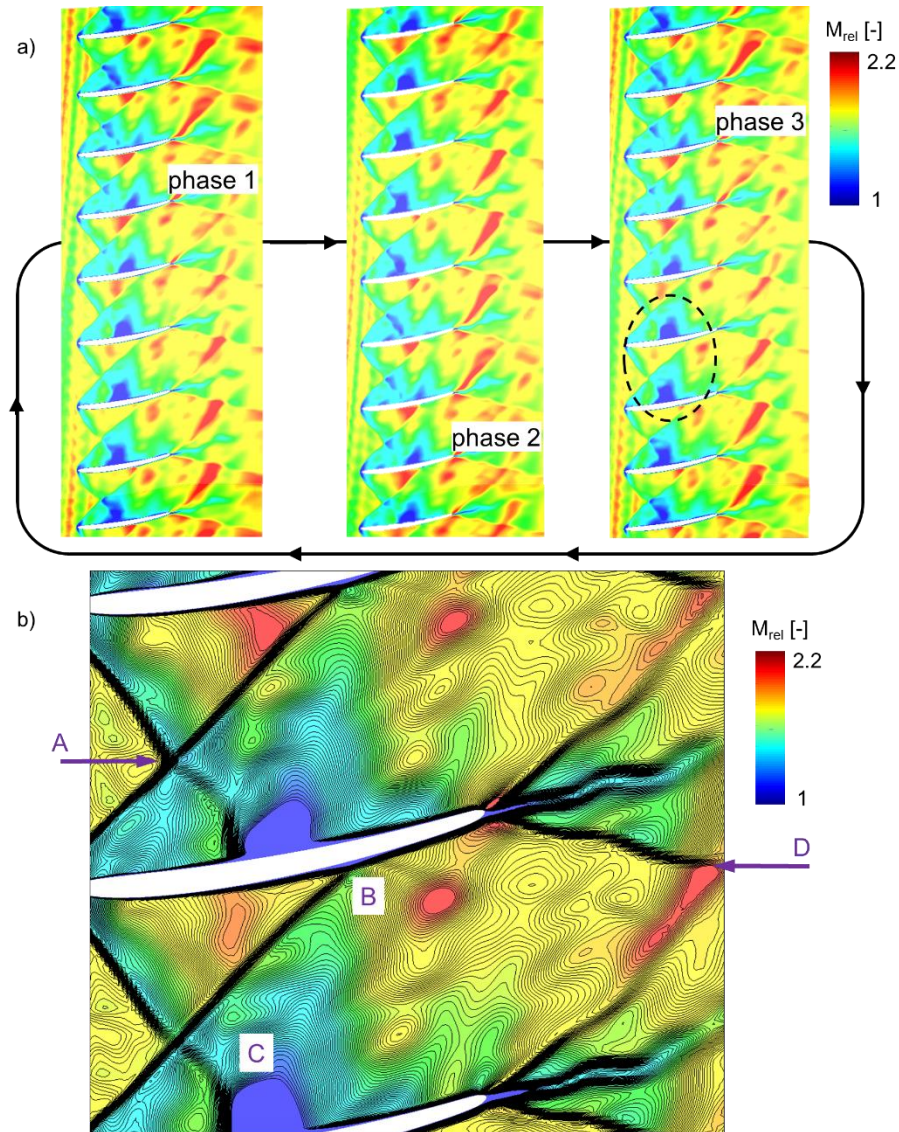


Figure 2.11. a) Flow field of a URANS rotor simulation at mid-span for three consecutive phases ($\bar{f}=0.24$, $\bar{A}=1$). b) Close up of the instantaneous shock pattern during phase 3.

Figure 2.12 displays the instantaneous rotor outlet relative Mach number distribution (Fig. 2.12a), relative total pressure distribution (Fig. 2.12b), and relative total temperature distribution

(Fig. 2.12c). In Fig. 2.12a, the relative Mach number contour reveals secondary flow structures different from the stator outlet topology shown in Fig. 2.8a, with small vertical structures across all rotor passages. The instantaneous outlet mass-flow averaged relative Mach number at phase 3 was 1.9 compared to 1.85 at inlet, indicative that the supersonic flow was accelerated through the rotor passages. Peak relative total pressure decreased from 11.6 bar to 5.4 bar (Fig. 2.12b). Zones of high relative total pressure (Fig. 2.12b) and high relative total temperature (Fig. 2.12c) were revealed, showing that the fluctuations induced by the upstream oblique shock are conveyed downstream to the next stage.

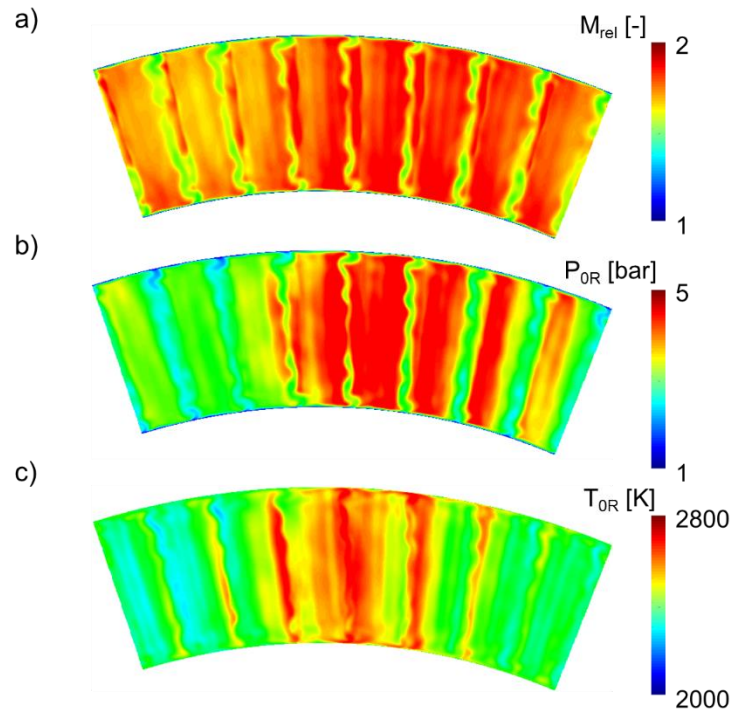


Figure 2.12. Instantaneous contour of rotor outlet at phase 3: a) relative Mach number, b) relative total pressure, and c) relative total temperature ($\bar{f}=0.24$, $\bar{A}=1$).

The instantaneous rotor damping is defined as:

$$\xi_R(t) = \frac{A_2 - A_3}{A_2} \quad (2.12)$$

Figure 2.13 plots the instantaneous fluctuations of radially mass-flow-averaged relative flow angle (Fig. 2.13a), static pressure (Fig. 2.13b), relative Mach number (Fig. 2.13c) and static

temperature (Fig. 2.13d) at the rotor inlet and outlet along the azimuthal direction. All fluctuations were instantaneously attenuated across the rotor passage as shown in Table 2.3, and the relative angular fluctuations were damped by 93%. The instantaneous mass-flow-averaged outlet relative flow angle was -19.3° compared to -25° from the 1D design. Power extraction and relative total pressure loss were computed to quantify the aerodynamic performance of the supersonic rotor. The time-averaged power was evaluated via Equation (2.13) and Equation (2.14):

$$\acute{o} = \text{mean}(\acute{o}(t)) \quad (2.13)$$

$$\dot{W} = \acute{o}\omega n \quad (2.14)$$

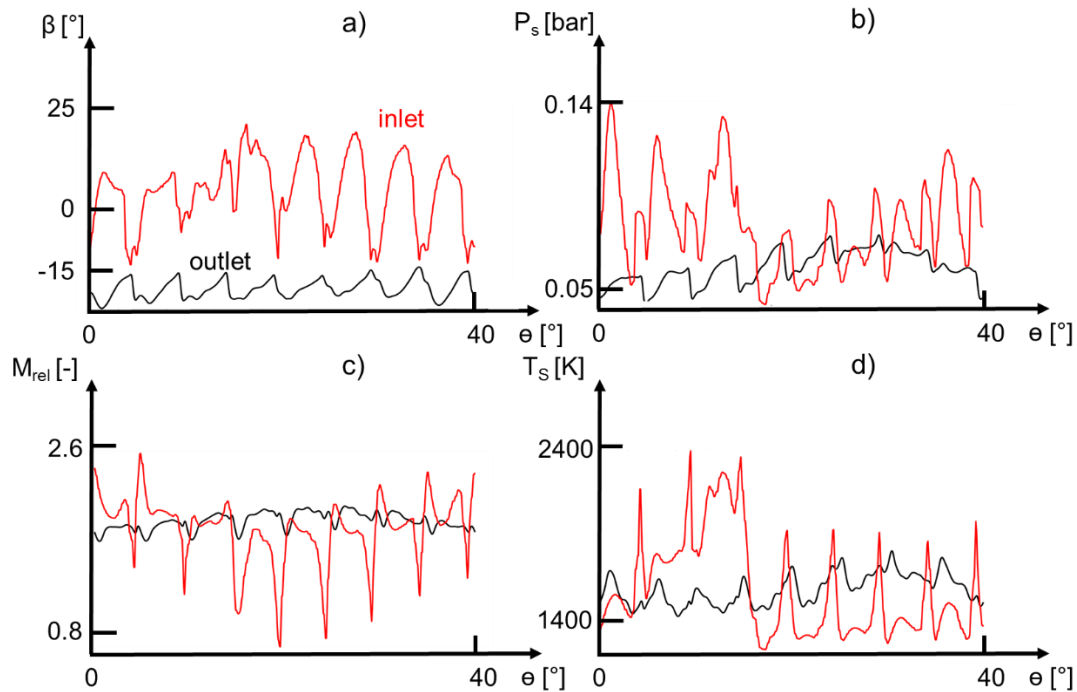


Figure 2.13. Instantaneous rotor fluctuations in function of the azimuthal angle at phase 3: a) relative flow angle, b) static pressure, c) relative Mach number, and d) static temperature ($\bar{f}=0.24$, $\bar{A}=1$).

Results of the performance assessment are summarized in Table 2.3. The aerodynamic loss, depicted by the relative total pressure drop across the rotor was 30.2%. The time-averaged mass flow rate at the inlet of the 72 rotors (full wheel) was 59.4kg/s and total power was 10.6MW.

Table 2.3: Performance assessment and instantaneous rotor damping ($\bar{f}=0.24$, $\bar{A}=1$).

$\zeta_{R,\beta}(t)$	93.0%
$\zeta_{R,P_s}(t)$	54.3%
$\zeta_{R,Mrel}(t)$	82.6%
$\zeta_{R,T_s}(t)$	67.0%
$1-P_{03R}/P_{02R}$	30.2%
\dot{W}	10.6 MW

2.2.4 Time-Resolved Turbine Stage Assessment

A URANS stage simulation was performed with 8 stator passages and 8 rotor passages, which resulted in a total of 31 million grids points. The computational burden was 360 hours on 30 cores of three Intel Xeon-E5 processors to achieve periodic convergence.

Figure 2.14a depicts three consecutive time instants (phases) of a supersonic turbine stage exposed to a rotating oblique shock. Figure 2.14b details the complex shock patterns and secondary flow structures within the turbine stage at phase 3. The stator passage shows similar features as stator alone simulations (Fig. 2.7c) with shock interactions downstream of the leading edge at point ‘A’ and a weak shock boundary layer interaction on the stator pressure side (‘B’). The reflected shock at point ‘B’ interacts with the trailing edge main shock at point ‘C’ and additionally impacts on the rotor leading edge. At point ‘C’, two main shocks from the trailing edge are identified: one impinging on the nearby rotor leading edge and one interacting with the reflected shock from the leading edge of the downstream rotor. At point ‘D’, multiple shocks interact before entering the rotor passage and the stator trailing edge vortex also travels into the rotor passage enhancing the three-dimensional flow structures within the rotor passage. Furthermore, downstream at point ‘D’, one shock interacts with the suction side triggering early separation of the rotor trailing edge and the other one impinges on the rotor pressure side causing a strong interaction with the pressure side boundary layer and resulting in a low subsonic pocket (point ‘E’). Downstream at point ‘E’, a reattachment shock is observed and point ‘F’ denotes the point where the rotor trailing edge vortex starts. Figure 2.14c displays the streamlines at both the hub and shroud end wall. One can observe that the streamlines tend to move towards the endwall close to the trailing edge. This is probably due to the divergence of the channel that locally accelerated the flow and counteracted the secondary flow effects. From the static temperature of the stator and rotor blades for three

consecutive time frames (Fig. 2.14d), the stator passage is mainly dominated by the periodic sweeping of the oblique shock, with high temperatures behind the shock front, and behind reflected shocks on the pressure side of the stator.

The instantaneous stage damping is defined as:

$$\xi_{stage}(t) = \frac{A_1 - A_3}{A_1} \quad (2.15)$$

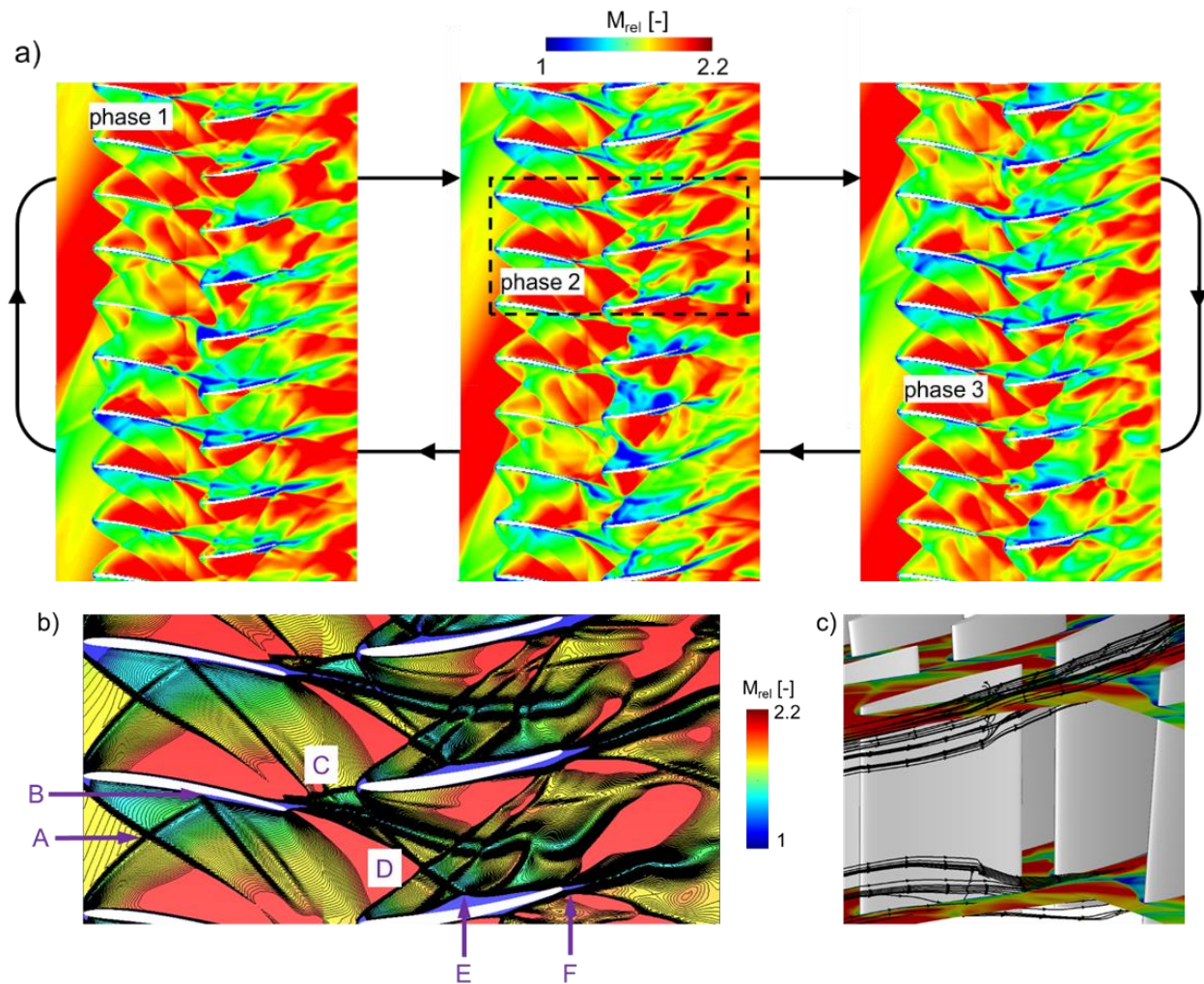


Figure 2.14. a) Flow field of a URANS stage simulation at mid-span exposed to oblique shocks for three consecutive phases. b) Close up of the instantaneous shock pattern during phase 2. c) 3D flow structure within the stage during phase 2. d) Static temperature of stator vanes and rotor blades for three phases ($\bar{f}=0.24$, $\bar{A}=1$).

Figure 2.14. Continued.

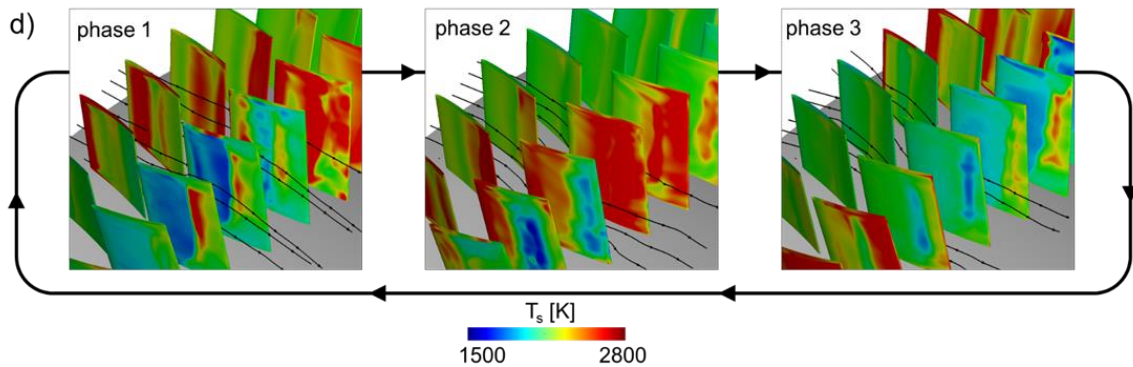


Figure 2.15 shows the instantaneous fluctuations of radially mass-flow-averaged flow angle (Fig. 2.15a), static pressure (Fig. 2.15b), relative Mach number (Fig. 2.15c) and static temperature (Fig. 2.15d) at the stator inlet and rotor outlet along the azimuthal direction. At this time step, the rotor outlet profile was shifted by 19° due to the blade rotation. All fluctuations were instantaneously attenuated across the entire stage as shown in Table 2.4, with angular fluctuations damped by 78.1%. The instantaneous mass-flow-averaged stator outlet flow angle was 17.3° . The instantaneous mass-flow-averaged rotor outlet relative flow angle was -19.2° , which was close to the rotor-alone simulations. The total power across the stage (full wheel) was 11.3MW.

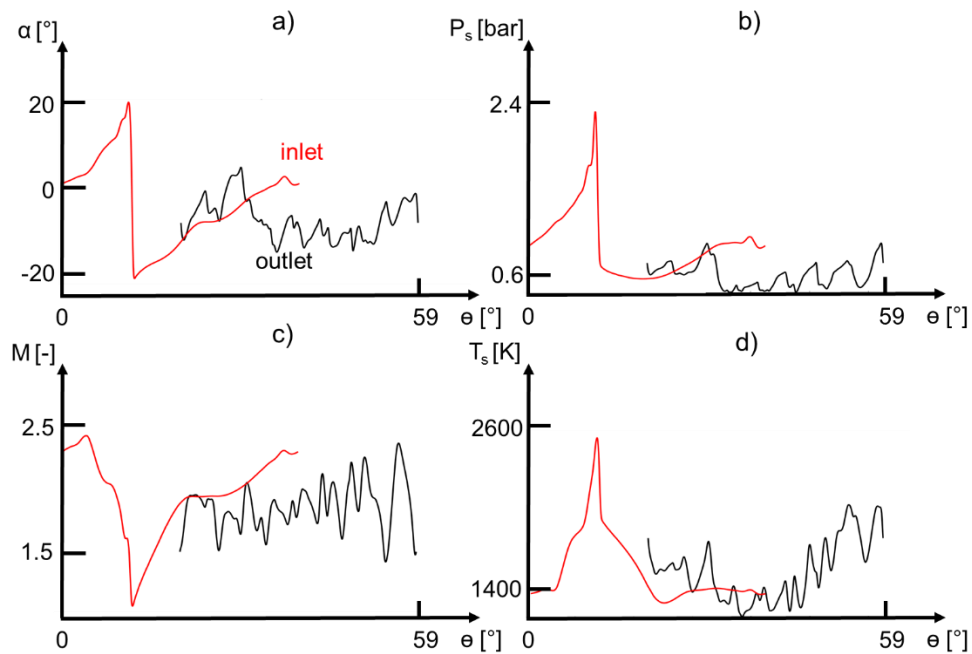


Figure 2.15. Instantaneous stage fluctuations in function of the azimuthal angle: a) flow angle, b) static pressure, c) Mach number, and d) static temperature ($\bar{f}=0.24$, $\bar{A}=1$).

Table 2.4: Instantaneous stage damping ($\bar{f}=0.24$, $\bar{A}=1$).

$\zeta_{stage,\alpha}(t)$	78.1%
$\zeta_{stage,Ps}(t)$	56.0%
$\zeta_{stage,M}(t)$	26.6%
$\zeta_{stage,Is}(t)$	32.0%

Figure 2.16a shows the instantaneous flow field of the stage at midspan. Two points were selected at the stator inlet and rotor inlet respectively for the frequency analysis. Figure 2.16b depicts the frequency spectrum of static pressure at stator inlet and rotor inlet for $\bar{f}=0.24$ and $\bar{A}=1$. The dominant frequency at the stator inlet is identified as the frequency at which the oblique shock waves impact the turbine, which is $6.3\pm 0.5\text{kHz}$. Due to the strong gradient of pressure at the inlet, one can observe more than 10 harmonics of the dominant frequency. By contrast, at the rotor inlet the amplitude of the pressure fluctuations was decreased by 41.7%. At the rotor inlet one can observe that the first harmonic was attenuated by 17.4%.

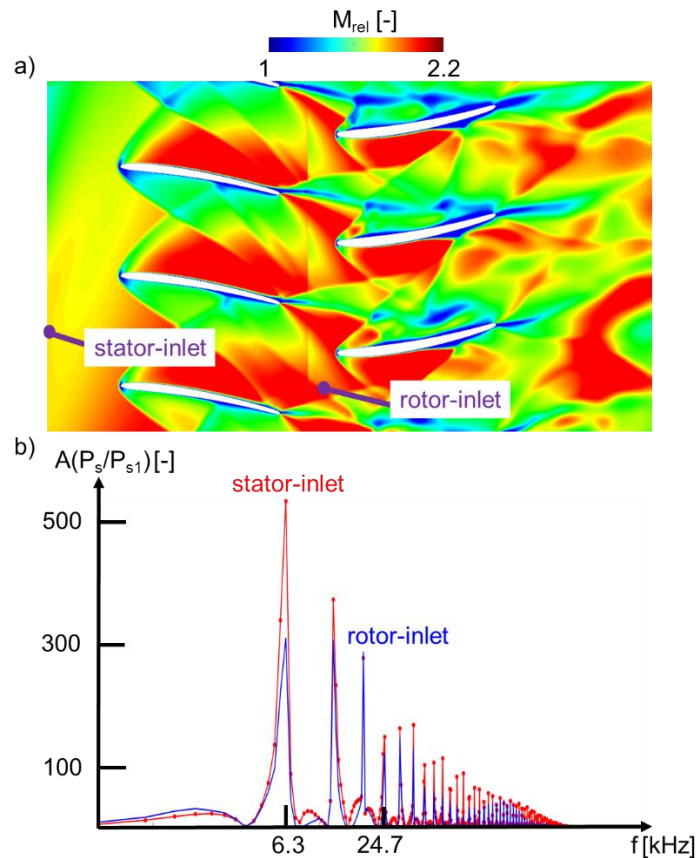


Figure 2.16. a) Instantaneous flow field of the URANS stage simulation at midspan ($\bar{f}=0.24$, $\bar{A}=1$). b) Frequency spectrum of static pressure at the stator inlet and rotor inlet.

Loss budgeting of the unsteady stage was performed to characterize the loss contribution from each source. The shock loss and viscous loss were evaluated through the model developed by Sousa et al. [45]. The shock loss was based on correlations from Moeckel [46] while the viscous and mixing loss were based on correlations proposed by Stewart [47] and Startford et al. [48]. Secondary flow losses were estimated by using Kacker-Ocappu [49] correlations. Estimation of the loss mechanism is summarized in Table 2.5. The leading edge shock loss is the prime source. Since the flow turning was less than 20° in the stator, secondary flow effects were minor. The viscous and mixing loss due to the growth of the boundary layer along the blade surface as well as the mixing effect downstream of the blade was approximately 6% for rotor and stator. The difference between the total losses and the summation of the presented values is the effect of unsteady interaction, 4.9% for the stator and 8.3% for the rotor.

Table 2.5: Budgeting of the unsteady total pressure loss due to shock waves, viscous, mixing, and secondary flow across the stator and rotor ($\bar{f}=0.24$, $\bar{A}=1$).

	stator	rotor
Y_{shock}	11.1%	10.5%
$Y_{\text{viscous+mixing}}$	6.1%	6.1%
$Y_{\text{secondary}}$	1.0%	1.6%
$Y_{\text{unsteady_interaction}}$	4.9%	8.3%
Y_{Total}	23.1%	26.5%

2.3 Performance Map

When exposed to periodic inlet oblique shocks, the supersonic turbine does not always operate at the design condition. Therefore, it is critical to investigate the turbine aerodynamic performance at off-design condition and to explore the limit of the operating range. For supersonic flows, static quantities and velocity are prescribed at stator inlet, while the rotor outlet boundary condition is set to interpolate from the internal field. To simulate the off-design environment, the rotor RPM ranges from 60% to 120% of nominal condition. For each RPM, the inlet static pressure varies from 60% to 120% of the nominal condition. In total 49 RANS simulations were carried out.

Figure 2.17a plots the total-to-total pressure ratio across the stage as a function of the corrected mass flow (Eq. 2.18). The corrected mass flow is unchanged, indicative of a supersonic passage. The pressure ratio variation across the supersonic stage is minor, ranging from 1.84 to 1.94. Figure

2.17b depicts the total temperature drop across the stage non-dimensionalized by the inlet total temperature, evaluated at various product of the corrected mass flow and corrected speed (Eq. 2.16). For a certain RPM, increased inlet static pressure enhances the pressure force exerted on the blade and consequently the torque, resulting in the work increase. For a certain inlet static pressure, angular momentum is enhanced as RPM increases, extracting more work.

$$\bar{m} = m \frac{\sqrt{T_{01}}}{P_{01}} \quad (2.16)$$

$$\bar{n} = \frac{\omega}{\sqrt{T_{01}}} \quad (2.17)$$

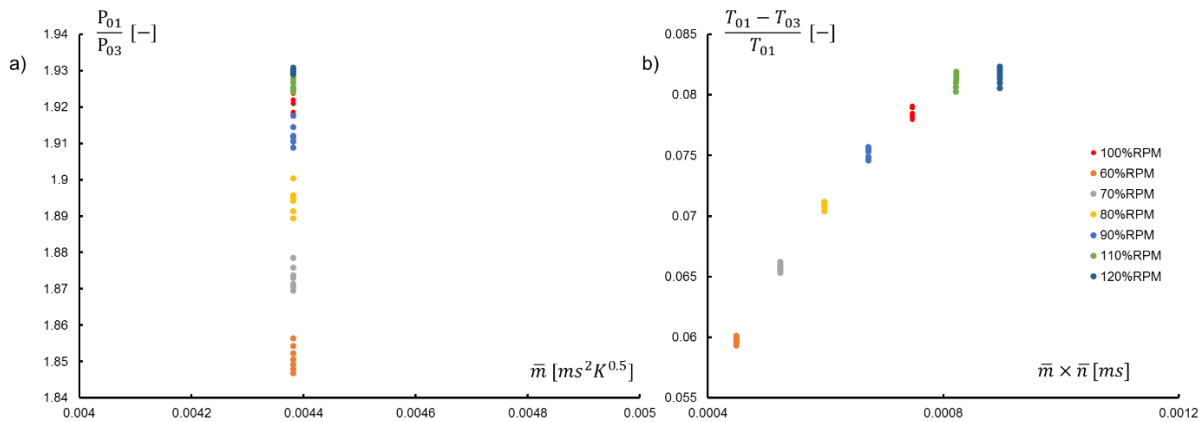


Figure 2.17. a) Total-to-total pressure ratio in function of the corrected mass flow. b) Non-dimensional total temperature difference in function of the product of corrected mass flow and corrected speed.

2.4 Unsteady Heat Transfer Assessment

The supersonic outlet conditions from a nozzle downstream of a RDC induces a large convective heat loading onto the downstream axial turbine. In this section, the convective heat flux is quantified to provide a detailed understanding of the underlying physics, for use in the design of adequate cooling schemes to manage the thermal loads, high and low cycle fatigue, and creep.

2.4.1 Span-wise Heat Flux Fluctuations

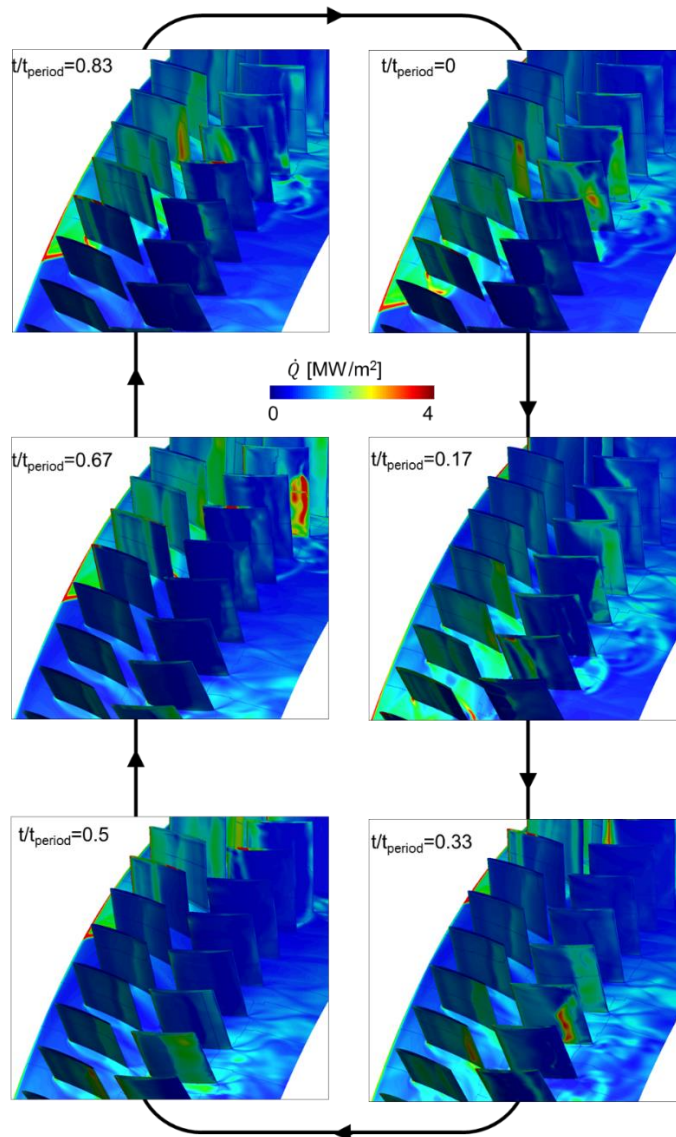


Figure 2.18. Instantaneous heat flux pattern for a wall temperature of 1800K.

Two isothermal simulations of the supersonic axial turbine exposed to nozzle outlet conditions are performed at two constant wall temperature: 1400K and 1800K. Figure 2.18 illustrates the instantaneous heat flux pattern for one oblique shock revolution for a wall temperature of 1800K. Heat flux magnitude is gradually attenuated across the stator channel until a reflected shock from the adjacent stator impinges. Throughout the rotor passage, the suction side is periodically swept by the upstream trailing edge shock and zones of large heat flux are identified downstream close

to the rotor trailing edge, owing to the shock boundary layer interaction generated by the reflected shock from the neighboring rotor.

The transient heat flux over the entire span on the leading edge of stator vanes and rotor blades is analyzed to locate the peak spot. At a wall temperature of 1400K, due to direct exposure to the inlet oblique shock, a uniform distribution of heat flux is displayed all over the vane span (Fig. 2.19b), with the maxima occurring upon the impingement of the inlet oblique shock. Downstream at the rotor leading edge, a large heat flux is observed at multiple time instants (Fig. 2.19c) due to the sweeping by the upstream stator trailing edge shock and blade rotation.

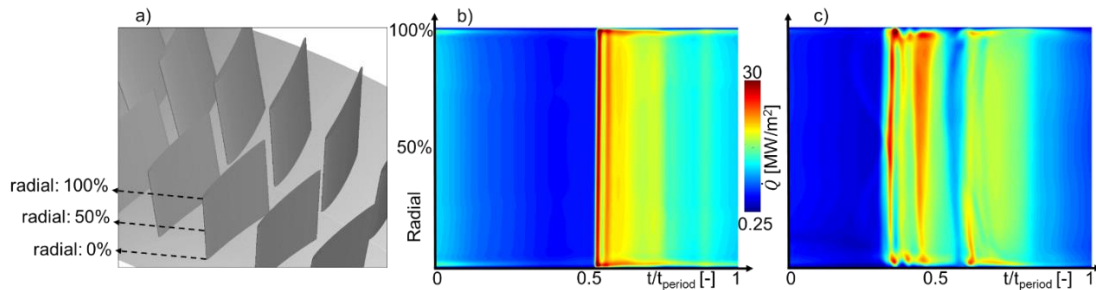


Figure 2.19. At a wall temperature of 1400K: a) Snapshot of the stator and rotor. Span-wise heat flux variation at: b) stator leading edge and c) rotor leading edge.

At the stator trailing edge (Fig. 2.20b), the unsteady heat flux is significantly attenuated thanks to the boundary layer effect along the vane, compared to the leading edge intensity. A symmetric pattern is observed, with maxima close to the mid-span. Downstream at the rotor trailing edge (Fig. 2.20c), peak heat flux occurs near the shroud, due to the shock boundary layer interaction.

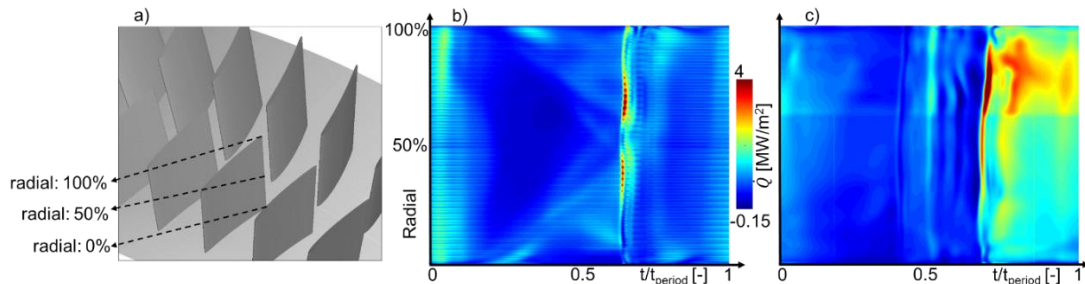


Figure 2.20. At a wall temperature of 1400K: a) Snapshot of the stator and rotor. Span-wise heat flux variation at: b) stator trailing edge and c) rotor trailing edge.

2.4.2 Stream-wise Heat Flux Variation

The design of suitable cooling scheme for the vane and blade requires the detailed assessment of the stream-wise heat flux variation, particularly in this case where a strong periodic oblique shock originates from the inlet and multiple reflected shocks are induced. Figure 2.19 plots the heat flux distribution at mid-span along the stream-wise direction in terms of the maxima in an oblique shock period at a wall temperature of 1400K. The stator suction side suffers higher maximum heat flux than the pressure side due to the periodic invasion of the inlet oblique shock (Fig. 2.21a). The heat flux generally declines towards the trailing edge. However, the reflected shocks from the adjacent stator gave rise to additional peaks observed after the mid-chord on the suction side and close to the trailing edge on the pressure side. Similar characteristics were identified at 25% span and 75% span. Downstream in the rotor (Fig. 2.21b), the leading edge maximum heat flux was reduced by 4% compared to the stator. On the aft part of the suction side, peak heat flux was observed close to the trailing edge due to the shock boundary layer interaction, which created separation both upstream and downstream of the impingement location and leads to the heat flux variation.

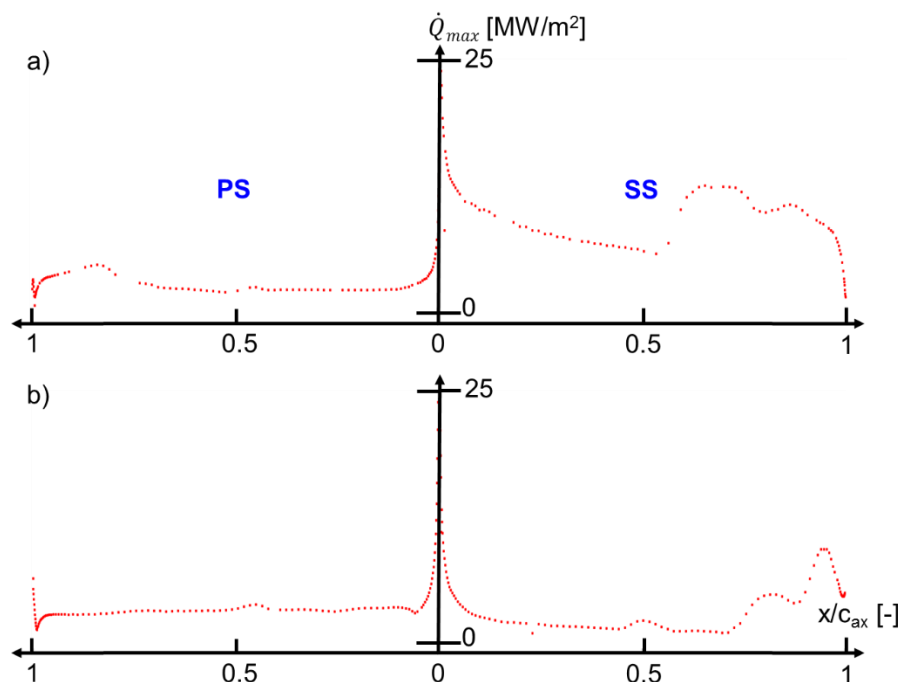


Figure 2.21. At a wall temperature of 1400K: stream-wise heat flux variation at mid-span of a) stator and b) rotor.

Table 2.6 summarizes the integral heat load of the axial turbine evaluated at steady and unsteady operation. The steady boundary conditions were obtained by performing a cycle-mass-averaged of mass-flow-averaged evaluation of the inlet quantities of the unsteady simulation. The time-averaged integral heat load for the unsteady simulations was computed via Equation (2.18). At a wall temperature of 1400K, due to the unsteadiness, the stator heat load is decreased by 2.4% (~0.2 kW). However, as wall temperature increased to 1800K and heat flux magnitude descends, in the unsteady case the stator heat load is 0.1 kW higher thanks to the unsteadiness.

$$\int \dot{Q} = \text{mean}(\int \dot{Q}(t)_{endwalls} + \int \dot{Q}(t)_{blade}) \quad (2.18)$$

Table 2.6: Comparison of the integral heat load between steady and unsteady simulations.

	T_w=1400K		T_w=1800K	
	stator	rotor	stator	rotor
steady	9.65 kW	10.22 kW	5.66 kW	5.71 kW
unsteady	9.42 kW	10.26 kW	5.79 kW	6.1 kW

2.4.3 Time-Resolved Adiabatic Wall Temperature

Figure 2.22a plots the mid-span time-resolved heat flux on the stator leading edge. The instantaneous heat flux at the end of the period is displayed in Fig. 2.22b, where a linear interpolation is performed to retrieve an adiabatic wall temperature of 2440K and an adiabatic heat transfer coefficient of 9240W/(m².K). Afterwards, this linear interpolation of the unsteady heat flux is repeated for all time instants, which leads to a heat flux surface shown in Fig. 2.22c. The intersection of this surface with the zero heat flux plane results in the time-resolved adiabatic wall temperature depicted in Fig. 2.22d.

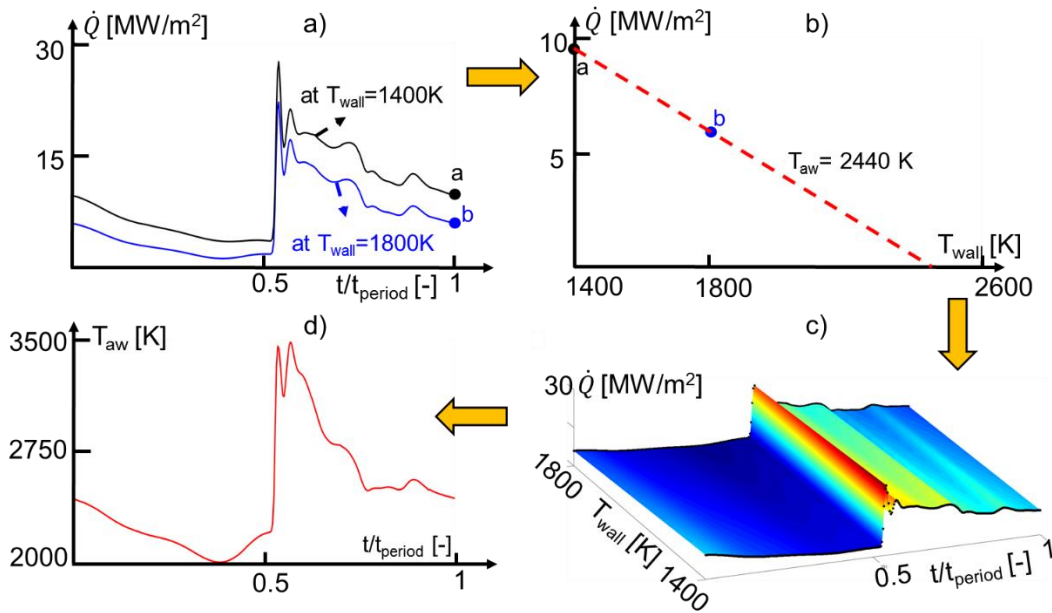


Figure 2.22. Stator leading edge at mid-span: a) Time-resolved heat flux. Linear interpolation of b) the instantaneous heat flux and c) at all time instants. d) Time-resolved adiabatic wall temperature.

To assess the uncertainty of this method, Fig. 2.23 plots the mid-span adiabatic wall temperature evaluated based on two simulations with constant wall temperature compared to the static temperature retrieved from an adiabatic simulation at the stator leading edge (Fig. 2.23a) and rotor leading edge (Fig. 2.23b). The adiabatic wall temperature method predicts the trend well, however a discrepancy was found when the oblique shock impacted on the blade as well as in the post-shock period due to the different boundary layer characteristics for the adiabatic and isothermal simulations.

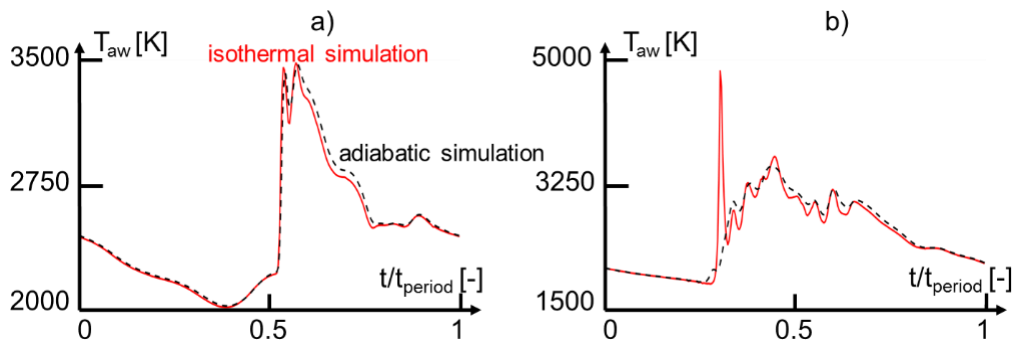


Figure 2.23. Verification of the adiabatic wall temperature at mid-span of a) stator and b) rotor.

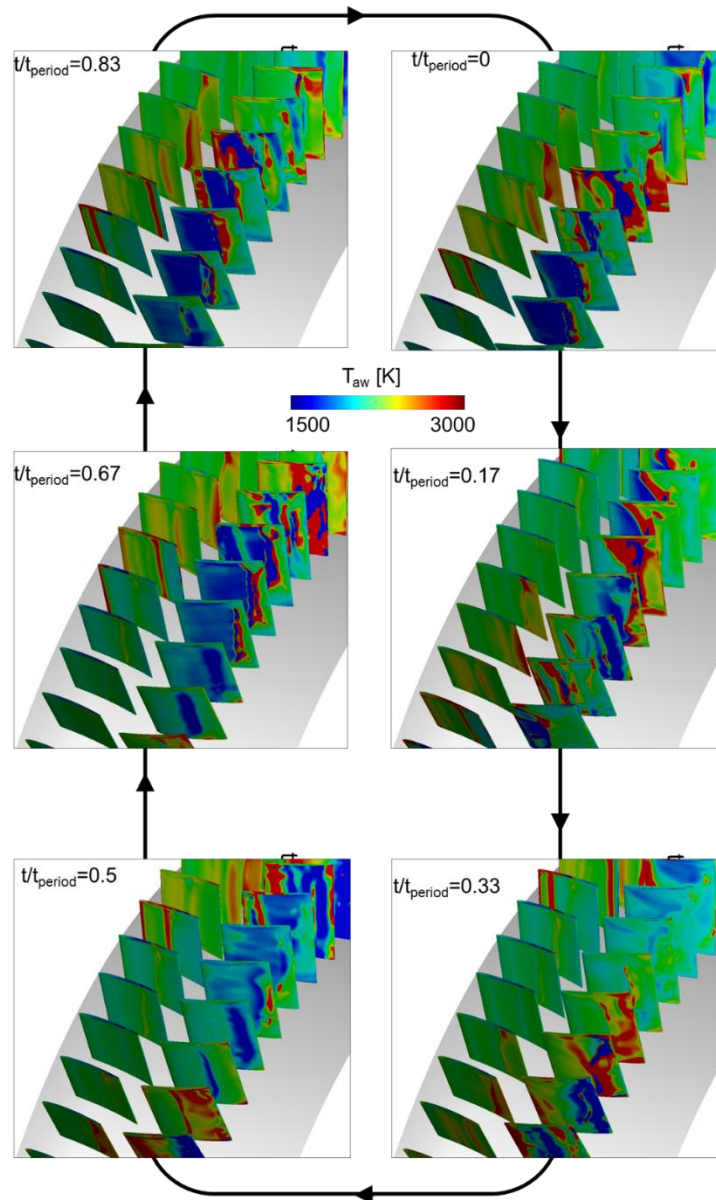


Figure 2.24. Instantaneous adiabatic wall temperature.

With the same procedure, the time-resolved adiabatic wall temperature of an entire vane/blade is acquired. Figure 2.24 displays the instantaneous adiabatic wall temperature for an oblique shock revolution passing through the computational domain. Similar to the unsteady heat flux pattern, periodic sweeping of the oblique shock creates adiabatic temperature variation in the azimuthal direction. Along the stream-wise direction, influence of the reflected shocks generates local maxima on both suction side and pressure side, as indicated in Fig. 2.18. However, the adiabatic wall temperature may not be the only driving source of the heat transfer, as the boundary layer

characteristics alter the local heat transfer coefficient as well. Therefore, a careful budgeting of the unsteady heat flux mechanism is needed.

2.4.4 Budgeting of the Unsteady Heat Flux Mechanism

Decomposition of the unsteady heat flux allows for identification of the source of unsteadiness, which can consequently be used to develop suitable cooling strategies. The unsteady heat flux (Equation 2.19) can be decomposed into a time-averaged term (Equation 2.20) and an unsteady term with zero mean (Equation 2.21) according to Pinilla et al. [50].

$$\dot{Q} = \bar{Q} + Q' = (\overline{h_{aw}} + h'_{aw})(\overline{T_{aw}} + T'_{aw} - T_w) \quad (2.19)$$

$$\bar{Q} = \overline{h_{aw}}(\overline{T_{aw}} - T_w) + \overline{h'_{aw}T'_{aw}} \quad (2.20)$$

$$Q' = \overline{h_{aw}}T'_{aw} + h'_{aw}(\overline{T_{aw}} - T_w) + h'_{aw}T'_{aw} \quad (2.21)$$

Where the first term on the right side of Equation (2.21) represents the unsteady flow temperature effect (“driving temperature”), the second term denotes the unsteady boundary layer effect, and the third term stands for the joint effect of the unsteady flow temperature and unsteady boundary layer. In Equation (2.20), the time-averaged heat flux was obtained through RANS simulations, where the inlet boundary conditions were acquired by taking cycle-mass-averaged of mass-flow-averaged of inlet profiles from URANS simulations.

Figure 2.25a depicts the investigated locations along the stator pressure side. Figure 2.25b-c plots the unsteady static pressure and unsteady Reynolds number, which reveal the passage of the shock wave, and the unsteady convective heat transfer coefficient. The unsteady heat transfer coefficient, also called boundary layer contribution to the unsteady heat flux in Equation (2.21), follows closely the pressure and Reynolds number fluctuations.

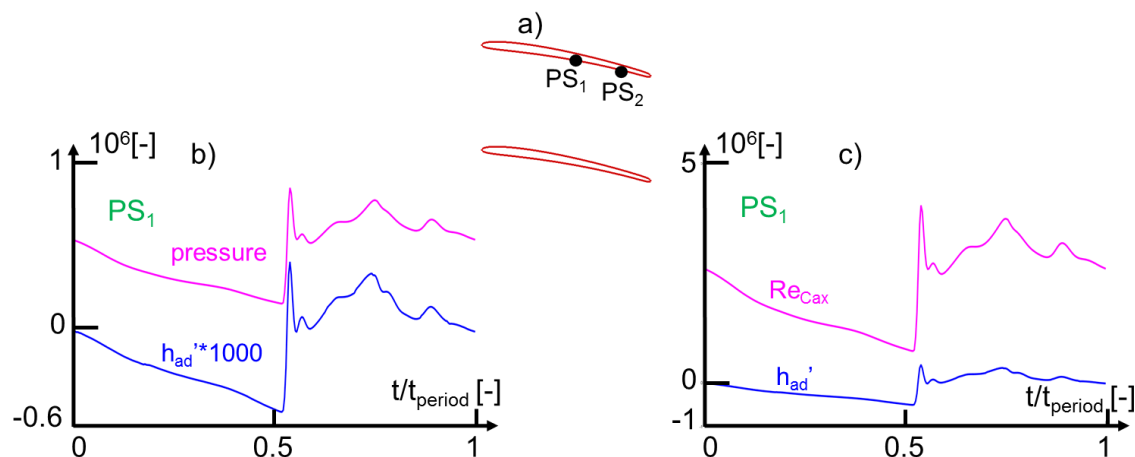


Figure 2.25. Stator at mid-span for a wall temperature of 1400K: a) Measurement locations. At PS₁: b) Unsteady static pressure and unsteady adiabatic heat transfer coefficient and c) unsteady Reynolds number and unsteady adiabatic heat transfer coefficient.

Figures 2.26a-b depict the different contributions to the unsteady heat transfer extracted from around mid-chord locations of the stator depicted in Fig. 2.25a. At mid-chord 'PS₁', the unsteady flow temperature effect is the main contribution to the unsteady heat flux, and the combined effect is minor. It is observed that the boundary layer effect counteracts the influence of the driving temperature upon arrival of the shock, hence reducing the overall detrimental effect of the impinging transient shock with a decrease in instantaneous heat transfer coefficient (h_{aw}'). Downstream at 'PS₂', due to the growth of the boundary layer, the intensity of heat flux is reduced upon the arrival of the oblique shock and the combined effect is larger. However, owing to the reflected shock from the adjacent stator, a dramatic increase of the flow temperature effect is observed closed to the end of the inlet oblique shock period, counteracted by the combined effect.

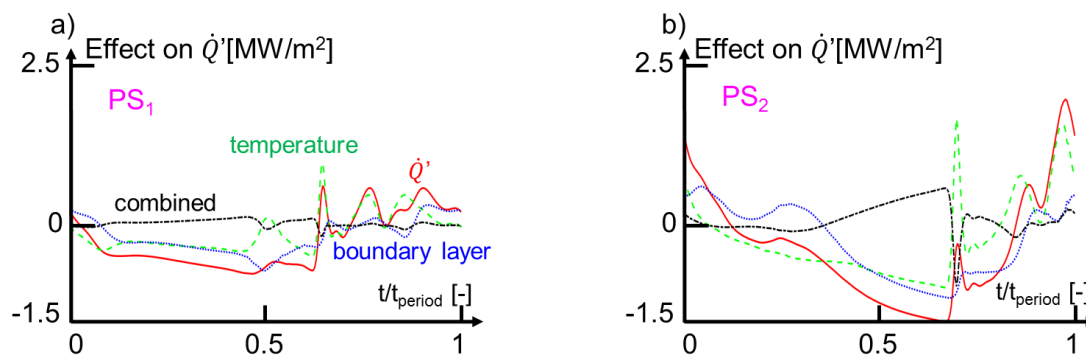


Figure 2.26. Stator at mid-span for a wall temperature of 1400K: Contribution to Q' at a) PS₁ and b) PS₂.

Likewise, at around mid-chord of the rotor (Fig. 2.27a-b), the unsteady adiabatic wall temperature accounts for 81% of the unsteady heat flux when the upstream inlet shock signs in. While this temperature effect is again negated by the effect of the unsteady boundary layer (8%), through the combined term (11%). In sum, the adiabatic wall temperature is the driving factor for the unsteady heat flux pattern. However, this deteriorate effect from the oblique shock is balanced at some locations due to a reduction in the local heat transfer coefficient.

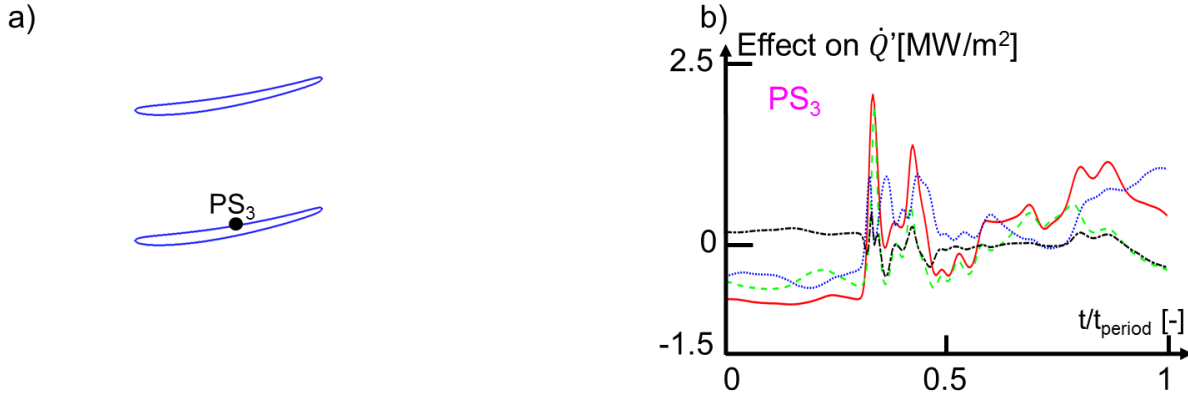


Figure 2.27. Rotor at mid-span for a wall temperature of 1400K: a) Measurement locations. b) Contribution to \dot{Q}' at PS_3 .

3. RETROFIT AN EXISTING SUBSONIC AXIAL TURBINE WITH ENDWALL CONTOURING

In this chapter, firstly an existing subsonic axial turbine is modified to be integrated with a diffuser and a rotating detonation combustor, by the stator endwall diffusion without redesigning the turbine passages and airfoils. The modified subsonic turbine was submitted to diffuser outlet fluctuations at a wide range of frequencies, amplitudes, and two Mach numbers and the performance is characterized with an increased level of modeling fidelity. Afterwards, the modified endwall contouring is optimized through a multi-step approach to enable the retrofit of the existing subsonic turbines with rotating detonation combustors. A performance map is constructed to assess the selected optimized subsonic turbine at off-design condition. Finally, an experimental campaign to replicate the flow diffusion in the optimized turbine is proposed in the Purdue Experimental Turbine Aerothermal Laboratory (PETAL) linear wind tunnel.

3.1 Turbine Geometry and Boundary Conditions

3.1.1 Computational Domain

The stator endwalls of a transonic turbine were modified to ingest high Mach inflow. Table 3.1 shows the geometric parameters of the investigated turbine from which the stator and rotor profiles were unaltered. Figure 3.1a displays the computational domain with an inlet area opening of 70% for a Mach 0.6 inflow, with the close-up view of grid topology at the stator leading edge (Fig. 3.1b) and at the rotor trailing edge (Fig. 3.1c). A structural mesh was created with Autogrid5 developed by NUMECA International containing 7 M cells. A mixing plane was set between the stator and rotor which conducted the pitch-wise averaging of the stator outlet fluctuations and disseminated results to the rotor. Thermally perfect gas (air) was selected as working fluid. The stator exit Reynolds number in terms of the chord was around 2.23×10^6 .

Table 3.1: Turbine geometric parameters at mean radius.

	stator	rotor
C [mm]	92.88	62.22
g/C [-]	0.75	0.75

Table 3.1: Continued.

w/g [-]	0.28	0.4
h/c [-]	0.69	0.95
Stagger angle [deg]	52	32
Number of vane / blade	43	64
RPM [-]	-	10421

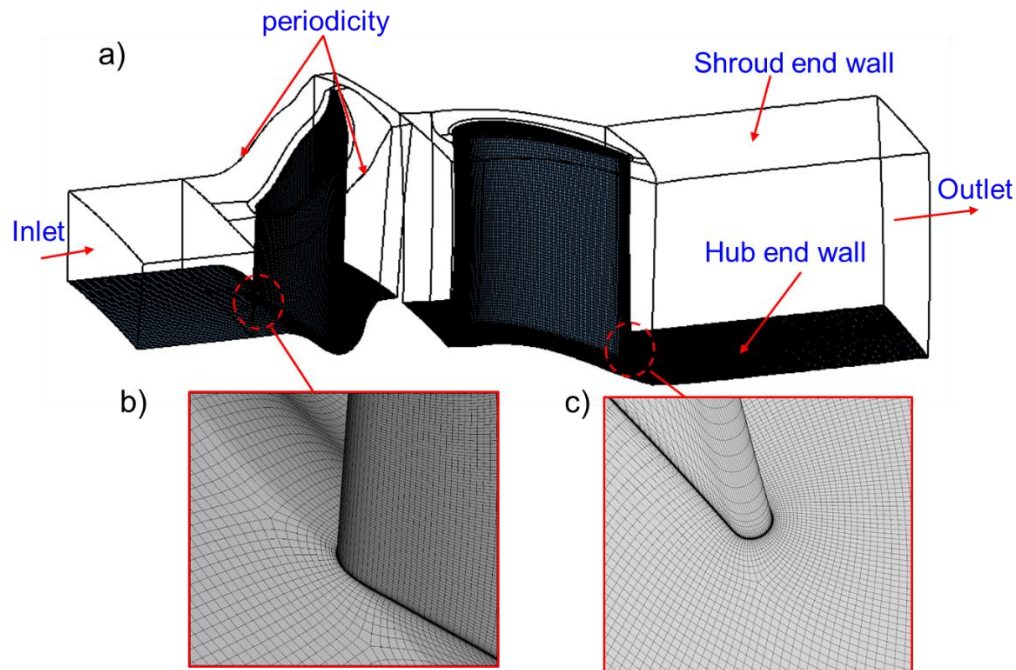


Figure 3.1. a) Computational domain of the turbine stage for a Mach 0.6 inflow. A close-up view of the b) stator leading edge and c) rotor trailing edge.

3.1.2 Grid Sensitivity

A mesh independence study was conducted on the investigated turbine (Fig. 3.1a) with four mesh levels ranging from 2.2 million cells (coarser) to 9.4 million cells (fine). For the steady simulations, constant total pressure and total temperature were prescribed at the stator inlet and a constant static pressure was imposed at the rotor outlet ($P_{01}/P_3=3$). Figure 3.2a plots the decay of rotor outlet total temperature, with a discrepancy of 0.01% going from the medium level to the fine level. The extrapolated error [41][51] of the rotor outlet total temperature was evaluated for all grid levels and results are displayed in Fig. 3.2b. The extrapolated error of medium mesh is identified as 0.038%, with a grid convergence index (GCI) of 0.036%. Therefore, the medium mesh was selected for the turbine stage assessment. Figure 3.2c depicts the evolution of mass flow

rate probed at stator inlet and rotor outlet evaluated under the medium mesh. The discrepancy of mass flow rate between stator inlet and rotor outlet is less than 0.65%, indicating that convergence was achieved for the steady case.

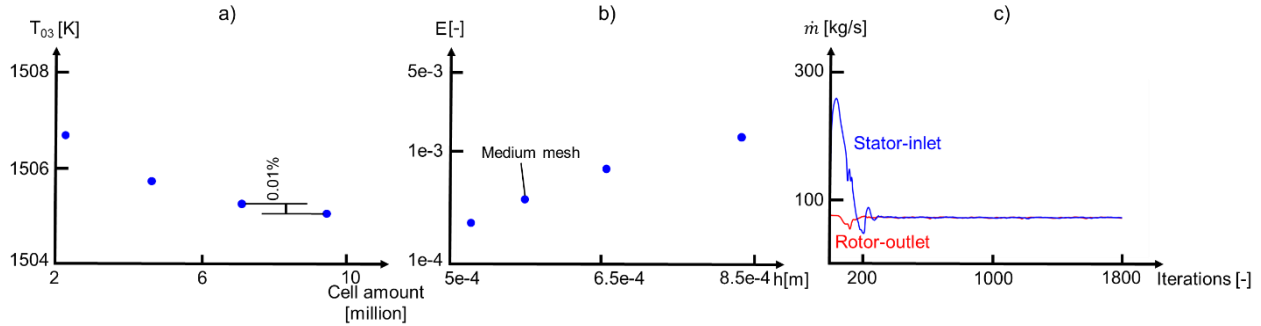


Figure 3.2. a) Rotor outlet total temperature in function of the cell count. b) Log-log plot of the numerical extrapolated error of rotor outlet total temperature in function of the representative grid size. c) Evolution of the mass flow rate at stator inlet and rotor outlet.

3.1.3 Time Step Convergence

For unsteady simulations, fluctuations of total pressure and total temperature were prescribed at the stator inlet while maintaining constant static pressure at the rotor outlet. Inlet pulsations across the stator were circumferentially averaged in the mixing plane and then conveyed to the rotor. Total pressure fluctuations were imposed as defined in Eq. 3.1 at five frequencies ($f= 100\text{Hz}$, 1kHz , 2kHz , 5kHz , and 10kHz), three peak-to-mean amplitudes ($A= 15\%$, 25% and 37.5%), and two inlet Mach number: 0.3 and 0.6 .

$$P_{01} = P_{0m} + (A \times P_{0m}) \times \sin 2\pi f \quad (3.1)$$

The total temperature fluctuations were retrieved via the isentropic relations. Figure 3.3 illustrates 4 periods of fluctuating total pressure (Fig. 3.3a) and total temperature (Fig. 3.3b) at 100Hz with a 15% peak-to-mean amplitude prescribed at the stator inlet. Computational time of a URANS stator-alone simulation was 48 hours and 96 hours for the turbine stage to achieve periodic convergence on 16 cores of one Intel Xeon-E5 processor.

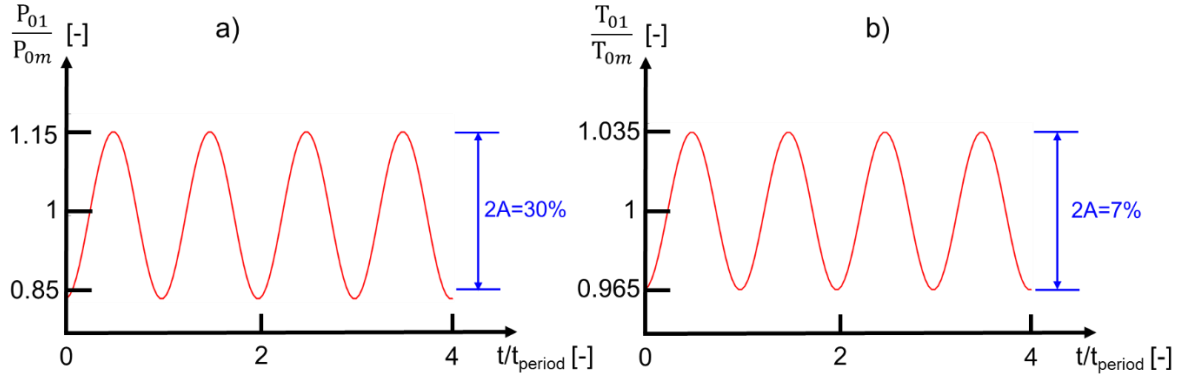


Figure 3.3. Fluctuation of a) total pressure at $f=100\text{Hz}$ and $A=15\%$ and b) total temperature at $A=3.5\%$ imposed at the stator inlet.

A time step sensitivity analysis was performed by discretizing the sinusoidal wave with 20, 30, and 60 inner time steps per period. Figure 3.4 depicts the stator outlet total pressure at a frequency of 1 kHz with an inlet peak-to-mean amplitude of 15% for one cycle assessed at different discretized time steps. A deviation of 8% is found when 20 time steps per cycle is used compared to 30 time steps per cycle (Fig. 3.4a). However by using 60 time steps, the discrepancy is decreased to 0.6% (Fig. 3.4b). Therefore, total quantities fluctuations were discretized with 30 time steps for all URANS simulations.

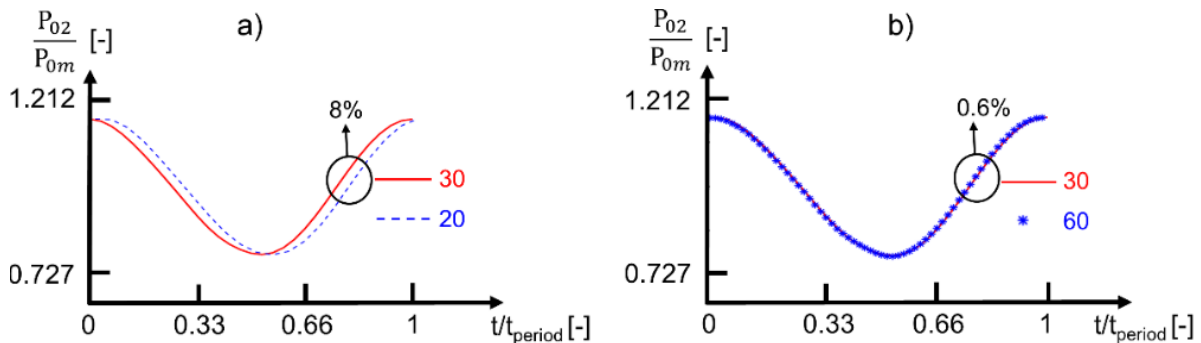


Figure 3.4. One period ($f= 1\text{kHz}$, $A=15\%$) with a) 20 vs. 30 discretized time steps and b) 30 vs. 60 discretized time steps.

3.1.4 Periodic Convergence

The method of Clark and Grover [42] was used to assess the unsteady convergence. The theory was developed based on signal processing and fuzzy logic principles. A series of fuzzy sets were created for the time-dependent mass-flow-averaged total pressure ($\bar{P}_{02_current}(t)$) at the stator outlet.

The membership grade in a series of fuzzy is defined by mean-level static pressure fluctuations, the Discrete Fourier Transform (DFT) amplitude, and phase which were assessed for two consecutive cycles. Through DFT, the frequency of the flow field unsteadiness was retrieved. The membership grade of the fuzzy set was computed through a cross-correlation coefficient for two consecutive cycles and was evaluated to measure the similarity between the expected periodic signals and the previous computed ones. An overall membership grade of all calculated fuzzy sets was analyzed by employing a multi-valued logic [43]. The URANS stage simulation at a frequency of 1 kHz with 15% peak-to-mean amplitude for an inlet Mach number of 0.3 was selected for the convergence analysis. The membership grade of each fuzzy set was greater than 0.9999, where the overall unsteady convergence is defined when the overall membership grades was higher than 0.95. This evaluation was repeated for all URANS cases to ensure periodic convergence.

3.2 Endwall Contouring to Ingest High Subsonic Flow

3.2.1 Axisymmetric Endwall Contouring to Prevent Choking

The three different endwall (EW) designs were labelled as EW1, EW2, and EW3 in Fig. 3.5a and each one is specified by a different throat-to-inlet area ratio. Fig. 3.5b presents the evolution of the stator area along the passage. The endwall opening was carefully selected based on the isentropic limit, which correlates the maximum local Mach number with the throat-to-local area ratio to prevent turbine unstarting due to an excess of mass flow. Three area ratios were selected: EW1 for Mach numbers up to 0.17, EW2 for a Mach number up to 0.35 and EW3 for a Mach number of 0.76. Figure 3.5c plots the theoretical maximum inlet Mach number according to the throat to inlet area ratio for the aforementioned three endwall profiles.

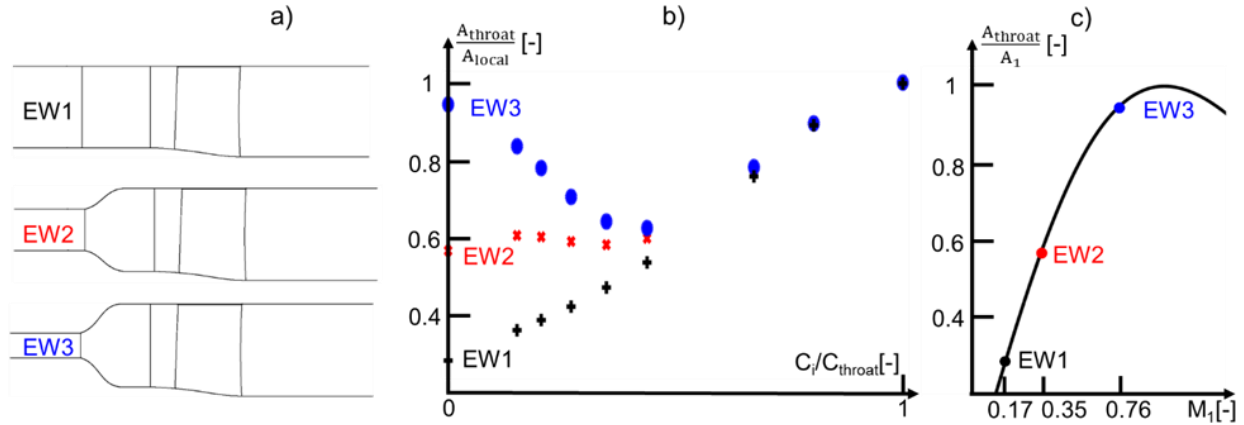


Figure 3.5. a) Cross sections of the three different endwall designs. b) Throat-to-local area ratio. c) Throat-to-inlet area ratio in function of the inlet Mach number.

3.2.2 Performance Analysis

To quantify the turbine performance, turbine thermodynamic efficiency and kinetic energy loss coefficients were evaluated. Lee et al. [52] reported that the instantaneous turbine efficiency could exceed unity. Therefore, to compute the kinetic energy loss coefficients and thermodynamic efficiency, all quantities were first mass flow averaged over the locations of interest per time step and then cycle mass averaged over a selected period. First, the stator and rotor outlet isentropic velocity were evaluated with the assumption of the isentropic expansion within the passages through Equation (3.2-3.5):

$$T_{2_{is}} = T_{01} \left(\frac{P_2}{P_{01}} \right)^{\frac{\gamma-1}{\gamma}} \quad (3.2)$$

$$V_{2_{is}} = 2C_p(T_{01} - T_{2_{is}}) \quad (3.3)$$

$$T_{3_{is}} = T_{02R} \left(\frac{P_3}{P_{02R}} \right)^{\frac{\gamma-1}{\gamma}} \quad (3.4)$$

$$W_{3_{is}} = 2C_p(T_{02R} - T_{3_{is}}) \quad (3.5)$$

Afterwards, the calculated isentropic outlet velocity was plugged into Equation (3.6) and Equation (3.7) to evaluate the kinetic energy loss coefficient. The kinetic energy loss coefficients of the stator and rotor are defined as:

$$\zeta_S = \left(\frac{V_{2_is}}{V_2} \right)^2 - 1 \quad (3.6)$$

$$\zeta_R = \left(\frac{W_{3_is}}{W_3} \right)^2 - 1 \quad (3.7)$$

The thermodynamic efficiency of the entire turbine stage is defined as:

$$\eta_{thermodynamic} = \frac{T_{01} - T_{03}}{T_{01} - T_{03_is}} \quad (3.8)$$

The Horlock estimation [53], in terms of the kinetic losses from individual rotor and stator simulations, is defined as:

$$\eta_{Horlock} = \left[1 + \frac{\frac{T_3}{T_2} \zeta_S V_2^2 + \zeta_R W_3^2}{2C_p(T_{01} - T_{03})} \right]^{-1} \quad (3.9)$$

At steady state, the Horlock estimation and thermodynamic efficiency were assessed and summarized in Table 3.2.

Table 3.2: Evaluation of turbine efficiency at steady state.

	EW2	EW3	EW1 (Mach inlet=0.3)	EW1 (Mach inlet=0.6)
ζ_S	7.2%	21.2%	-	-
ζ_R	9.1%	17.8%	-	-
$\eta_{Horlock}$	91.8%	81.5%	-	-
$\eta_{thermodynamic}$	91.2%	79.9%	64.7%	49.7%

The deviation between the Horlock estimation and the thermodynamic efficiency is 0.6 percentage-points for EW2 at a reduced computational cost of 6 hours. The use of the Horlock estimation allows to predict the turbine stage efficiency based on a single row calculation of the stator and a single row calculation of the rotor. At steady state, the computational time for EW2 to reach convergence was around 16 hours on 16 cores of one Intel Xeon-E5 processor . However, for a single stator row or a single rotor row, the computational burden was reduced to 5 hours. An increase of the endwall diffusion from EW2 to EW3 leads to an increase in stator kinetic energy loss of 14 percentage-points (Table 3.2) and subsequently results in a decrease in turbine efficiency by 11 percentage-points. When EW1 is exposed to that inlet Mach number, the turbine was unstarted with a consequent upstream moving pressure wave and the turbine efficiency dropped by 30 percentage-points.

Figures. 3.6a-b display the mid-span flow field of EW1 and EW2 exposed to an inlet Mach number 0.3. Figures 3.6c-d depict the flow field of EW1 and EW3 for an inlet Mach number of 0.6. EW1 is the original design and delivers a 91.9% turbine efficiency when operating at Mach 0.16 inflow. However, when exposed to the outlet conditions of diffusers, higher Mach numbers at the inlet are present. Due to accumulation of mass flow, a pressure wave was established for EW1 near the turbine inlet and consequently the turbine was unstarted. Figure 3.6e displays the mass-flow-averaged Mach number extracted along the mid-pitch (black dotted line) for EW1 and EW2. Owing to the unstarted operation, a sudden drop of the Mach number across the pressure wave was observed for an inlet Mach number of 0.3. Similarly, Figure 3.6f shows a reduction of the Mach number across the pressure wave for an inlet Mach number of 0.6, resulting in an efficiency drop from 80% down to 50%. When EW1 was exposed to the Mach 0.3 and Mach 0.6 inflow, a pressure wave was generated close to the inlet. In practice, this pressure wave tends to move upstream and is the result of mass flow accumulation, which leads to lower flow acceleration across the stator passage. As a result, the rotor is at off-design condition which significantly abated the turbine efficiency.

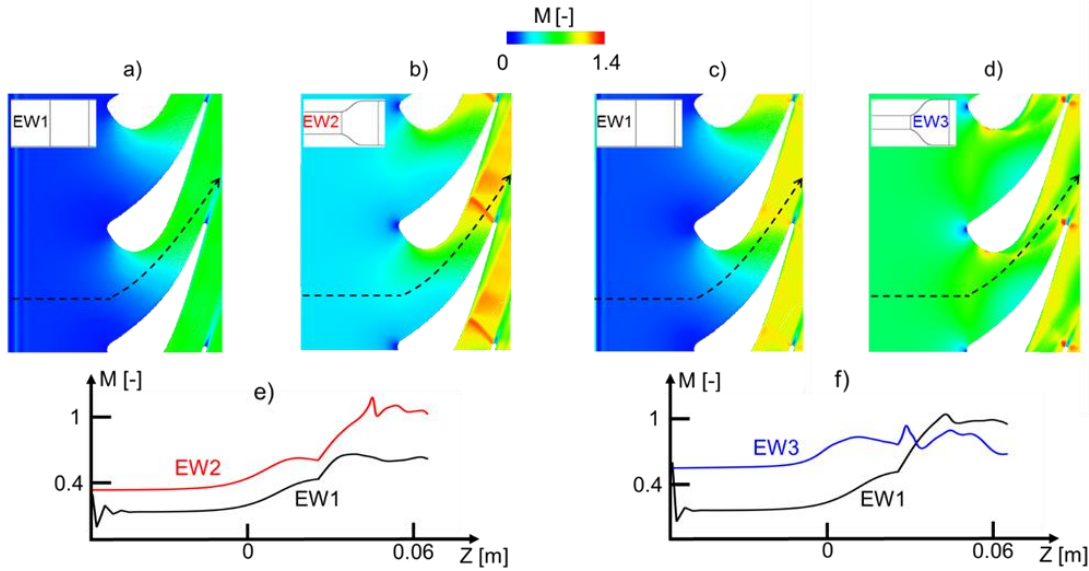


Figure 3.6. a) EW1 choked at $M1=0.3$. b) Started operation: EW2; c) EW1 choked at $M1=0.6$. d) Started operation: EW3. e) Mach number distribution along the midpitch for EW1 and EW2. f) Mach number distribution along the mid-pitch for EW1 and EW3.

Loss correlations were used to dissect the loss contribution throughout the stator passage (Table 3.3), the two-dimensional calculation agreed with the profile and mixing losses proposed by Traupel [54] and Denton [55], with a discrepancy of 1.2 percentage-point in terms of the total kinetic energy loss. The 3D stator simulation at steady conditions experienced secondary flow losses (in addition to the profile and mixing losses from the 2D simulation) and analysis of the flow field revealed separation bubbles originated from the endwalls due to a large diffusion shown in Fig. 3.7. For EW2, minor separation in terms of negative axial velocity was detected (Fig. 3.7a). The axial shear stress (τ_{ax}) non-dimensionalized by the inlet dynamic pressure was assessed to gauge the intensity of flow separation at the hub of EW2 stator (Fig. 3.7b), and 14% of hub area contains separated flow (blue negative regions). However, as diffusion increases for EW3, enhanced flow separation was found (Fig. 3.7c) and the separation zone on the hub endwall covered 29% of the total surface (Fig. 3.7d).

Table 3.3: Budgeting of loss mechanism at steady state for EW2 and EW3.

	2D RANS stator alone	3D EW2 RANS stator alone	3D EW3 RANS stator alone
ζ_s	6%	7.3%	23.3%
$\zeta_{profile_Traupel}$	4.3%	3.5%	2.5%

Table 3.3: Continued.

$\zeta_{\text{mixing_Denton}}$	2.9%	2.4%	2%
$\zeta_{\text{S-}} - \zeta_{\text{profile_Traupel-}}$ $\zeta_{\text{mixing_Denton}}$	-	1.4%	18.8%

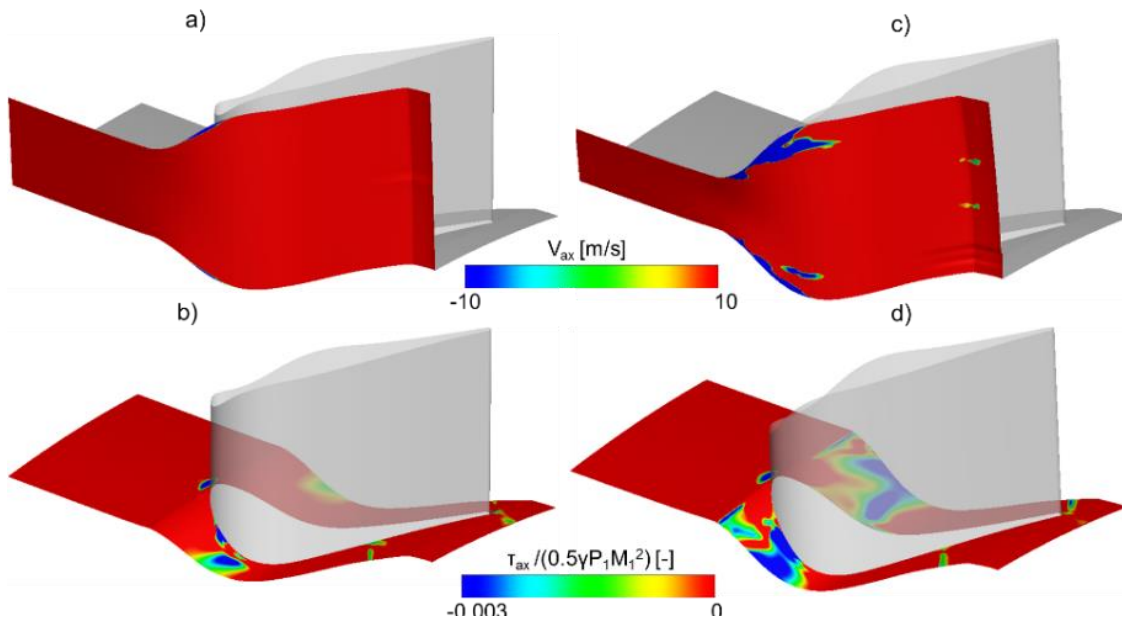


Figure 3.7. Minor flow separation in EW2: a) and b). Increased flow separation in EW3: c) and d).

3.3 Effect of Inlet Fluctuations on Efficiency and Damping

Flow separation is sensitive to the area opening, local curvature, and intensity of the secondary flows. In this section, the performance of the redesigned turbines exposed to inlet fluctuations with various frequencies and amplitudes is assessed. The turbine performance is characterized by the turbine stage efficiency and stage damping according to the inlet Mach number, oscillating amplitude, and the reduced frequency. With models of different fidelity, different physical phenomena are dissected. The Horlock estimation (Section 3.3.1) decouples the effect of the stator unsteadiness from the overall stage and assumes constant stator outlet pressure and quasi-steady operation in the rotor. The URANS stage with mixing plane approach (Section 3.3.2) couples the effects of both stator and rotor unsteadiness, but circumferentially averaged at the stator/rotor

interface. The full unsteady approach (Section 3.3.3) fully resolves the turbine stage unsteadiness, but at a high computational cost.

3.3.1 Horlock Estimation

The variation of the turbine efficiency was first analyzed via the Horlock estimation by evaluating the stator kinetic energy loss for several pulsating frequencies, amplitudes, and inlet Mach number. The rotor kinetic energy loss was taken from steady-state simulations (Table 3.2). Firstly, loss budgeting was performed for two turbines operating under the maximum reduced frequency and amplitude. However, under pulsating conditions (Table 3.4), the URANS simulation revealed up to 3 times more losses than the steady simulation and cannot be predicted by the mass-flow averaged steady secondary or profile and mixing losses. This triggered a detailed investigation of the flow, and unveiled unsteady separation bubbles shedding from the endwalls, which resulted from the interaction of the stator secondary flow and the large diffusion across the passage for EW2 and EW3.

Table 3.4: Budgeting of loss mechanism operating at a total pressure fluctuation of $A=37.5\%$ for EW2 ($\bar{f}=1.38$) and EW3 ($\bar{f}=1.26$).

	3D EW2 URANS stator alone	3D EW3 URANS stator alone
ζ_s	23.5%	39%
$\zeta_{profile_Traupel}$	2.4%	2.3%
ζ_{mixing_Denton}	3%	2.5%
$\zeta_s - \zeta_{profile_Traupel} - \zeta_{mixing_Denton}$	18.1%	34.2%

The Horlock estimation in function of reduced frequency and amplitude is illustrated in Fig. 3.8 for EW2 (Fig. 3.8a) and EW3 (Fig. 3.8b). The Horlock estimation ranges from 91.6% to 85.4% for EW2. On the other hand, the Horlock estimation of EW3 shows only a maximum of 81.7% at a reduced frequency of 0.12 and further decreases to 77.9% at a reduced frequency of 0.23. In addition, Figure 3.8a illustrates that in the regime of low reduced frequencies ($\bar{f} < 0.01$), the induced excitation travels across the stator in a quasi-steady manner as the excitation was two orders of magnitude lower compared to the speed of the convective properties. However, in the high reduced frequency range ($\bar{f} > 1$) the imposed pulsation propagated faster than the speed at which the convective characteristics travelled across the stator passage. Therefore, in this regime, the next

pulsation period was already initiated at the inlet before the previous fluctuation arrived at the outlet of the stator passage, which results in lower efficiency for high amplitudes of the fluctuations.

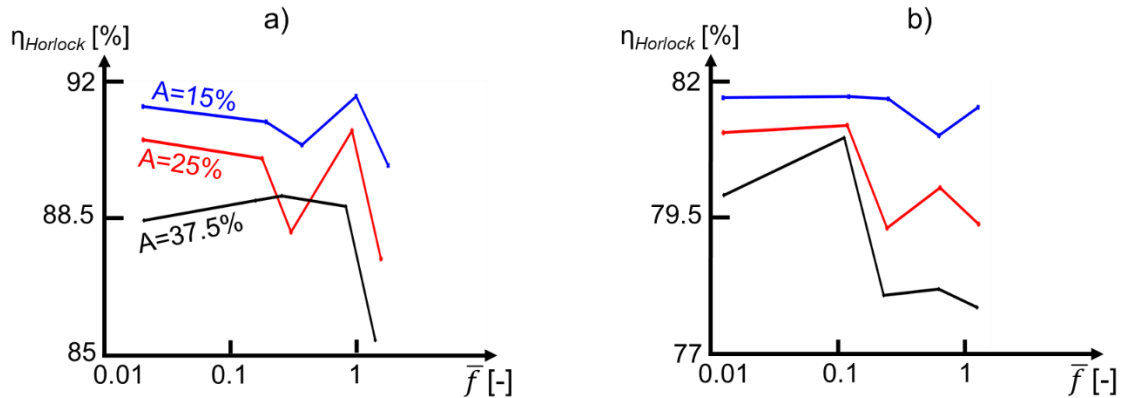


Figure 3.8. Horlock estimation in function of amplitude and reduced frequency for a) EW2 and b) EW3.

Overall, the efficiency varies around 1percentage-point if the amplitude is lower than 15%. For high amplitudes this increases to 3 percentage-points for EW2 and EW3. A drop is noted when the reduced frequency of excitation falls within the intermediate regime ($0.1 < \bar{f} < 1$), where the speed at which the flow characteristics travel throughout the passage have the same order of magnitude as the induced excitations. The acoustic resonance frequency of the computational domain (which is taken as the stator passage) is the inverse of the time required by the pressure waves which move at the speed of sound to traverse the entire computational domain. When the resonance frequency falls within the intermediate regime, an increase in the overall fluctuations across the passage is observed, resulting in the efficiency reduction.

3.3.2 URANS Stage Simulations: Mixing Plane Approach

The unsteady characteristics of the turbine stage operating at various fluctuating conditions were evaluated with the mixing plane approach for EW2 and EW3. The total pressure flow field of EW2 is depicted in Fig. 3.9. The fluctuation at the stator outlet were circumferentially averaged at the mixing plane between stator and rotor and these circumferentially averaged fluctuations are then imposed to the downstream into the rotor.

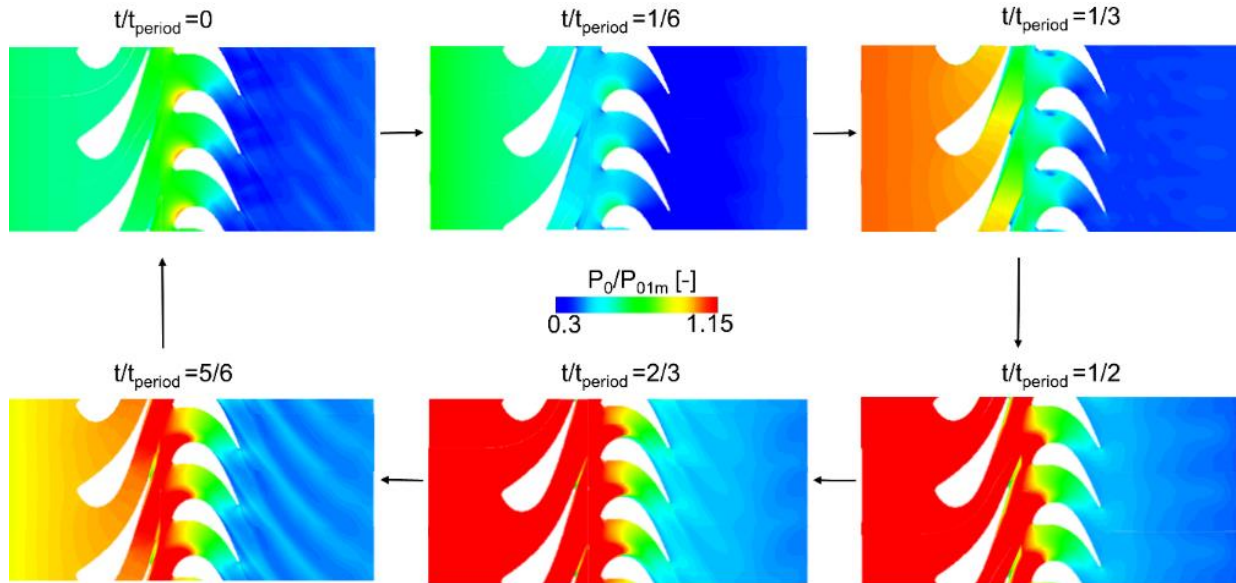


Figure 3.9. Flow field of a URANS stage simulation (mixing plane approach) of EW2 exposed to a total pressure fluctuation ($A=37.5\%$, $\bar{f}=0.15$).

Figure 3.10 displays the turbine thermodynamic efficiency at various pulsating amplitudes and reduced frequencies for EW2 (Fig. 3.10a) and EW3 (Fig. 3.10b). For EW2, the turbine efficiency ranges between 81% and 90.8%, while the efficiency of EW3 is reduced to 71.6%. Starting from the intermediate regime ($\bar{f} > 0.1$), the influence of the pulsating amplitude on the stage performance is increased. For both configurations, the difference between maximum efficiency and one at highest amplitude is around 9 percentage-points, which is not predicted by the Horlock estimation. At low reduced frequencies ($\bar{f} < 0.01$), the Horlock estimation (Fig. 3.8) predicts the turbine efficiency well. However, further increase of the reduced frequency from 1.38 to 3.47 at a peak-to-mean amplitude of 37.5% for EW2 yields in a larger efficiency discrepancy of 4.4 percentage-points. Hence, the unsteady phenomena in the rotor is needed to assess the stage performance at high reduced frequencies and large amplitudes. Additionally, steady assessment at maximum and minimum total pressure revealed a higher sensitivity to pressure ratio for turbines with larger diffusion through the vane passage (at minimum total pressure ratio, the efficiency of EW2 decreased by 1.5 percentage-points while this decreased by 8 percentage-points for EW3, due to a reduction of the rotor inlet relative flow angle causing the rotor to work at off-design condition).

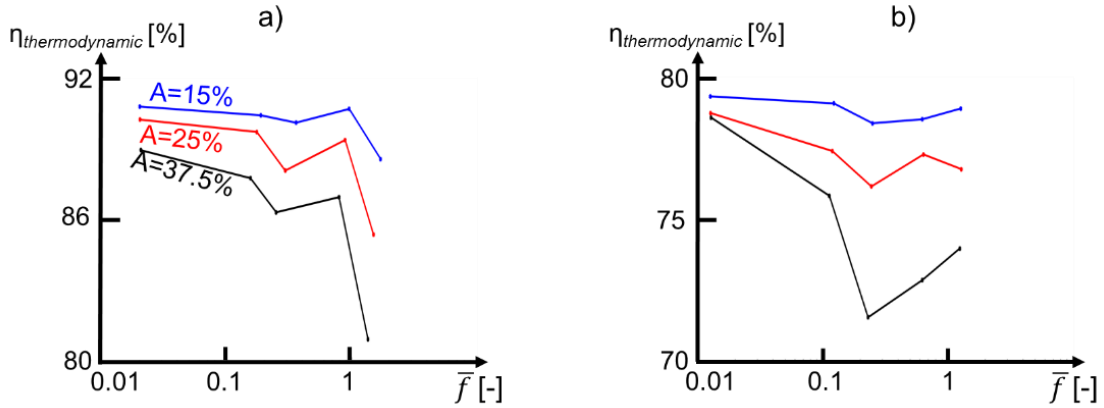


Figure 3.10. Turbine efficiency in function of amplitude and reduced frequency for a) EW2 and b) EW3.

The turbines were designed to not only efficiently cope with high inlet Mach numbers for power extraction, but also to attenuate the large fluctuations induced by the upstream diffuser for the subsequent turbine stages. Stage damping, defined in Equation (3.10), was assessed to quantify the attenuation (positive damping) and enhancement (negative damping) of the total pressure propagating across the turbine internal passage. Figure 3.11 depicts the stage damping of the total pressure oscillations for EW2 (Fig 3.11a) and EW3 (Fig 3.11b). Attenuation of total pressure is found for all reduced frequencies and amplitudes for both configurations. In order to accommodate higher inlet Mach number, higher level of endwall diffusion is required, resulting in an increase of damping and decrease of turbine efficiency. As shown in Fig. 3.11a, for a pulsating amplitude of 15%, the maximum stage damping for EW2 is 83.3% at a reduced frequency of 0.96. However, for EW3, the maximum stage damping reaches 86.9% at a reduced frequency of 0.63.

$$Damping_{p01} = \frac{A_1 - A_3}{A_1} \quad (3.10)$$

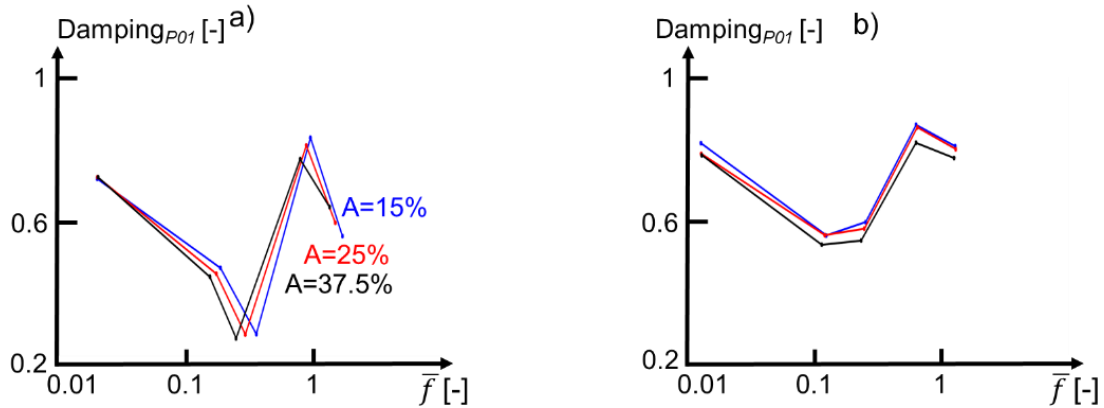


Figure 3.11. Stage damping in function of reduced frequency and amplitude for a) EW2 and b) EW3.

This precise evaluation of efficiency and damping for multiple amplitudes of the flow fluctuations in function of the reduced frequency can be used for accurate assessment of engine performance such as analysis performed by Sousa et al. [26]. To investigate the mechanism behind the effect of the reduced frequency and amplitude on the flow features, Figure 3.12 represents the axial velocity contour, where negative values (in blue) reveal large recirculation bubbles. The recirculation bubbles are created by the interaction of the airfoil secondary flow and the positive pressure gradient in the region of high endwall diffusion. At a low fluctuating amplitude (Fig. 3.12a), the bubble size displays minor variations in the investigated frequency span. However, at a large pulsating amplitude (Fig. 3.12b), the bubble size varies considerably as the reduced frequency increases. As a result, the stator loss rises and the turbine performance is abated.

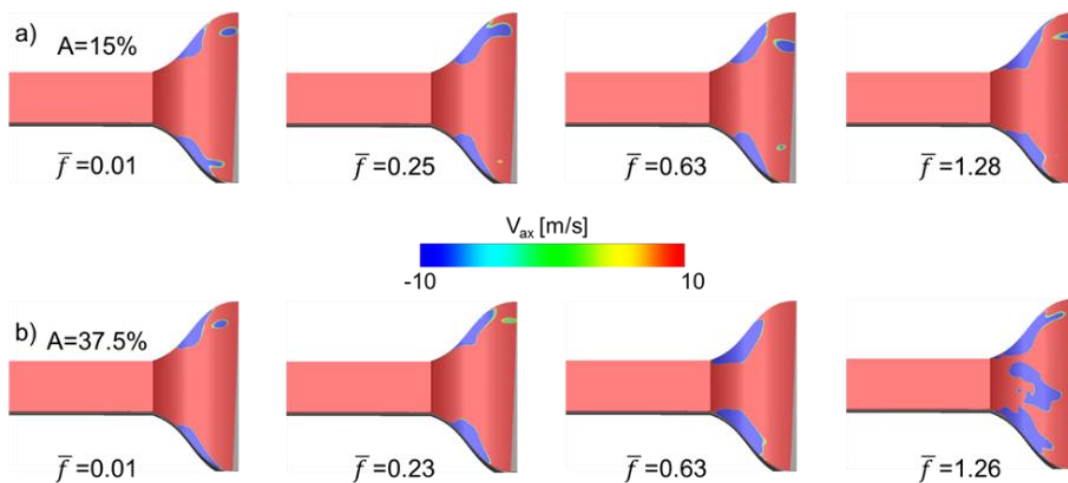


Figure 3.12. Instantaneous stator axial velocity contour of EW3 in function of the reduced frequency at a) $A=15\%$ and b) $A=37.5\%$.

3.3.3 URANS Stage Simulations: Full Unsteady Approach

The full unsteady simulations were performed on a numerical grid of 19 million cells with 2 stator and 3 rotor passages. The computational time was 50% higher than the mixing plane approach in addition to an increase of grid cell by a factor of 2.4. Fluctuations of total pressure were imposed at the inlet of both configurations for a peak-to-mean amplitude of 37.5% at two reduced frequencies: 1.38 and 1.26. Figure 3.13 displays the instantaneous total pressure flow field for EW2. At the stator-rotor interface, the fluctuations from the stator outlet were fully conveyed to the downstream rotor. Therefore, the rotor displays non-uniform rotor inlet total pressure in both radial and tangential direction at each time instant in contrast to the mixing plane approach (Fig. 3.9). Due to the high reduced frequency ($\bar{f} > 1$), the next total pressure pulsation already started at the stator inlet before the previous fluctuation propagated throughout the rotor passage. Table 3.5 summarizes the turbine efficiency from the steady RANS stage simulation, a full unsteady stage with constant inlet, a URANS stage with pulsating inlet and the mixing plane approach, and a full unsteady stage with pulsating inlet. Due to the increased stator-rotor interaction, at constant inlet efficiency decreases by 0.6 percentage-point for EW2 while this penalty increases to 1.4 percentage-points for the largest diffusion case (EW3). When the turbine is submitted to the largest fluctuations ($A=37.5\%$) at high reduced frequency, the URANS stage with mixing plane approach underpredicts the efficiency by 5.3 percentage-points for EW2 and 4.4 percentage-points for EW3.

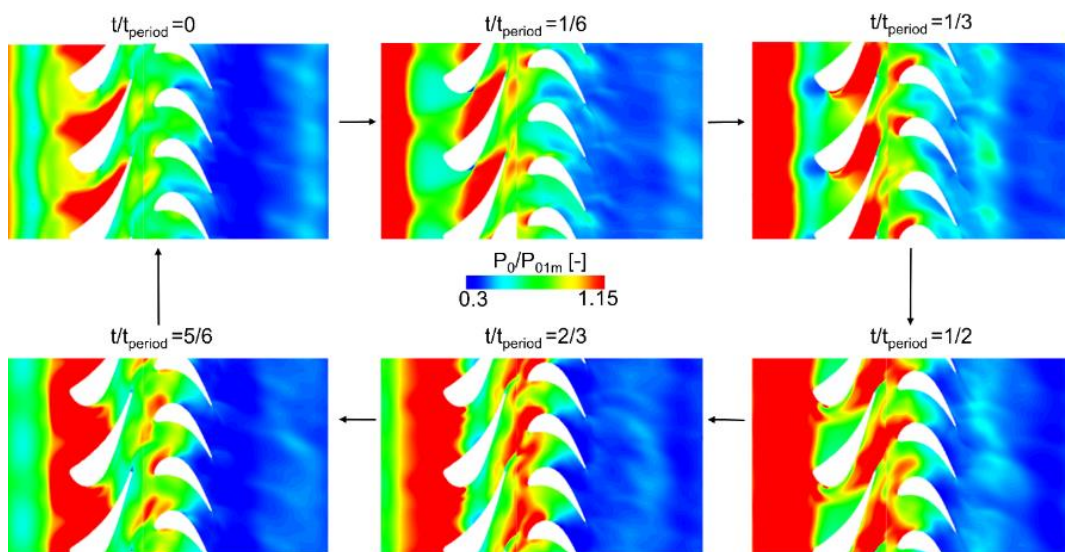


Figure 3.13. Flow field of a full unsteady stage simulation of EW2 exposed to a total pressure fluctuation ($A=37.5\%$, $\bar{f}=1.38$).

Table 3.5: Comparison of turbine efficiency for EW2 and EW3 between steady and full unsteady simulations.

	EW2 (Mach inlet=0.3)				EW3 (Mach inlet=0.6)			
	RANS	Full unsteady (constant inlet)	Mixing plane ($\bar{f}=1.38$, A=37.5 %)	Full unsteady ($\bar{f}=1.38$, A=37.5 %)	RANS	Full unsteady (constant inlet)	Mixing plane ($\bar{f}=1.26$, A=37.5 %)	Full unsteady ($\bar{f}=1.26$, A=37.5 %)
$\eta_{\text{thermodynamic}}$	90.6 %	90.0%	81.0%	75.7%	79.7 %	78.3%	74.0%	69.6%

Furthermore, the validity of the mixing plane model is assessed for EW3 over a range of amplitudes and reduced frequencies in terms of turbine efficiency (Equation 3.8) and stage damping (Equation 3.10). Due to the pitch-wise averaging of the upstream fluctuations at the mixing plane, the turbine efficiency is over-predicted for all cases. The discrepancy is 2.5 percentage-points at a low pulsating amplitude of 15% while this increases to 4.2 percentage-points for large amplitudes. Additionally, the stage damping features an under-estimation of 3.8 percentage-points at a low amplitude and a maximum deviation of 32.8 percentage-points at a large amplitude within the intermediate regime ($0.1 < \bar{f} < 1$), where the speed at which the flow characteristics travel throughout the passage have the same order of magnitude as the induced excitations. In sum, for the turbine design with large diffusion under the pulsating environment, the mixing plane approach is a cost-effective method to assess turbine efficiencies across a wide range of fluctuating amplitudes and reduced frequencies. However, full unsteady simulations are required to accurately evaluate the stage damping to account for precise stator-rotor interactions, particularly at large amplitudes where strong interactions between diffusion and secondary flow occurs.

3.4 Optimization Strategy

The multi-step optimization strategy is outlined in Figure 3.14: The steady optimization (Fig. 3.14a) starts with a turbine parametrization via an in-house code [56]. In this case, seven design parameters were selected for the stator and rotor endwalls. The turbine geometry is meshed and solved. The objective functions (thermodynamic efficiency and specific work) are extracted from the post-processing and are fed to a differential evolution optimizer, CADO [57]. Afterwards, the

three most influential design parameters from the steady optimization are provided for the unsteady optimization (Fig. 3.14b). During the unsteady optimization, URANS equations are solved in which large inlet fluctuations are imposed to the turbine inlet.

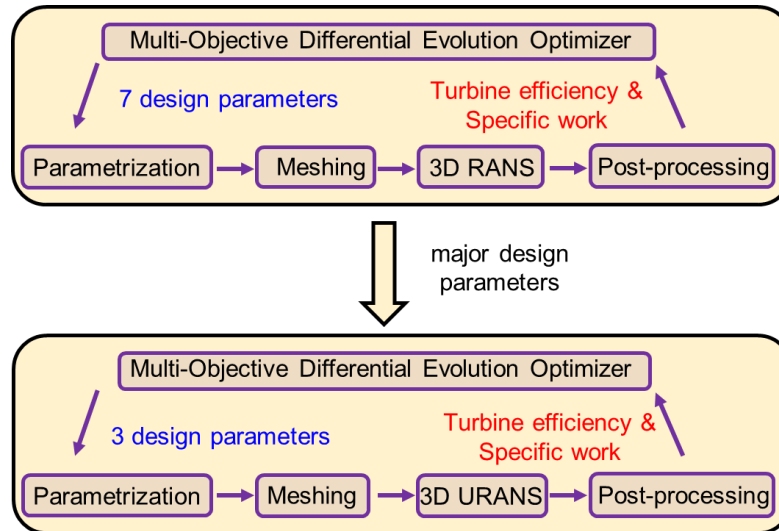


Figure 3.14. Multi-step optimization strategy.

Figure 3.15 illustrates the turbine channel parametrization for the steady optimization. The vanes and rotor blade profiles were unaltered during the optimization and the stage had a degree of reaction of 0.3 [58]. This airfoil design was selected for its adequate performance at on and off-design condition and was validated in various experimental and numerical studies [58][59][60][61] in contrast to impulse blades which trade turbine efficiency for work extraction and perform poorly at off-design conditions. Four free control points (x_1 , x_2 , x_3 , and x_4) defined the contour of the stator endwall and were free to move in the radial direction with a certain degree of variability. Three free control points (x_5 , x_6 , and x_7) were assigned to contour the rotor hub. The fixed points were constrained in both radial and axial direction to allow for a Mach 0.6 flow at the inlet of the turbine. The endwalls were contoured with a Bezier curve to ensure a smooth endwall design and axisymmetry was assumed. The steady optimization was initialized with a Design of Experiments (DoE) through a fractional factorial method [62] to generate 128 individuals. The individuals per population of the multi-objective optimizer, equipped with the NSGA-II algorithm [63], were set to 40.

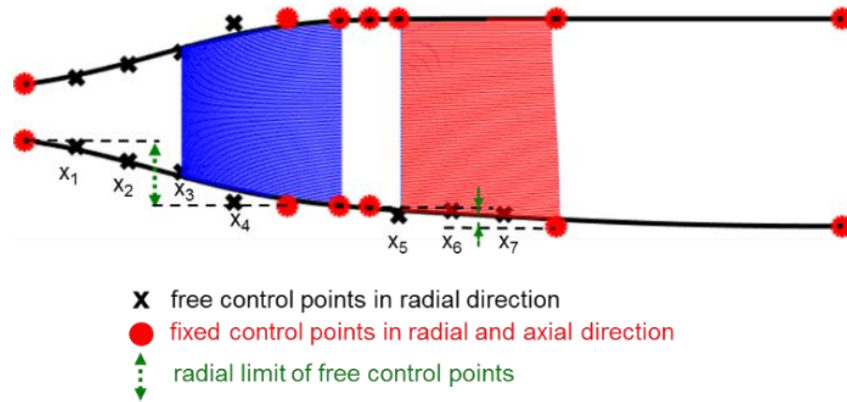


Figure 3.15. Turbine channel endwall parametrization for the steady optimization.

3.5 Results

3.5.1 Steady Optimization

The computational burden for one individual was around 10 hours on one Intel Xeon-E5 node. During the steady optimization, six populations were generated with a total of 368 geometries. Figure 3.16 depicts the Pareto front of these individuals together with the DoE and the baseline. All individuals are colored by the stator inlet Mach number. Turbine efficiency was computed by Equation (3.8) and specific work are evaluated via Equation (3.11). The Pareto front is defined as a region in which the efficiency of the endwall profiles cannot be improved without penalizing the specific work and vice versa. In this case, the Pareto front is situated in the upper right area. These profiles also featured high inlet Mach number (up to 0.65). Optimized endwall geometries have up to 12.5% of efficiency increase compared to the baseline and the specific work was enhanced by more than 13%. In addition, the position of the control points from the superior endwall designs suggest that the free control point x_1 of the stator endwalls (Fig. 3.15) should be radially close to the first fixed control point and the rotor hub endwall control points (points x_5 , x_6 , and x_7 in Fig. 3.15) have a minor effect on the turbine performance. Hence, three major design parameters (x_2 , x_3 , and x_4) are selected for the unsteady optimization.

$$w = C_p(T_{01} - T_{03}) \quad (3.11)$$

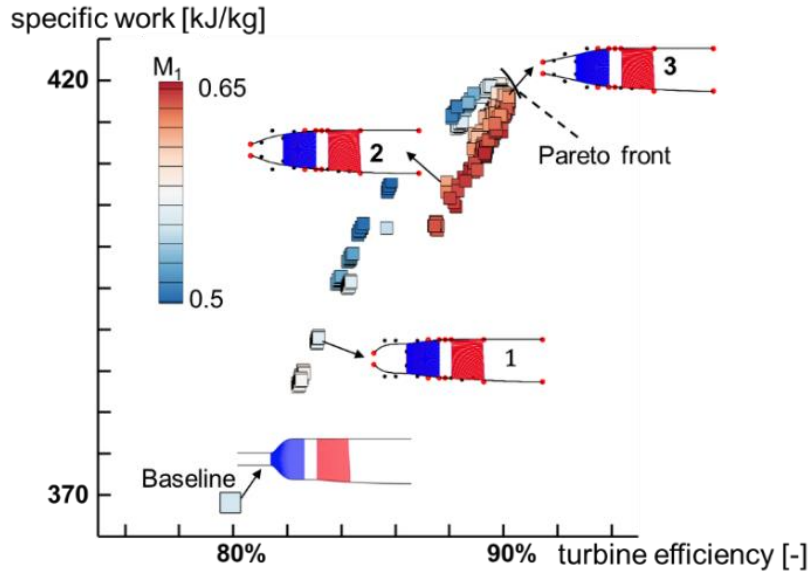


Figure 3.16. Pareto front of the steady optimization.

Separation due to endwall diffusion causes total pressure loss and negatively impacts the efficiency and work potential of the turbine stage. This effect is amplified for increased diffusion across the stator from the baseline study. Therefore, the amount of separation at a cross-section plane within the stator passage was assessed and is defined in Equation (3.12) as the amount of area that contained separated flow. Separated flow area was defined as mesh cells in which the axial velocity is less than 0.01 m/s.

$$\text{Separation intensity} = \frac{SS_{(v_{ax} < 0.01)}}{SS} \quad (3.12)$$

Figure 3.17a describes a pitch-wise cut within the baseline stator passage contoured by the axial velocity. A significant separation occurs for the baseline stator with a separation intensity of 19.5% while the steady-optimized configuration shows the separation intensity of only 0.2%. Figure 3.17b displays the Pareto front colored by the separation intensity. The upper right zone, featured by profiles with high efficiency and specific work, are also characterized by a low separation intensity.

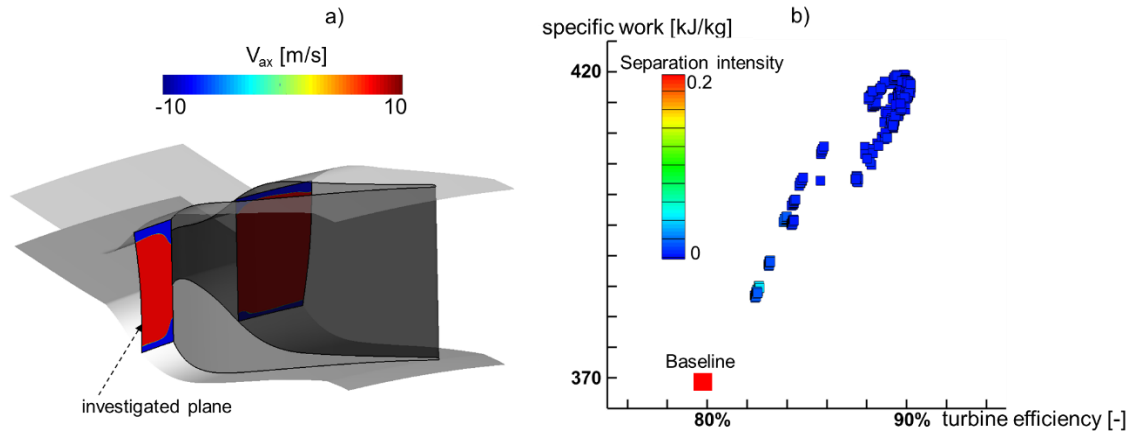


Figure 3.17. a) Axial velocity contour of the baseline stator. b) Pareto front colored by the separation intensity.

3.5.2 Unsteady Optimization

Seven populations were created containing 37 endwall geometries. The computational burden was 48 hours per individual on one Intel Xeon-E5 node. The Pareto front of 37 individuals, the DoE, and the baseline are illustrated in Fig.3.18a. To evaluate the objective functions for the unsteady cases, all parameters of Equation (3.8) were first instantaneously mass-flow-averaged and afterwards cycle-mass-averaged over a periodic cycle to determine the thermodynamic efficiency. The Pareto front is again visible in the upper right area. The individuals are colored by the amount of damping which quantifies the residual fluctuations at the outlet of the first turbine stage and was assessed with Equation (3.10).

Compared to the baseline profile, the turbine efficiency increased by approximately 21.4% for the optimized endwall geometries. The specific work from the optimized configurations was augmented by more than 22%. From the baseline to the optimized profiles, damping of the total pressure fluctuations increased by up to 30 percentage-points. Figure 3.18b plots the total pressure signature extracted from the stator inlet and rotor outlet for both baseline and unsteady-optimized turbine (profile 2, Fig. 3.18a) for two pulsating periods, where the stage damping across profile 2 was 83% and was 29 percentage-points higher than the baseline case.

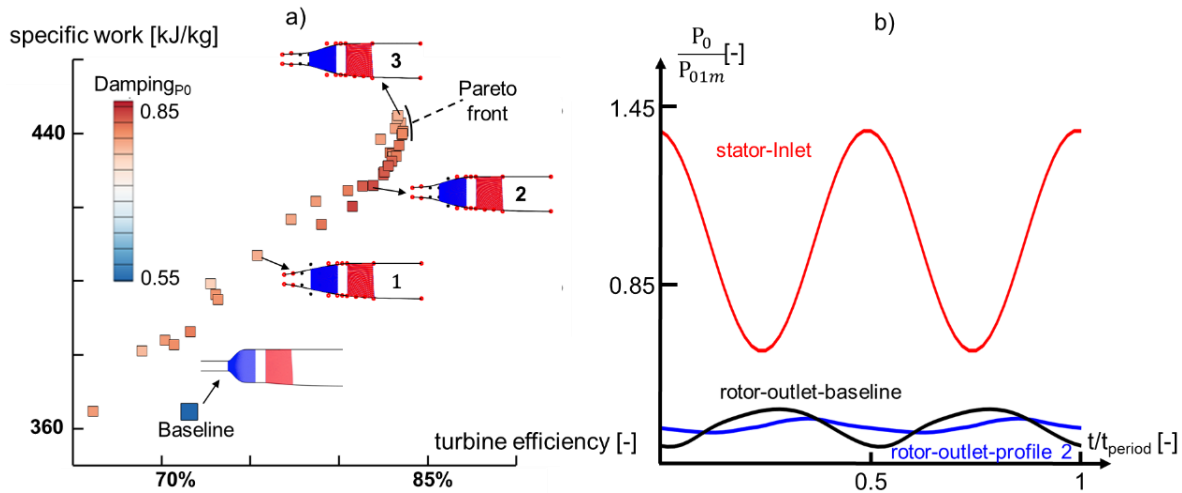


Figure 3.18. a) Pareto front colored by stage damping. b) Total pressure traces from the stator inlet and rotor outlet.

For the baseline profile, the endwall opening occurs only across the stator passage. As a result, flow experiences diffusion at the beginning then is accelerated till the stator trailing edge. However, for both the steady and unsteady optimized profiles, flow is diffused upstream of the stator in such a way that flow turning is enhanced and full acceleration is achieved in the stator passage. Figures 3.19a-c display the channel for the baseline, the steady-optimized (profile 3, Fig. 3.16), and unsteady-optimized (profile 2, Fig. 3.18a) stator, and the stator throat-to-local area ratio for each case is plotted in Fig. 3.19d. In the baseline stator, local cross-section area keeps increasing from the leading edge till the mid-axial chord during which diffusion is dominant and flow separation occurs whereas the channel keeps converging in both optimized configurations from the stator leading edge till the trailing edge. In addition, at steady state, the Mach number in front of the stator leading edge is 0.64 for the baseline, 0.3 for the steady-optimized, and 0.35 for the unsteady-optimized profile. This indicates that unsteady-optimized endwall is diffused to a lesser extent upstream of the stator leading edge, which helps to suppress the growth of the unsteady recirculation bubbles for the pulsating inlet condition compared to the steady-optimized endwall. As shown in Figure 3.20 where the negative axial velocity represents recirculation bubbles, the bubble size is considerably reduced in the unsteady-optimized stator (profile 2, Fig. 3.18) compared to the one in the steady-optimized stator (profile 3, Fig. 3.16).

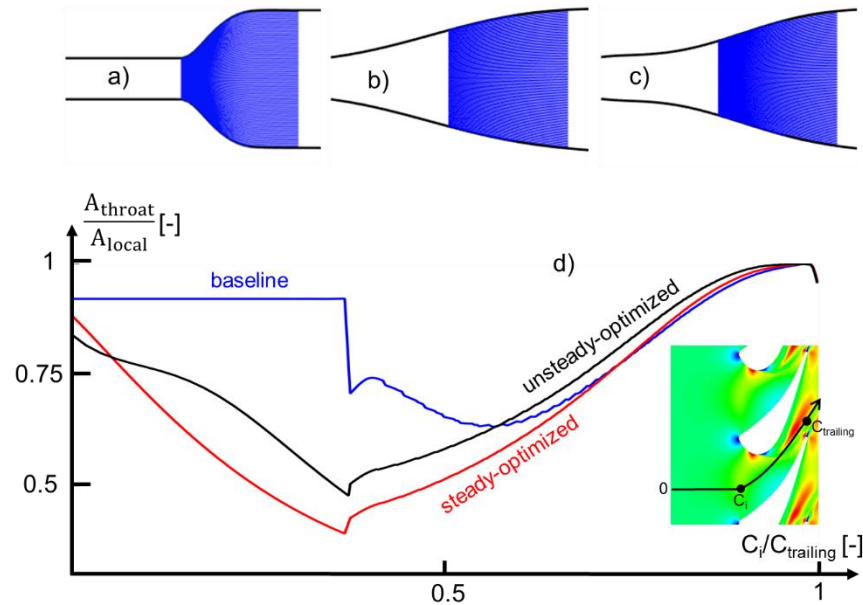


Figure 3.19. Meridional view of a) baseline stator, b) profile 3 in Fig. 3.16, and c) profile 2 in Fig. 3.18a. d) Throat-to-local area ratio in function of the normalized surface curvilinear coordinate.

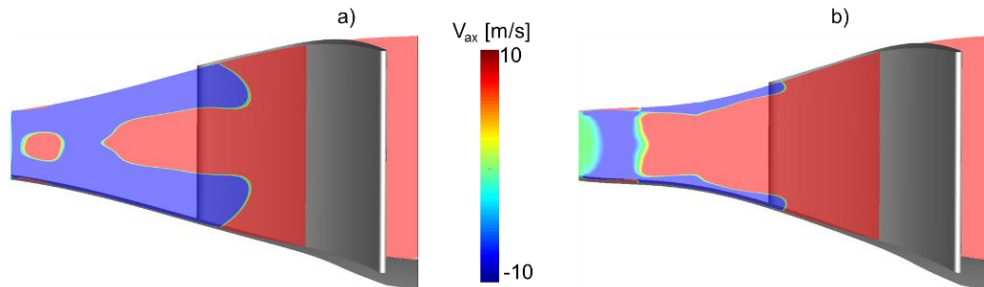


Figure 3.20. Instantaneous axial velocity contour at $\bar{f}=0.23$ and $A=37.5\%$ of a) profile 3 in Fig. 3.16 and b) profile 2 in Fig. 3.18a.

3.5.3 Full Unsteady Assessment of Optimized Endwall Geometries

High-fidelity full unsteady simulations of the turbine stage were carried out with inlet total quantities pulsations at a reduced frequency of 0.23 for two peak-to-mean amplitudes, where at the stator and rotor interface upstream fluctuations were fully conveyed to the downstream rotor compared to the mixing plane approach. The entire computational domain contains two stator passages and three rotor passages. Consequently, the computational burden increased to 168 hours on three Intel Xeon-E5 nodes compared to 48 hours for the mixing plane approach with only one

node. Profile 3 from Fig. 3.16 was selected for the steady-optimized profile while profile 2 from Fig 3.18a was chosen for the unsteady-optimized profile. Figure 3.21a depicts the mid-span relative Mach contour of the steady-optimized turbine (profile 3, Fig. 3.16) during one period of the inlet fluctuations and turbine efficiencies are plotted in Fig. 3.21b. The steady-optimized turbine (profile 3, Fig. 3.16) outperforms the baseline (by 10 percentage-points) and unsteady-optimized turbine (by 0.4 percentage-point) when operating at steady state. However, under pulsating conditions, the full unsteady assessment demonstrates that the unsteady-optimized turbine (profile 2, Fig 3.18a) outperforms the baseline and steady-optimized turbine (profile 3, Fig. 3.16) by up to 13 percentage-points. The deviation in turbine efficiency between the full unsteady analysis and the mixing plane approach was 4.4 percentage-points, which demonstrates the validity of using the mixing plane approach for unsteady optimization.

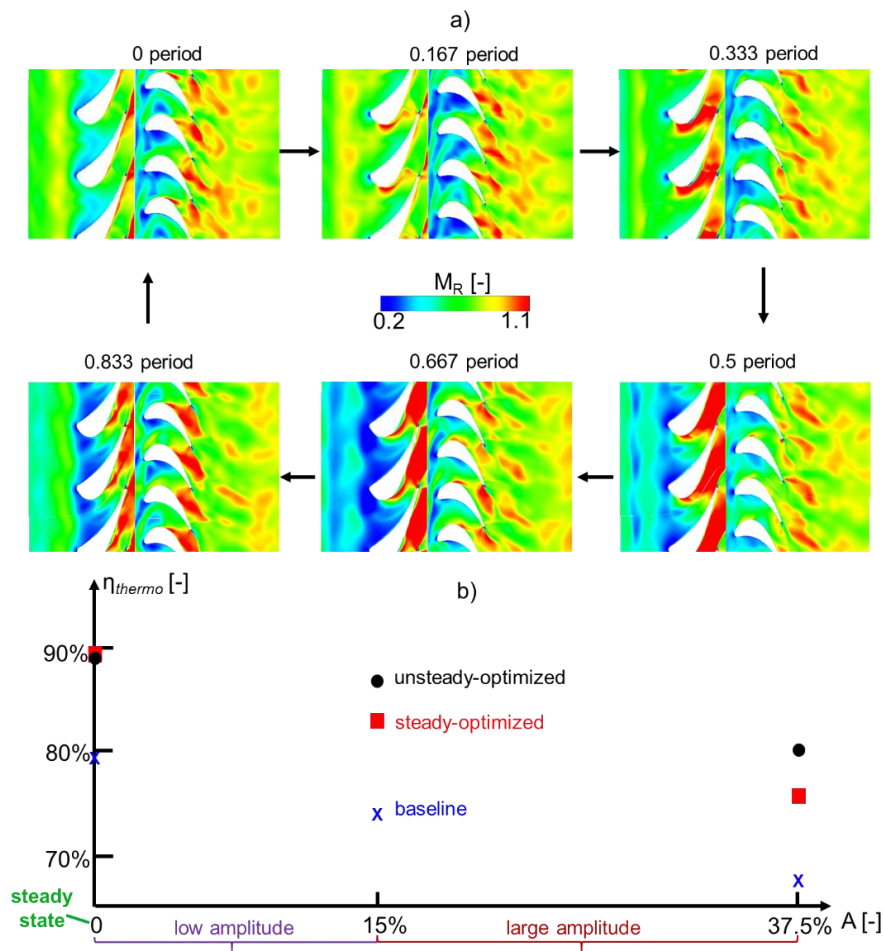


Figure 3.21. a) Flow field from a full unsteady turbine simulation (profile 3, Fig. 7) at $A=37.5\%$ and $\bar{f}=0.23$. b) Turbine efficiencies of the baseline and selected optimized configurations.

3.5.4 Engine Model with a Rotating Detonation Combustor and an Optimized Turbine Profile

To assess the benefits in terms of power extraction and thermal efficiency of rotating detonation engines with the retrofitted turbine, an engine model with T-MATS [64] similar to Sousa et al. [26] was developed for a turbojet engine configuration. T-MATS is a NASA developed open source toolkit to model thermodynamic systems such as engines and turbomachinery components. Figure 3.22a shows the different components that were implemented for this power plant. The inlet is followed by a conventional compressor. The burner is the rotating detonation combustor and fuel-to-air ratio and pressure gain are required as input. Figure 3.22b depicts the pressure gain of a RDC that was retrieved for each overall compression ratio, calculated via the reduced order model and verified with 2D URANS calculations [14] and implemented within the T-MATS environment.

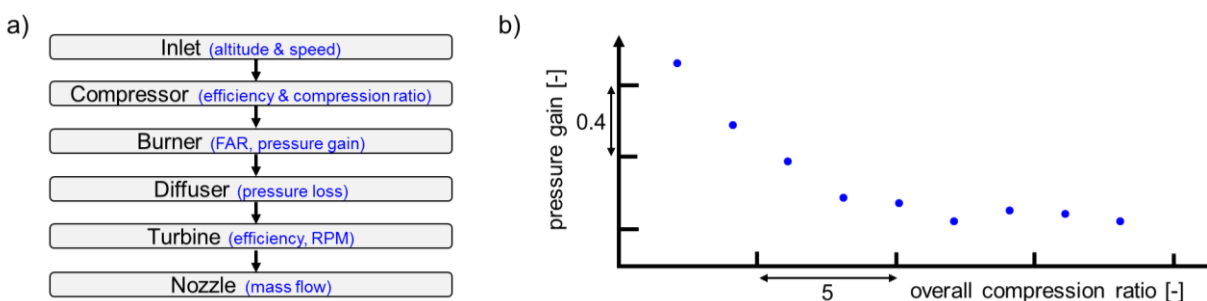


Figure 3.22. a) Engine model. b) Pressure gain in function of the overall compression ratio of the engine.

Figure 3.23a details the engine thermal efficiency (Equation 3.13) in function of the overall compression ratio for several engine layouts with an assumed pressure loss through the diffuser of 30%. The rotating detonation engine layout has a turbine with an efficiency of 86.3% (based on profile 2 in Fig. 3.18a with 25% mean-to-max amplitude) and an efficiency of 76% (based on the baseline design with 25% mean-to-max amplitude). For low pressure ratios, the pressure gain was the major reason of thermal efficiency increase for an RDC cycle as most of the thrust comes from the high-pressure gain. At low compression ratios, benefits are as high as 10 percentage-points. At intermediate compression ratios, the turbine efficiency becomes increasingly important to maintain gains compared to deflagration. The reason behind this is that at low pressure ratios, the power extraction from the turbine is low compared to the thrust from the pressure gain while at higher compression ratios the pressure gain is lower. From intermediate to high compression ratios,

the optimized turbine yields in a thermal efficiency gain up to 2 percentage-points compared to the baseline turbine. In addition, as the compression ratio increases, a detonation-based engine coupled with the baseline turbine is inferior to conventional deflagration engines in terms of thermal efficiency. Hence, the appropriate selection of the stator endwall contour is especially critical in these high compression ratio regions. Figure 3.23b depicts the non-dimensional thrust for several compression ratios in which the highest gain is observed at low and intermediate compression ratios.

$$\text{Engine thermal efficiency} = \frac{(\dot{m}_0 + \dot{m}_5)V_5^2 - \dot{m}_0V_0^2}{2\dot{m}_f Q_l} \quad (3.13)$$

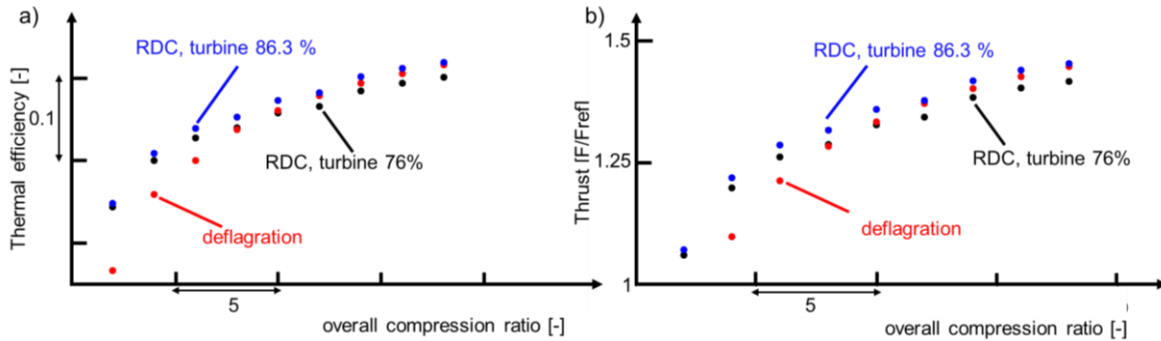


Figure 3.23. Thermal efficiency (a) and thrust (b) in function of pressure ratio.

3.6 Performance Map

Forty-nine RANS cases of the selected optimized turbine were carried out to explore the turbine operating range at off-design condition. For a certain RPM, the total-to-static pressure ratio (P_{01}/P_3) ranges from 1.4 to 3.8. For a certain total-to-static pressure ratio, RPM varies from 60% to 120% nominal condition.

Figure 3.24a plots the total-to-total pressure ratio across the stage at different corrected mass flow. For each RPM, once the pressure ratio exceeds 1.5, the stator throat is choked, with inlet mass flow unchanged. Figure 3.24b depicts the turbine efficiency in function of the product of corrected mass flow (Equation 2.15) and corrected speed (Equation 2.16). Below the nominal RPM, flow is separated on the rotor suction side and the separation is intensified as RPM keeps

decreasing due to the strong positive incidence, resulting in low efficiencies. For all investigated RPM, increasing total-to-static pressure ratio feeds more mass flow into the turbine and generates more torque. However, once the turbine is choked, the efficiencies are maintained around a certain level which is 88% for nominal RPM and decreases to 81% for 70% RPM.

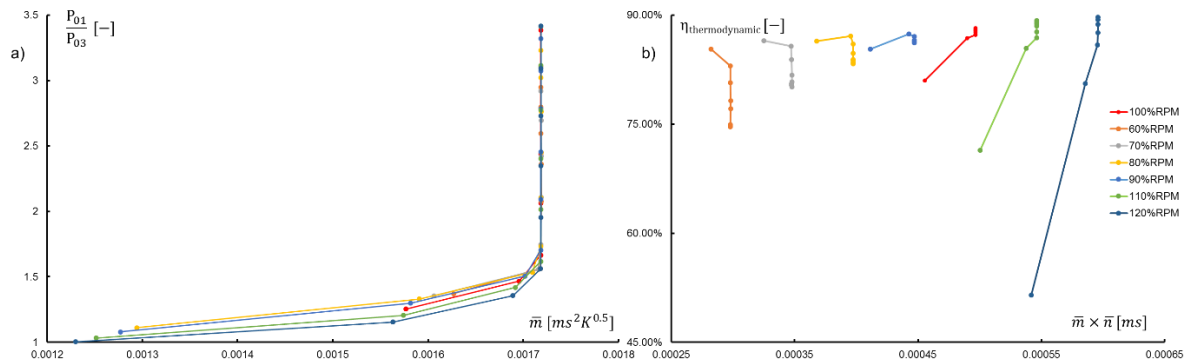


Figure 3.24. a) Total-to-total pressure ratio in function of the corrected mass flow. b) Turbine efficiency in function of the product of corrected mass flow and corrected speed.

3.7 Design of Experiments

3.7.1 Facility Introduction and Test Article Design

An experimental campaign is designed to replicate the diffusion from the stator inlet to the stator leading edge of the selected optimized endwall geometry (profile 2, Fig. 3.18a) in the PETAL linear test section (Fig. 3.25). The test section is equipped with Quartz side walls to allow for fully optical measurements [65]. A sonic valve is placed downstream of the test section to allow for tests with various Mach numbers, by varying the throat area [65]. A wide span of Re could be achieved by fixing the upstream conditions as well as the back pressure [65].

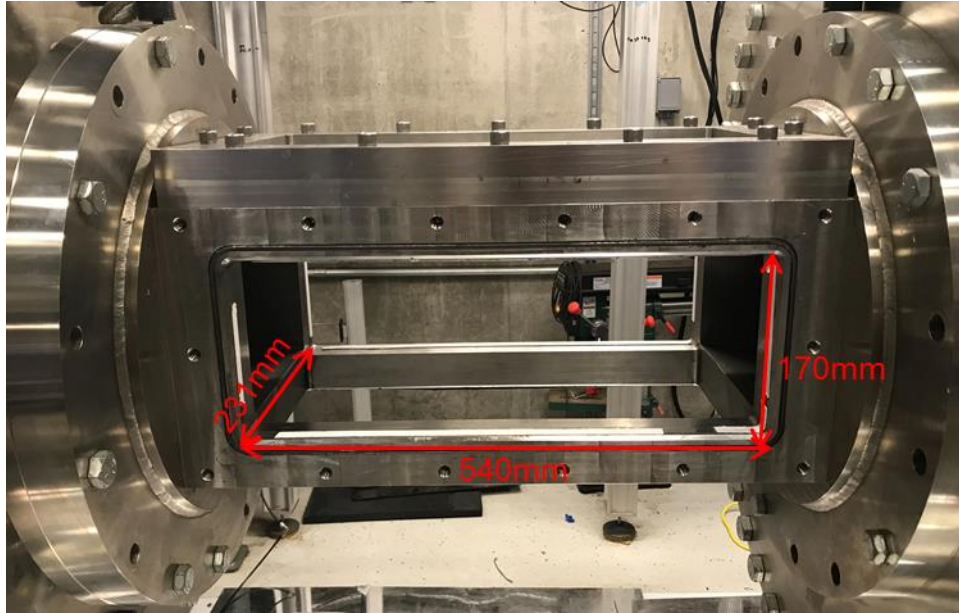


Figure 3.25. PETAL facility linear test section.

The test article shown in Fig. 3.26a consists of three components to increase modularity of the test section: a converging nozzle (colored by orange), a diffuser (replicating the optimized endwall curvature from inlet to the stator leading edge, colored by red), and a flat plate (colored by green). All components are designed with Bezier curves to ensure a smooth curvature. The test article is placed on a bottom support (colored by blue), with pressure tappings displayed in Fig. 3.26b. The diameter of the pressure tappings is 1.6mm. A 2D RANS simulation of the entire test section was conducted. The throat height of sonic valve was carefully selected so that the turbine inlet Re was replicated at the diffuser inlet while the throat of sonic valve was choked, at an upstream total temperature of 300K. The inlet mass flow is around 3.52 kg/s. A representation of the test article assembly in the linear wind tunnel is detailed in Fig. 3.27a. Flow field of the test section is illustrated in Fig. 3.27b. The downstream wedge simulates the operation of the sonic valve, where the summation of the outlet length represents the sonic throat height. In this case, the outlet is choked. Close to the end of the diffuser, a minor separation is observed (Fig. 3.27c). Figure 3.28 depicts the static pressure distribution along the test article. Flow enters the test section at around Mach 0.1, is accelerated to around Mach 0.53 at the diffuser inlet, and is then decelerated all the way to the exit of the flat plate.

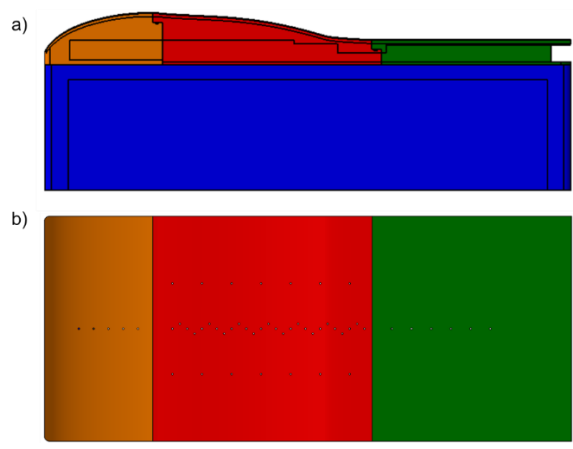


Figure 3.26. a) Frontal view of the test article. b) Top view of the pressure tapings.

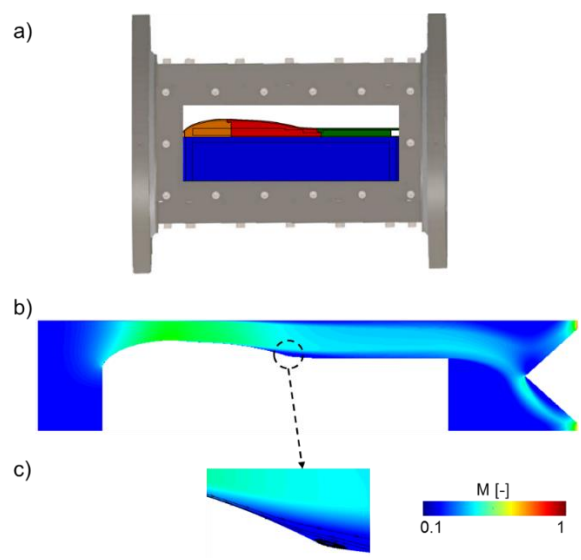


Figure 3.27. a) Test article assembled in the linear test section. b) Flow field of the test section. c) Diffuser end: snapshot of flow separation.

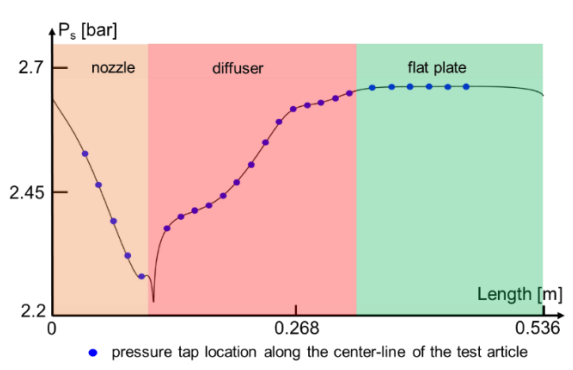


Figure 3.28 Static pressure distribution along the test section

3.7.2 Proposed Measurement Techniques

3.7.2.1 Low-Frequency Measurements

Steady pressure measurements are achieved via a Scanivalve data acquisition system through pneumatic lines. Due to the length of the tubes, the pressure fluctuations are considerably attenuated, resulting in a low frequency response. A Pitot probe is used to measure the flow total pressure. Steady heat flux is retrieved by surface thermocouples combined with a one-dimensional solver [66]. Flow total temperature is measured by total temperature thermocouples. Skin friction is measured by oil-film interferometry (OFI) technique proposed by Naughton and Braun [67], which correlates the oil droplet deformation to shear stress. Through Quartz windows, the flow structure can be visualized with Shadowgraph imaging.

3.7.2.2 High-Frequency Measurements

Unsteady surface pressure measurements are performed via fast-response Kulites sensors (XCE-062, up to 120 kHz). To maintain high-frequency content, the dimension of pneumatic lines (length and diameter) must be carefully selected based on the theory of Bergh and Tijdeman [68]. A dynamic calibration of this type of sensor was performed by Paniagua and Denos [27]. For high-frequency heat flux measurements, an atomic layer thermopile is used [69]. The velocity vectors of the flow field are resolved via Particle Image Velocimetry (PIV), and femtosecond laser electronic excitation tagging [70] and the density field is resolved via Background Oriented Schlieren.

4. DEVELOPMENT OF FLOW MEASUREMENT TOOLS FOR EXPANSION SYSTEMS

In this chapter, a fast-response directional probe for high-frequency pressure measurement is designed through a detailed numerical procedure. Afterwards, angular calibration is performed. In the end, a biomimicry-inspired design is explored.

4.1 Directional Probes for Pressure Measurements in Subsonic Flow

4.1.1 Probe Shape and Computational Domain

Figure 4.1 shows the two investigated probe geometries, both with identical overall dimensions, i.e. 4.4×2.2 mm. The computational domain is 100×100 mm, covering more than 20 times the probe dimension upstream and downstream. The grid was unstructured which totaled around 250,000 cells. The probe curvilinear coordinate “S” shown in Fig. 4.1 is defined around the probe perimeter.

To quantify the angle sensitivity, the pressure coefficient is defined in Equation (4.1) as the difference between local static pressure at the location “j” of the probe curvilinear coordinate and the upstream flow static pressure, non-dimensionalized by the dynamic pressure:

$$C_{pj} = \frac{P_{Sj} - P_{Sin}}{P_{0in} - P_{Sin}} \quad (4.1)$$

In Equation (4.1), P_{01} and P_{S1} are the upstream flow total and static pressures, located at the far inlet of the computational domain. C_{pj} was evaluated at 5 equiangular locations of the probe curvilinear coordinate shown in Fig.1: “a”, “b”, “c”, “d”, “e”. Angle sensitivity expressed in Equation (4.2) was evaluated at point “a”, “c” and each point was compared with itself between different yaw and 0 yaw. Analyses of unsteadiness sensitivity were performed at the same equiangular locations. Both time-averaged and time-resolved assessment were performed at several Mach numbers, but here we report the results at Mach 0.3, 0.6 and 0.75. Calorically perfect gas (air) was selected as working fluid.

$$abs(C_{pj}) = abs(C_{pj}(yaw) - C_{pj}(0\ yaw)) \quad (4.2)$$

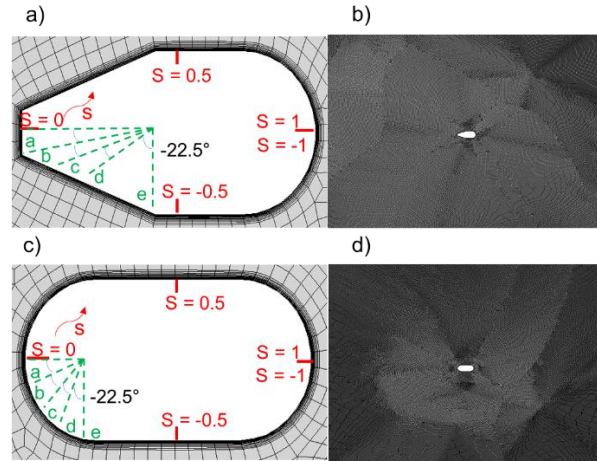


Figure 4.1. a) Trapezoidal probe, and b) the computational domain of the trapezoidal probe. c) Oval probe, and d) the computational domain of the oval probe.

4.1.2 Grid Sensitivity

A grid sensitivity study was completed on the selected probe geometry using the method of Celik [41]. Four grid levels were evaluated with increasing cells numbers: around 70,000 (coarser grid), 129,000 (coarse grid), 250,000 (medium grid), and 440,000 (fine grid). Figure 4.2 depicts the local static pressure non-dimensionalized by the inlet static pressure, measured at the location ‘c’ (Fig. 4.1c) as a function of cell number. The static pressure displays a decreasing trend as cell amount increases, however the relative variation from the medium to the fine grid is minimal. The evaluated grid convergence index (GCI) of medium mesh is 0.27%, indicating a good grid convergence. Hence, the medium mesh was selected for the numerical investigation.

Considering the medium grid, the local static pressure non-dimensionalized by the inlet static pressure, sampled at the location ‘c’ (Fig. 4.1c), was re-evaluated considering different turbulence closures. The three turbulence models were: Spalart-Allamaras (S-A), Standard k-epsilon (k- ϵ), and K-omega SST (k- ω SST). The results are displayed in Fig. 4.3. The discrepancy of local static pressure is about 300 Pa (less than 0.2%) among the different turbulence models. Therefore, the

turbulence closure was provided with the $k-\omega$ SST model, which is also well suited for adverse pressure gradients and separated flows.

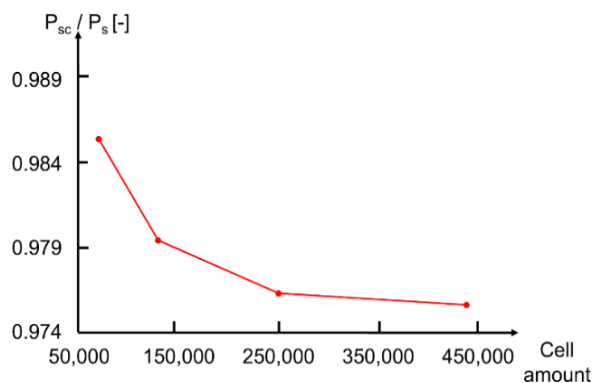


Figure 4.2. Non-dimensional pressure at point ‘c’ on the oval probe in function of grid cell amount.

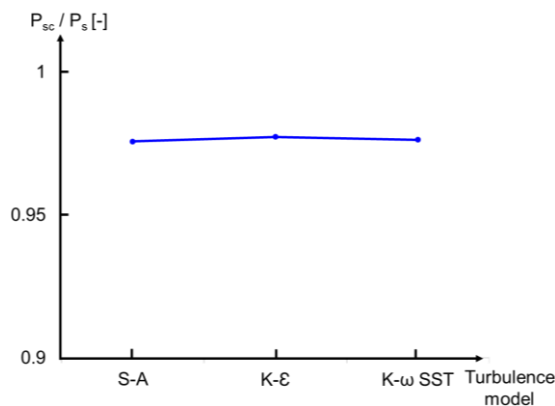


Figure 4.3. Non-dimensional pressure at point ‘c’ on the oval probe in function of the turbulence model.

4.1.3 Unsteady Convergence Assessment

The flow field around the probe is intrinsically unsteady, primarily due to the instantaneous vortex shedding. Hence, the flow field properties are affected by vortex shedding unsteadiness and periodically oscillate. We selected location ‘a’ in Fig. 4.1a to assess the convergence. To assess unsteady convergence, the method of Clark and Grover [42] described in Chapter 2 was carried out, by generating a series of fuzzy sets. Figure 4.4a shows the pressure signal retrieved from location ‘a’ the trapezoidal probe leading edge. Figure 4.4b displays a zoomed view of the previous

trace, comprising seven consecutive periods. In Fig. 4.4c, the three last periods agree very well with each other. The overall membership grade is 0.9952, indicating the achievement of unsteady convergence. For the unsteady subsonic calculations, we selected a time step of $1\mu\text{s}$, whereas for the transonic regime the time step is $0.1\mu\text{s}$. The observation window in all frequency analysis was 2ms to ensure 0.5 kHz frequency resolution. The total computational time for all 2D URANS simulations was about 1344 hours on an Intel(R) Xeon(R) CPU 2.40 Ghz machine.

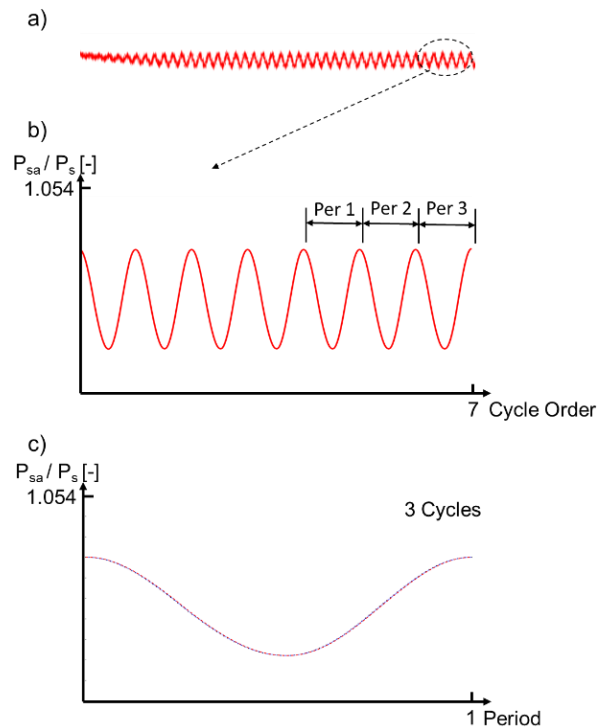


Figure 4.4. a) Non-dimensional pressure retrieved by point ‘a’ on the trapezoidal probe in function of periodic cycles. b) Zoomed portion of the last 7 periodic cycles. c) Overlap of the last 3 cycles.

4.2 Probe Shape Characterization

In the time-averaged pressure measurements, probe shape was characterized in terms of angle sensitivity and total pressure recovery. Twenty four 2D RANS simulations were carried out. Figure 4.4 displays the steady Mach contours for an inlet Mach number of 0.3 at three yaw angles: trapezoidal (Fig. 4.5a) and oval (Fig. 4.5b). As yaw increases toward the negative direction, Mach contour displays non-symmetric characteristics, with a shift of the stagnation point at the probe

leading edge. Figure 4.6 depicts local static pressure non-dimensionalized by the upstream flow static pressure along the probe curvilinear coordinate “S”. The total pressure was recovered close to point ‘a’ and the stagnation point shifts towards the flow impingement location. Figures 4.7a and 4.7b depict contours of C_{Pi} evaluated at “a”, “b”, “c”, “d”, and “e” exposed to several yaw angles. Figures 4.7c and 4.7d evidence that the angle sensitivity of point ‘c’ increases with higher yaw angles for both characterized probe shapes and the trapezoidal probe exhibits a higher angle sensitivity, with a maximum of 10 percentage-points higher at -20° yaw.

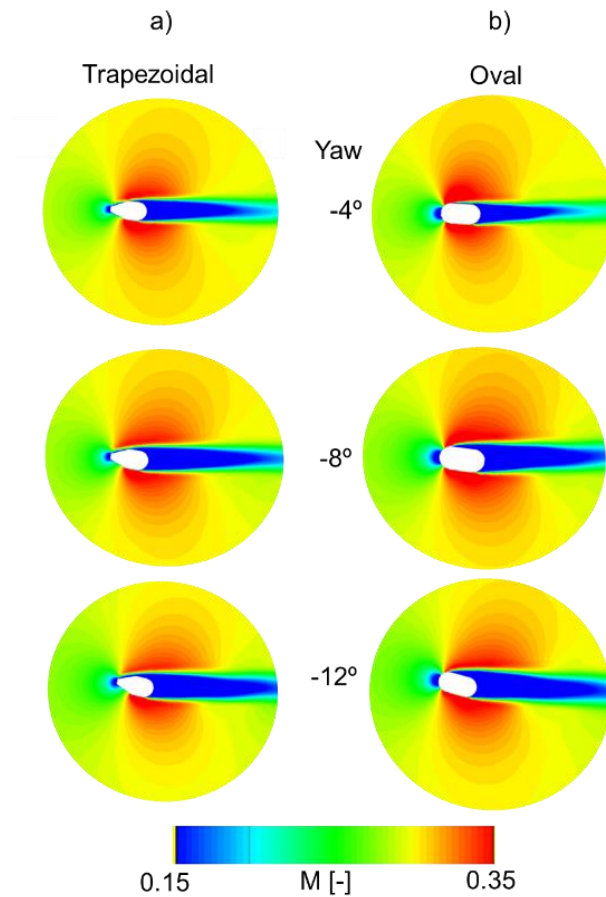


Figure 4.5. Steady Mach contours in function of yaw angles for an inlet Mach number of 0.3 and two characterized probe shapes: a) trapezoidal, and b) oval.

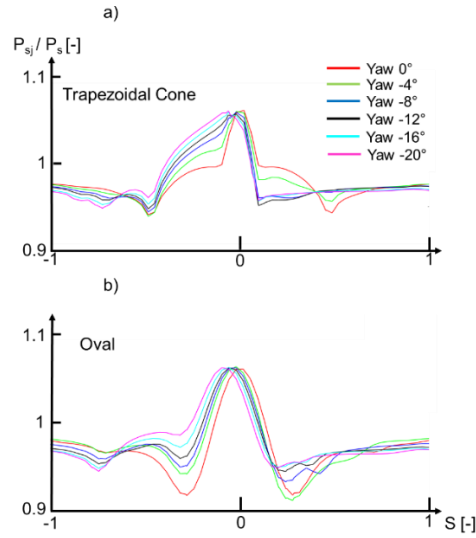


Figure 4.6. Non-dimensional pressure as functions of the probe curvilinear coordinate and yaw angles for an inlet Mach number of 0.3 and two characterized probe shapes: a) trapezoidal, and b) oval.

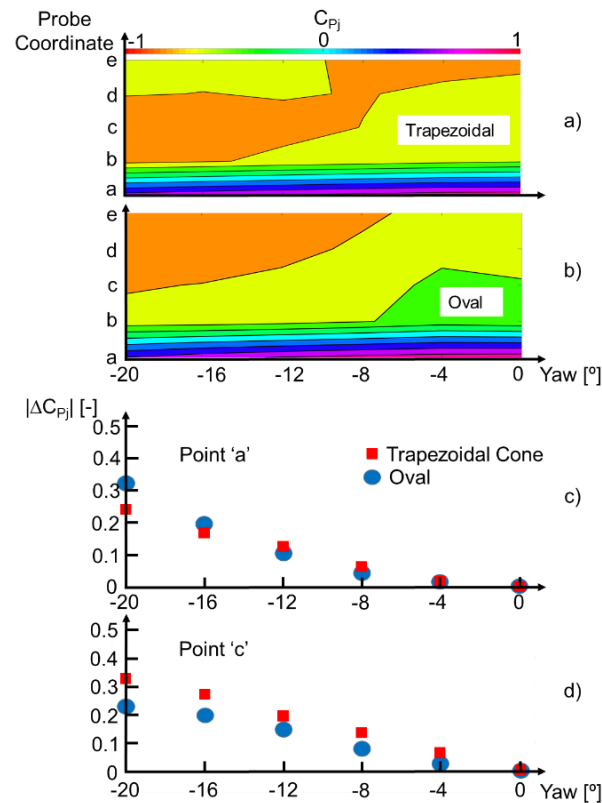


Figure 4.7. Iso-contours of C_{p_i} in functions of yaw angles and probe coordinate for an inlet Mach number of 0.3 and two characterized probe shapes: a) trapezoidal, and b) oval. Angle sensitivity as a function of yaw angles for an inlet Mach number of 0.3 and two characterized probe shapes evaluated at c) point 'a', and d) point 'c'.

In the transonic regime, the steady Mach contours in function of yaw angles for an inlet Mach number of 0.75 is displayed in Fig. 4.8. The supersonic pocket is visualized, encompassing the wake. Figure 4.9 gives the non-dimensional static pressure evaluated along the probe coordinate at an inlet Mach number of 0.75. Similar to Fig. 4.6, the total pressure was recovered close to the stagnation point. However, across the bow shock, a significant total pressure loss is induced. Contours of C_{P_i} evaluated at “a”, “b”, “c”, “d”, and “e” exposed to several yaw angles for an inlet Mach number of 0.75 are depicted in Fig. 4.10a and Fig. 4.10b. The angle sensitivity of point ‘c’ shown in Fig. 4.10c and Fig. 4.10d elevates as yaw angle rises for both characterized probe shapes and the trapezoidal probe evidences a higher angle sensitivity, with a maximum of 15 percentage-points higher at -20° yaw. However, compared with subsonic results detailed in Fig. 4.7, the angle sensitivity is reduced closed to the transonic regime.

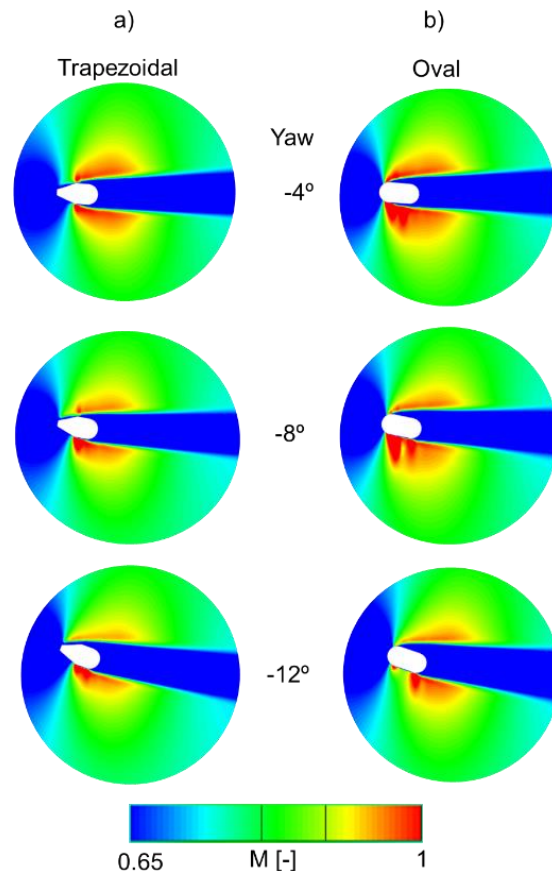


Figure 4.8. Steady Mach contours in function of yaw angles for an inlet Mach number of 0.75 and two characterized probe shapes: a) trapezoidal, and b) oval.

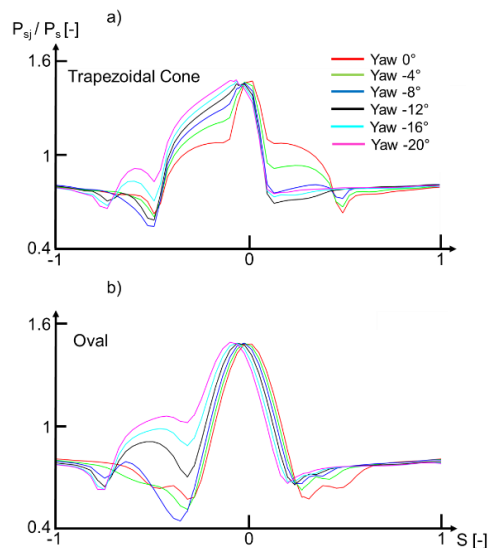


Figure 4.9. Non-dimensional pressure as functions of the probe curvilinear coordinate and yaw angles for an inlet Mach number of 0.75 and two characterized probe shapes: a) trapezoidal, and b) oval.

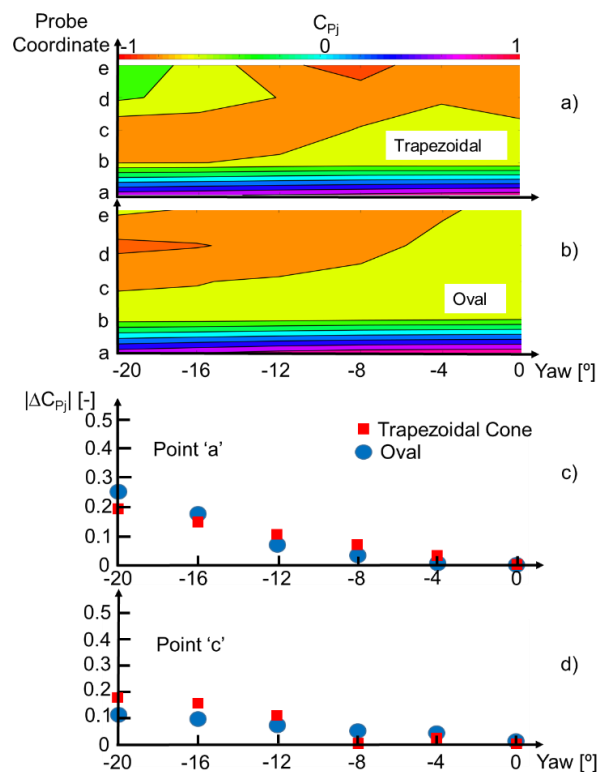


Figure 4.10. Iso-contours of C_{pi} in functions of yaw angles and probe coordinate for an inlet Mach number of 0.75 and two characterized probe shapes: a) trapezoidal, and b) oval. Angle sensitivity as a function of yaw angles for an inlet Mach number of 0.75 and two characterized probe shapes evaluated at c) point 'a', and d) point 'c'.

Total pressure recovery is defined as C_{pa} by reevaluating C_{pj} at the point “a” with 0 yaw angle for both characterized shapes and two inlet Mach numbers: 0.3 and 0.75. Comparison of the total pressure recovery for two shapes is summarized in Table 4.1, which demonstrates that the oval probe retrieves higher total pressure recovery up to 4.6 percentage-points.

Table 4.1: Total pressure recovery for two characterized probe shapes at two inlet Mach numbers.

	Mach=0.3		Mach=0.75	
	Trapezoidal	Oval	Trapezoidal	Oval
C_{pa}	0.92	0.93	0.923	0.966

In the time-resolved pressure measurements, probe shape was characterized in terms of the sensitivity to vortex shedding. A statistical analysis was conducted at several Mach numbers and yaw angles. Figures 4.11 and 4.12 depict the instantaneous vortex shedding downstream of the two probe shapes for two inlet Mach numbers (0.3 for Fig. 4.11 and 0.75 for Fig. 4.12) at two time frames for 0 yaw angle. Vortex shedding frequencies based on the CFD evaluation were summarized in Table 4.2. For an inlet Mach number of 0.75, vortex shedding frequency was enhanced for both characterized shapes. Numerical results were verified against theoretical St-Re correlation [71] by applying Equation (4.3).

$$St = \frac{fD}{V} \quad (4.3)$$

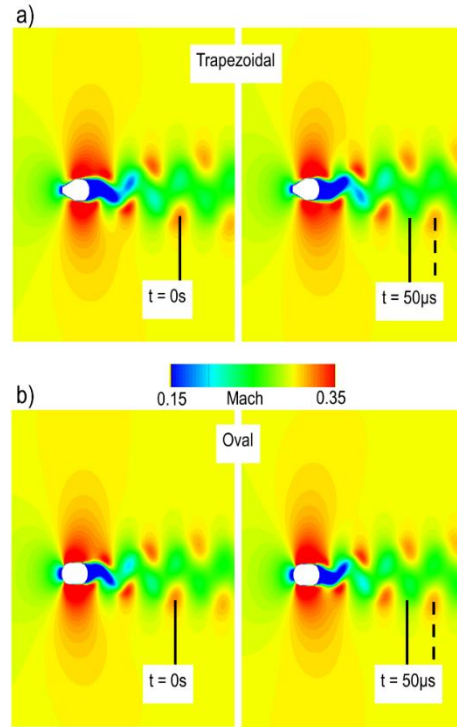


Figure 4.11. Instantaneous vortex shedding at two time frames for an inlet Mach number of 0.3 and 0 yaw angle downstream of the two characterized probe shapes: a) trapezoidal, and b) oval.

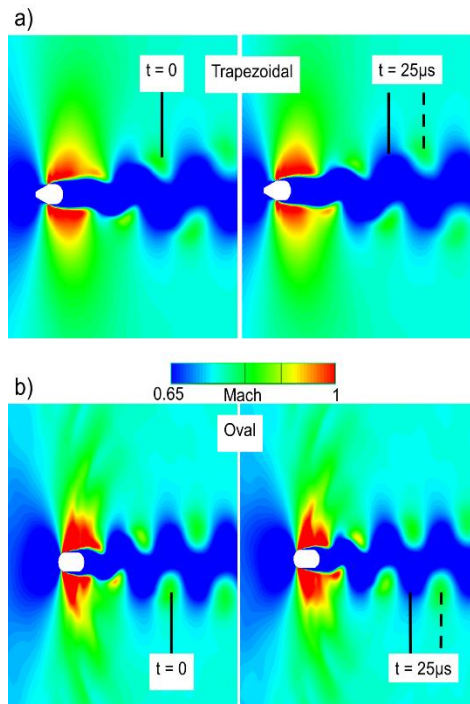


Figure 4.12. Instantaneous vortex shedding at two time frames for an inlet Mach number of 0.75 and 0 yaw angle downstream of the two characterized probe shapes: a) trapezoidal, and b) oval.

Table 4.2: Vortex shedding frequency in functions of inlet Mach numbers and yaw angles for two characterized probe shapes.

	Mach=0.3		Mach=0.75	
	Trapezoidal	Oval	Trapezoidal	Oval
Yaw=0°	10.7±0.5 kHz	11.3±0.5 kHz	18.6±0.5 kHz	21.8±0.5 kHz
Yaw=-12°	9.2±0.5 kHz	9.3±0.5 kHz	20.2±0.5 kHz	17.4±0.5 kHz
St-Re correlation	9.0~9.2 kHz		19.8~20.3 kHz	
Re	22800	22800	46300	46100

For a perfect sinusoidal signal, the statistical parameter MinMax is defined in Equation (4.4), which was evaluated at all five equiangular locations (Fig. 4.1a, c) on two characterized probe shapes to quantify the unsteadiness sensitivity for two inlet Mach numbers and two yaw angles. Figures 4.13a-d display MinMax in function of probe coordinate, yaw angle, and inlet Mach number. The trapezoidal probe revealed a maximum of 5 percentage-points higher unsteadiness sensitivity than the oval probe. Interestingly, sharp corners (trapezoidal) are not better to attenuate vortex shedding fluctuations than smooth curves (oval). The location of lateral pressure tappings should be avoided on point “e” of the oval probe due to the intense vortex shedding unsteadiness.

$$MinMax = \frac{Max - Min}{P_{0in} - P_{sin}} \quad (4.4)$$

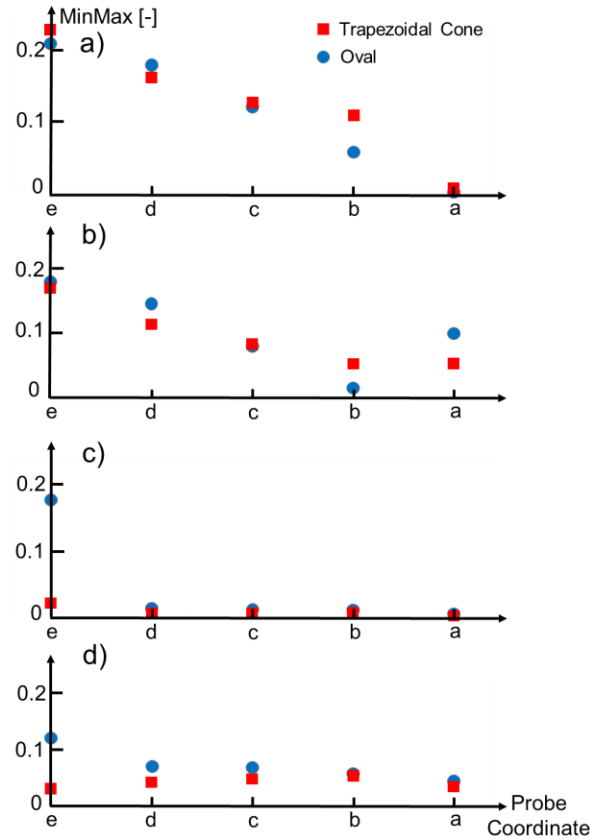


Figure 4.13. MinMax in function of probe coordinate for a) an inlet Mach number of 0.3 and 0 yaw angle, b) an inlet Mach number of 0.3 and -12° yaw angle, c) an inlet Mach number of 0.75 and 0 yaw angle, d) an inlet Mach number of 0.75 and -12° yaw angle.

4.3 Two-Dimensional Evaluation of Oval Probe Performance

The oval probe was selected with line-cavity systems introduced which is delineated in Fig. 4.14. The downstream velocity sensor was utilized to retrieve the vortex shedding frequency and two recessed sensors (sensor 1 and sensor 2) were mounted at the end of the pneumatic lines. One central and two lateral pressure tappings were drilled perpendicular to the head surface. Lateral pressure tappings are located at 50° from the central axis. Diameter of pneumatic lines starts with 0.3mm and expands to 0.6mm.

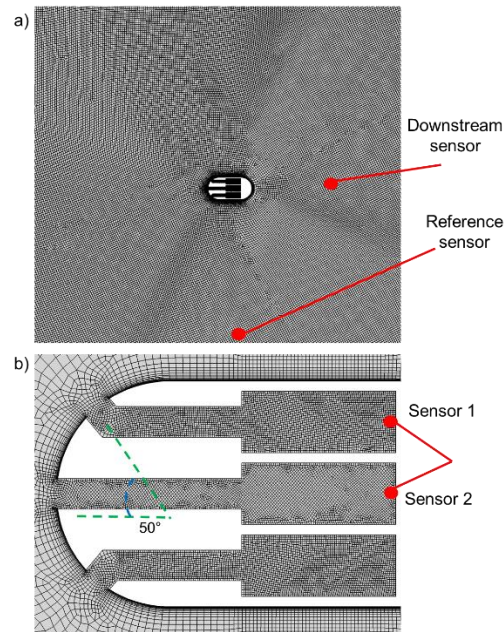


Figure 4.14. a) Computation domain. b) Oval probe with pressure tappings.

Analyses of the unsteady circulation, and effect of the pneumatic line are fundamental to ensure an accurate pressure reading. Frequency analyses were performed on the downstream velocity sensor as well as on the two recessed sensors (sensor 1 and sensor 2) inside the oval tube as shown in Fig. 4.14. Frequency spectrum retrieved by all three sensors were carefully evaluated. Figure 4.15a identifies the vortex shedding frequency as 11 ± 0.5 kHz for an inlet Mach number of 0.3 and a higher shedding frequency of 18.75 ± 0.5 kHz was retrieved for an inlet Mach number of 0.6 in Fig. 4.15d. Additionally, at inlet Mach number 0.3, Figure 4.15a reveals the first, the second, and the third harmonic after the dominant vortex shedding frequency and their amplitudes decrease by 50%. At inlet Mach number 0.6, Figure 4.15d reveals the occurrence of the second harmonic and its amplitude declines by more than 50%.

For an inlet Mach number of 0.3, Figures 4.15b and 4.15c display the frequency spectrum retrieved by the recessed sensor 1 and sensor 2, where the identical vortex shedding frequency of 11 ± 0.5 kHz is observed. However, the amplitude of harmonics retrieved by recessed sensor 1 is far lower than that of the dominant shedding frequency while the amplitude of the first harmonic retrieved by recessed sensor 2 is larger. In addition, Figure 4.15c indicates that the acoustic wave traveling at the frequency of 3.5 ± 0.5 kHz is observed and dominates the frequency response of recessed sensor 2. On the other hand, for an inlet Mach number of 0.6, Figure 4.15e and 4.15f

depicts the frequency spectrum retrieved by recessed sensor 1 and sensor 2, where the same vortex shedding frequency of 18.75 ± 0.5 kHz was revealed as well as the acoustic resonance of 2.7 ± 0.5 kHz. However, the frequency of the traveling acoustic wave was attenuated due to the lower static temperature. Frequency spectrum of recessed sensors demonstrate that shedding unsteadiness has propagated into the pneumatic lines and pressure readings were affected.

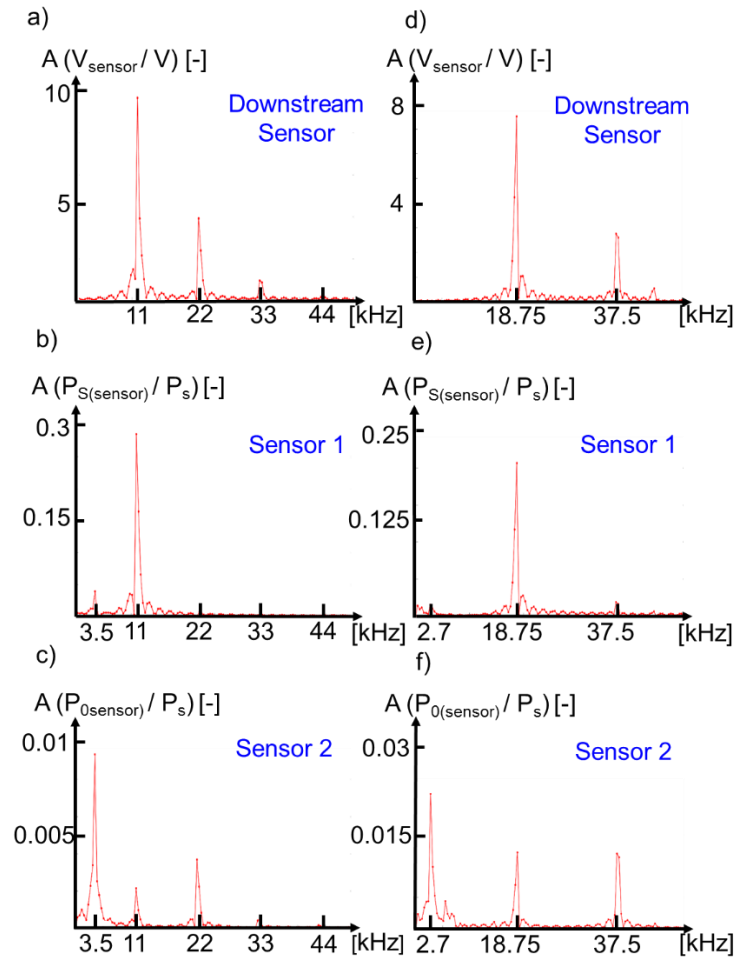


Figure 4.15. Frequency spectrum for an inlet Mach number of 0.3 retrieved by a) downstream velocity sensor, b) recessed sensor 1, c) recessed sensor 2. Frequency spectrum for an inlet Mach number of 0.6 retrieved by d) downstream velocity sensor, e) recessed sensor 1, f) recessed sensor 2.

Resonance frequency of the line-cavity system is essential to analyzing the dynamic behavior of pneumatic lines. Firstly, the traditional analytic model introduced by Whitmore- Leondes [72] was implemented applying Equation (4.5). The resonance frequency of the central line-cavity system was identified as 22.6 kHz for an inlet Mach number of 0.3.

$$f_n = \frac{a}{2\pi L} \sqrt{\frac{1}{0.5 + \frac{V_c}{V_t}}} \quad (4.5)$$

Afterwards, to verify the traditional analytic model, the numerical methodology was implemented by initiating a total pressure step after unsteady simulations were periodically converged. Transfer functions between the reference (18D span-wise downstream from sensor 2) and recessed sensor 2 were evaluated to resolve the resonance frequency of the central line-cavity system. Figure 4.16a displays the non-dimensional pressure retrieved by the reference and recessed sensors, non-dimensionalized by upstream total pressure, for an inlet Mach number of 0.3. The obtained transfer function is illustrated in Fig. 4.16b. The resonance frequency from the numerical approach is identified as 20.8 kHz for an inlet Mach number 0.3, which is lower than the predictions from the Whitmore-Leondes [72] model.

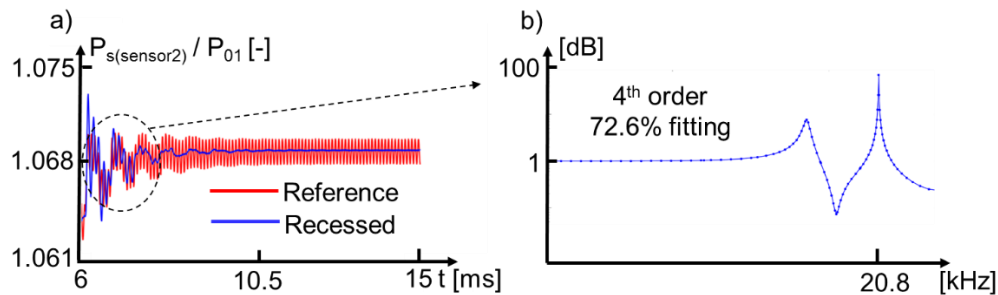


Figure 4.16. a) Non-dimensional pressure retrieved by reference and recessed sensor for an inlet Mach number of 0.3. b) Transfer function identification.

Finally, a more complex analytic model developed by Bergh- Tijdeman [68] utilizing a general recursive formula was implemented to reevaluate the resonance frequency. The model predicts a frequency response of 17.3 kHz.

4.4 Three-Dimensional Design

Based on the probe shape characterization, the proposed directional probe design, depicted in Fig. 4.17a, consists of a 3mm-diameter hemispherical head which is mounted on a 3.7mm-diameter

cylindrical stem. The structure of internal tubes is illustrated in Fig. 4.17b. Five miniature Kulite sensors are embedded inside the Inconel probe. Additionally, the five recessed sensors located in the stem provide an improved performance in a wider range of Mach number, from low subsonic to transonic.

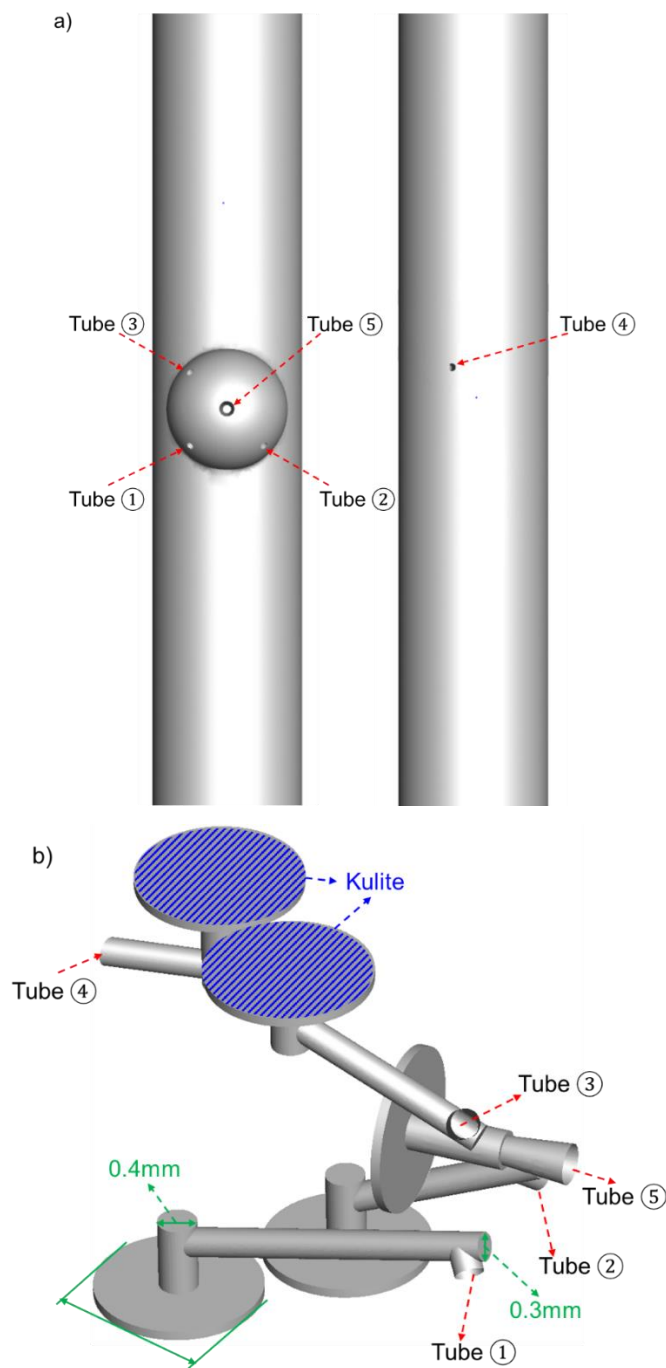


Figure 4.17. a) 3D design of the directional probe. b) Internal structures of the pressure tapings.

Figures 4.18a-c display the 3D computational domain together with 2D cuts. The grid was unstructured with around 6,400,000 cells depicted in Fig. 4.18d. A zoomed mid-cut grid parallel to the flow direction is shown in Fig. 4.17e. The convention of yaw and pitch is defined in Fig. 4.19a. Figure 4.19b delineates the steady Mach contours at 0 pitch and various yaws for an inlet Mach number of 0.3. To perform time-averaged measurements of the directional probe, twelve 3D steady simulations were carried out. The steady performance of the probe was characterized at different pitches and yaws using pressure coefficient defined in Equation (4.6). The ‘k’ represents the location of each tube on the hemispherical head when pressure tapplings are closed.

$$C_{pk} = \frac{P_{Sk} - P_{Sin}}{P_{0in} - P_{Sin}} \quad (4.6)$$

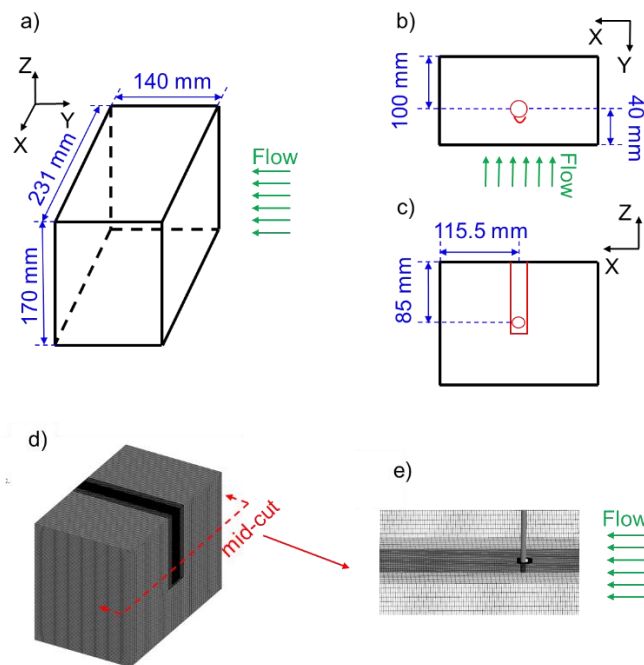


Figure 4.18. a) 3D computational domain. b) Top view, and c) front view of the computational domain. d) Numerical grid. e) 2D mid-cut of the numerical grid.

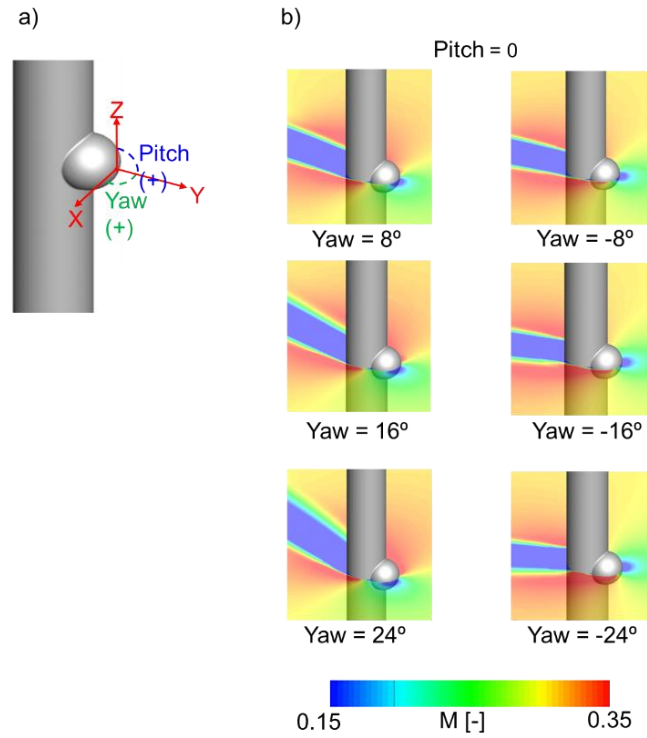


Figure 4.19. a) Convention of yaw and pitch angle. b) Steady Mach contours in function of yaw angle for an inlet Mach number of 0.3 and 0 pitch angle.

Steady results delineated in Fig. 4.20 illustrate that based pressure readings located in the wake region are less sensitive to angle incidences, where pressure coefficient changes less than 0.15 from -16 to 16 degrees. Positive pitches reduce sensitivity to yaw variations and total pressure recovery rises as yaw approaches 0.

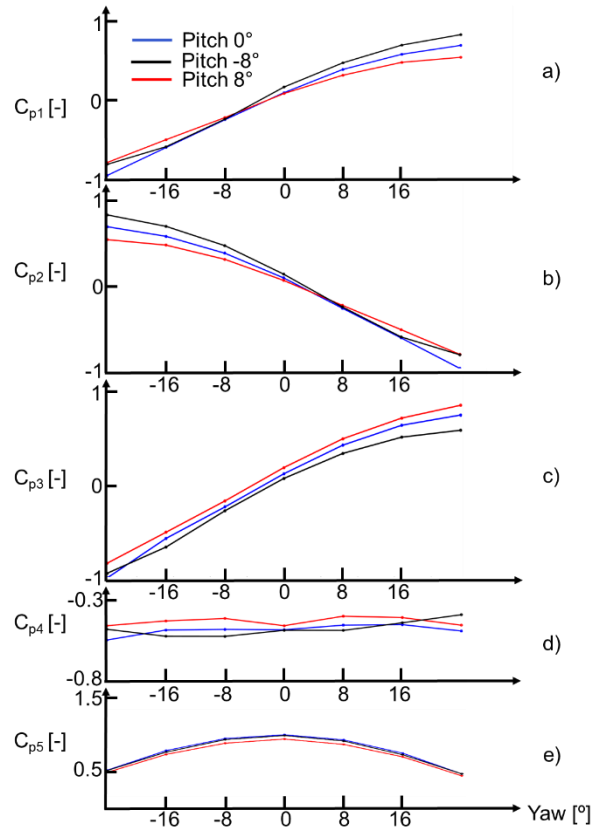


Figure 4.20. C_{pk} in function of yaw and pitch angles for an inlet Mach number of 0.3 evaluated at: a) Tube 1, b) Tube 2, c) Tube 3, d) Tube 4, and e) Tube 5.

4.4.1 Angular Calibration of Probe

Angular calibration is essential to minimize the error in the flow angle, static, and total pressure measurements. The calibration procedure follows an in-house data reduction algorithm [73], shown in Fig. 4.21. One hundred and sixty-nine RANS simulations were simulated at an inlet Mach number of 0.3 to create a calibration database, with yaw and pitch angles ranging from -24° to 24° at an increment of 4° . The pressure readings from frontal tappings, Tube 1, Tube 2, Tube 3, Tube 5, together with an initial guess of the static pressure, are used to compute the following pressure coefficient (Equation 4.7-4.11, [73]):

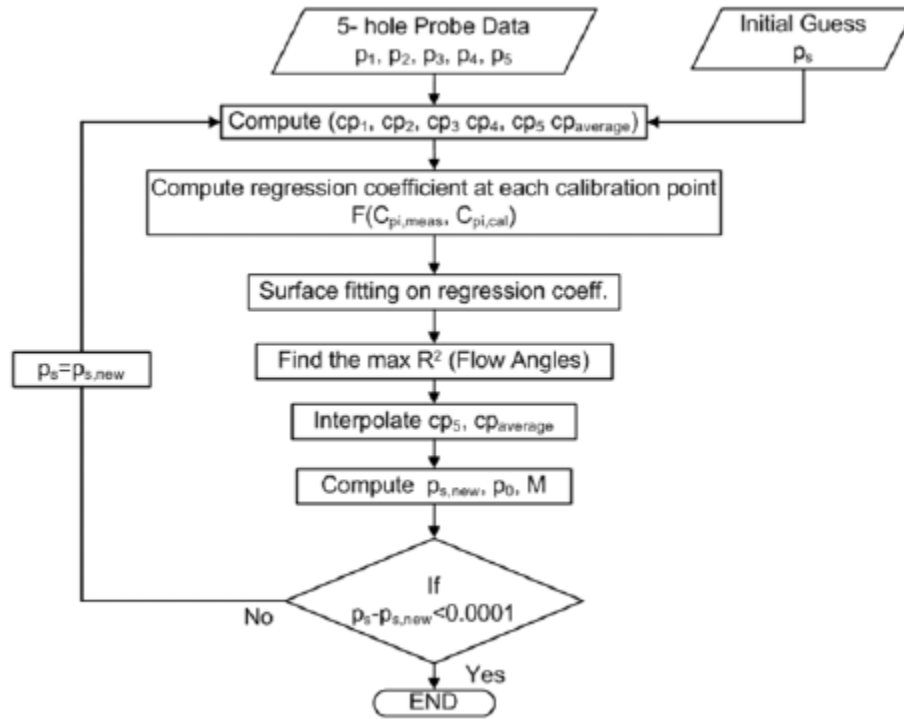


Figure 4.21. Data reduction algorithm [73].

$$C_{p1} = \frac{P_{S1} - P_S}{P_{S5} - P_S} \quad (4.7)$$

$$C_{p2} = \frac{P_{S2} - P_S}{P_{S5} - P_S} \quad (4.8)$$

$$C_{p3} = \frac{P_{S3} - P_S}{P_{S5} - P_S} \quad (4.9)$$

$$C_{p5} = \frac{P_{S5} - P_S}{P_{01} - P_S} \quad (4.10)$$

$$C_{pmean} = \frac{\text{mean}(P_{S1-3}) - P_S}{P_{01} - P_S} \quad (4.11)$$

The contours of computed pressure coefficient are depicted in Fig. 4.22, displaying solitary characteristics between flow angles and measured pressure and indicating that only one angle corresponds to a certain combination of pressure readings [73]. Afterwards, the pressure coefficients are compared to the data in the calibration database, by assessing a regression coefficient. The pressure is found when the regression coefficient becomes unity. A surface fitting is performed to relate the regression coefficient to yaw and pitch angles, where the surface peak represents the flow angles. Finally, the static ($C_{p\text{mean}}$) and total (C_{p5}) pressure are interpolated according to the flow angles. The interpolated static pressure is compared to the initial guess of static pressure to assess the convergence. The entire process is iterated till the overall convergence is achieved.

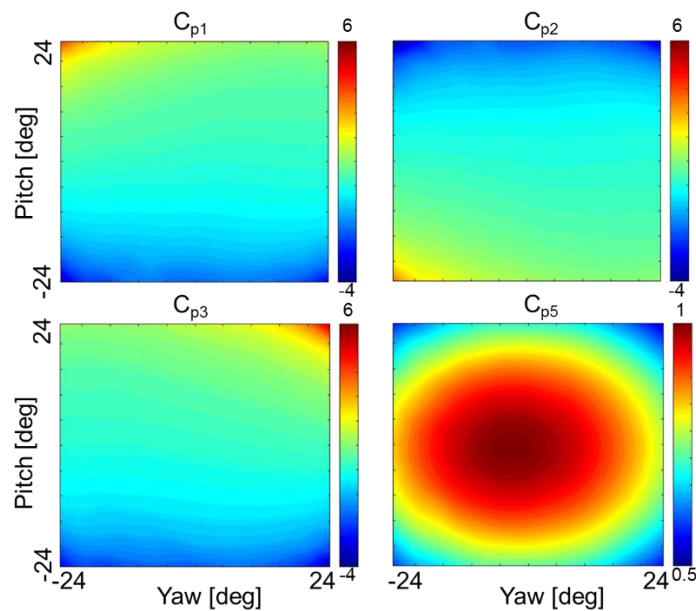


Figure 4.22. Contour of pressure coefficient in function of yaw and pitch angle.

Two test cases are utilized to assess the accuracy of the calibration algorithm and results are summarized in Table 4.3 (case 1: yaw=14°, pitch=14°; case2: yaw=18°, pitch=2°). The maximum error is around 1.39% in yaw angle measurement, indicating the validity of the algorithm.

Table 4.3: Accuracy assessment of the calibration algorithm.

	Case 1	Case 2
Error_{yaw}	0	1.39%
Error_{pitch}	0	0

Table 4.3: Continued.

Error_{Ps}	0.027%	0.016%
Error_{P0}	0.016%	0.032%

4.4.2 Unsteady Performance Assessment of Directional Probe

To characterize the vortex shedding unsteadiness induced by the probe stem, a 3D unsteady simulation was performed and instantaneous vortex shedding downstream of the directional probe is displayed in Fig. 4.23. The total computational time for a 3D URANS simulation was about 432 hours on 20 cores of one Intel Xeon-E5 processor to achieve periodic convergence. Figure 4.24 plots the frequency spectrum retrieved by all Kulite sensors and the vortex shedding frequency is identified as $4.4 \pm 0.5 \text{ kHz}$ by the base sensor. Afterwards, CFD results were verified against theoretical $St-Re$ correlation [71] as shown in Table 4.4, revealing a good agreement considering the frequency resolution. At Kulite 5 where total pressure is measured, the effect of vortex shedding unsteadiness is substantially reduced. Frequency spectrum retrieved by Kulites explicates the propagation of vortex shedding unsteadiness into the pneumatic lines and time-resolved pressure readings were affected.

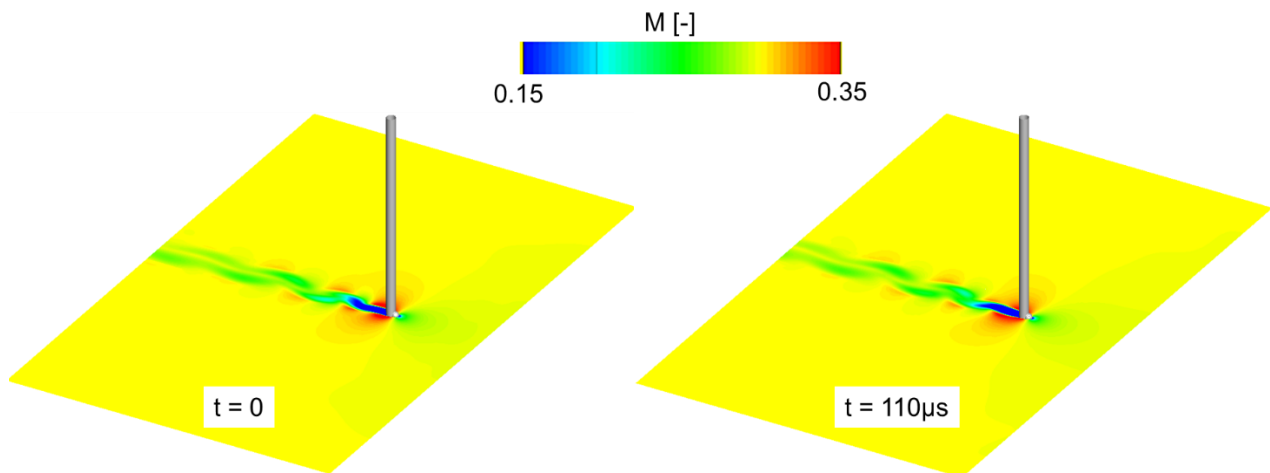


Figure 4.23. Instantaneous vortex shedding downstream of the directional probe at two time frames for an inlet Mach number of 0.3.

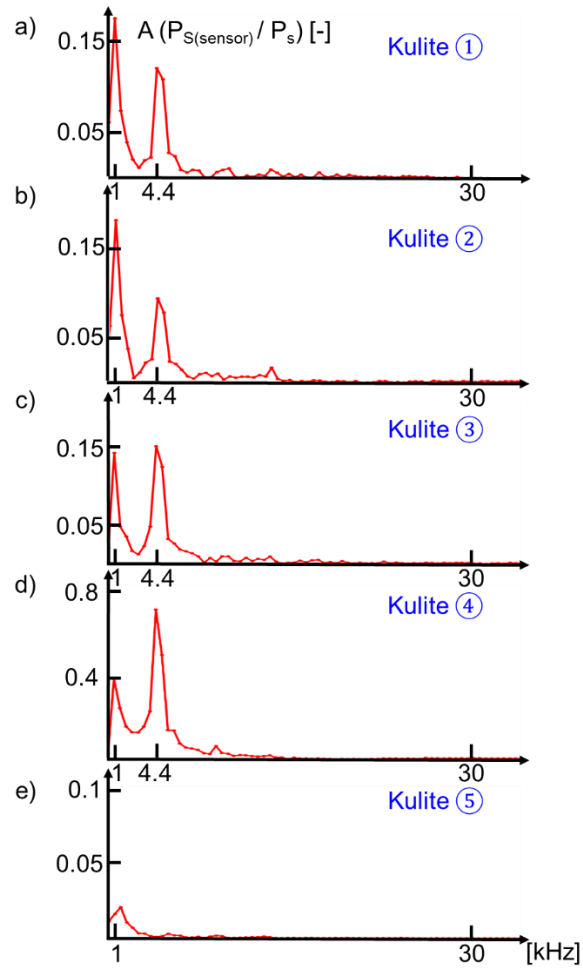


Figure 4.24. Frequency spectrum for an inlet Mach number of 0.3 retrieved by a) Kulite 1, b) Kulite 2, c) Kulite 3, d) Kulite 4, and e) Kulite 5.

Table 4.4: Vortex shedding frequency evaluated by St-Re correlation for a Mach number of 0.3.

Mach=0.3	
Re	37700
Confinement ratio	1.6%
St	0.195~0.2
f	5.12~5.25 kHz

Probe frequency response is represented by the resonance frequency of the internal tube-cavity system, which characterize the acoustic excitation in these recessed lines. Figure 4.25a illustrates a schematic sketch of the tube-cavity system adopted in the probe design with subsurface-mounted sensors, recessed from the probe head. In this case, we implemented the analytic model of Bergh

and Tijdeman [68] and results in Fig. 4.25b imply that increasing tube length could significantly reduce the probe frequency response.

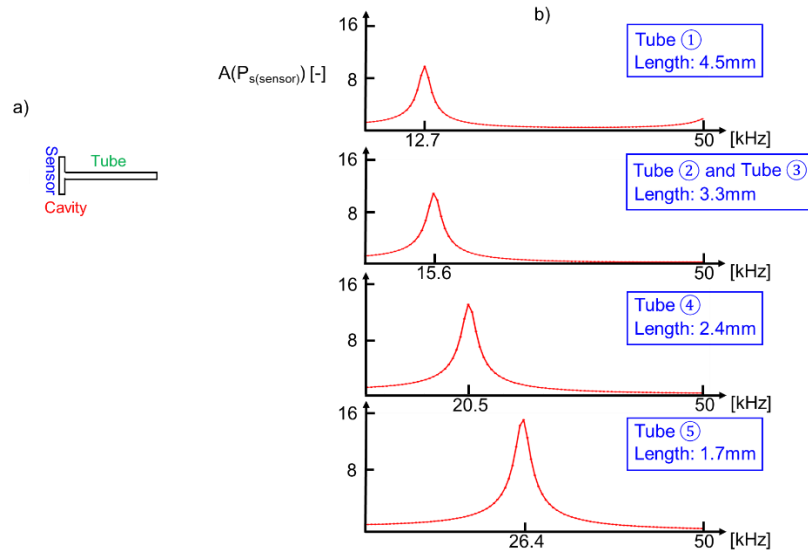


Figure 4.25. a) Schematic sketch of the line-cavity system. b) Resonance frequency of all five tube-cavity systems inside the directional probe.

4.5 Biomimicry-Inspired Design to Attenuate Vortex Shedding Unsteadiness

From the frequency spectrum retrieved by the cylindrical probe in Fig. 4.24, it is noticed that the time-resolved pressure measurements have been interfered by the induced vortex shedding due to the probe intrusion. To reduce the effect of vortex shedding perturbation, a biomimicry-like probe design inspired by the harbor seal whiskers is proposed. In the oceanic environment, seal whiskers generate vortex shedding pattern. When the shedding frequency agrees with the resonance frequency of the whisker, a self-vibration is caused that could be detected by their predators. To avoid the fatal consequence, seals developed their own unique wavy structure to minimize the effect of vortex shedding perturbation. Figure 4.26a depicts the whisker-inspired probe design, with undulations imposed on the original cylindrical stem. The design is featured with periodic waves, with the major axis parallel to the flow direction suggested in [35]. The diameter of the minor axis is 3.7 and 4mm, while that of the major axis is 5 and 5.5mm. Figure 4.26b shows the frequency spectrum of all Kulite sensors. Compared to the cylindrical design, the amplitudes of the vortex shedding were reduced in all sensors, up to 76% in the base tapping.

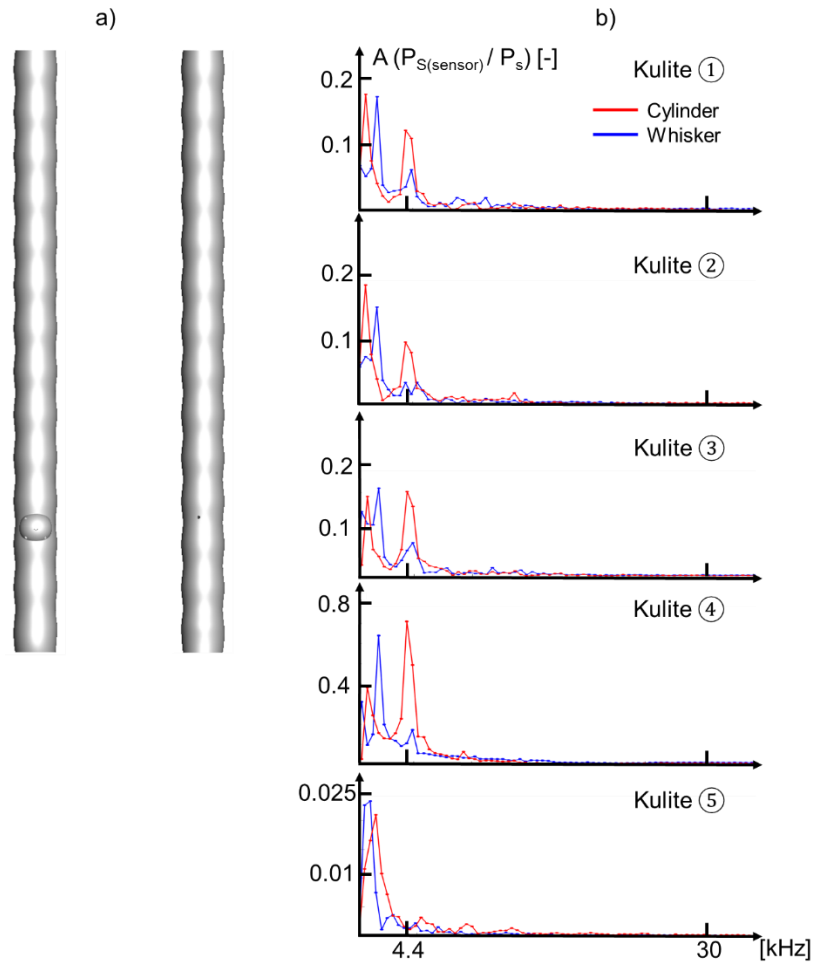


Figure 4.26. Whisker probe: a) Frontal view and b) Rear view. c) Comparison of the frequency spectrum retrieved by Kulites between the cylindrical probe and the whisker probe.

5. CONCLUSION

A supersonic axial turbine able to ingest the flow downstream of a rotating detonation combustor was designed. In terms of the aerodynamic assessment, the steady performance of a supersonic turbine was first evaluated. The turbine was designed via a method of characteristics solver for a Mach 2 inflow. The relative total pressure loss in the rotor was 15.5%, leading to a power output of 13.7MW. Secondly, the unsteady turbine performance was characterized with increased level of complexity. The performance of the supersonic stator passages exposed to rotating oblique shocks was evaluated for several frequencies and amplitudes of the oblique shock, confirming the importance of well-designed nozzles to damp the outlet fluctuations of RDCs. For all frequencies and amplitudes, the angular fluctuations were attenuated across the stator passage by up to 84.6%. Total pressure loss across the stator ranged between from 20% and 34%, depending on the inlet fluctuations. Afterwards, the stator outlet profiles were extracted and imposed at the supersonic rotor inlet with a resulting power extraction of 10.6MW. The relative total pressure drop was 30.2% and angular fluctuations were further damped. Finally, a full stage analysis was performed. Unsteady stage simulation revealed a total pressure loss of 23.1% across the stator and relative total pressure loss across the rotor was identified as 26.5%. The frequency content displayed a decrease of amplitude at the dominant frequency by 41.7% from stator inlet to rotor inlet. Detailed loss budgeting showed that the leading edge shock waves were the main contributors to the overall unsteady loss mechanism. A performance map was constructed, exploring the operating range of the supersonic turbine at various off-design conditions.

In terms of the heat transfer assessment, the adiabatic wall temperature evaluation method serves as a reliable prediction of the real adiabatic wall temperature when compared to the adiabatic simulation and is the driving factor for the unsteady heat flux signature for supersonic turbines exposed to RDC outflow. However, the detrimental effect of the sweeping oblique shock on the driving temperature was balanced at some locations due to a decrease in local heat transfer coefficient. Due to the unsteadiness, the discrepancy in integral heat load between the steady and unsteady evaluation is less than 8%.

A retrofit strategy of an existing high-pressure subsonic axial turbine with a RDC was proposed. The strategy was achieved through contouring the stator endwall without redesigning the vane and rotor blades.

In the first phase, steady two-dimensional and three-dimensional simulations were performed. Afterwards, the performance of the turbine under pulsating inlet conditions was evaluated using an array of different numerical methods by increasing the level of fidelity. The stator passage was submitted to fluctuating inlet conditions and modeled without rotor. This was compared to stage simulations with mixing plane and pitch-wise averaging which allowed for time-resolved variations in the rotor. Finally, full unsteady simulations were performed. This stepped approach enabled to unveil the main physical mechanisms and precisely document the effects associated to the unsteady inlet, the diffusion across the vane passage and the unsteady stator-rotor interactions. Detailed loss budgeting revealed that the stator exposed to unsteady inlet conditions triplicates the loss compared to the steady case, which agrees with Traupel's and Denton's correlations. The performance was constrained by three major factors. First of all, the high inlet Mach number limits the performance. To avoid the unstating of the stator passage upstream of the throat, the turbine endwalls were opened by a factor of two to allow for an inlet Mach number 0.3, and by a factor of three for an inlet Mach number of 0.6. Secondly, the amplitude of the fluctuations influences the unsteady separation bubbles caused by the interaction of the large endwall diffusion and the secondary flows. Thirdly, the frequency of the inlet excitation relative to the speed of propagation, i.e. the reduced frequency, determines the growth mechanism of the bubble and hence the turbine efficiency and damping as well. In conclusion, if efficiencies of 85% or higher are required without altering the vanes or rotor blades, the diffuser needs to decelerate the turbine inlet Mach number to around 0.3 and damp the fluctuations to peak-to-mean amplitudes below 25%. At the expense of higher turbine losses, a higher diffusion rate throughout the stator passage is possible.

In the second phase, a multi-step optimization routine of the endwall contouring was performed to enhance the turbine aerodynamic performance. The optimization strategy starts with a steady routine, which consists of turbine channel parametrization, mesh generation, RANS simulations and post-processing of objective functions. Three hundred and sixty eight endwall geometries were generated and detailed assessment shows that an efficiency increase of 12.5% was reached under the steady condition. It was found that separation intensity for the optimized endwalls was lowered and resulted in a decrease of total pressure loss. Several critical design parameters were identified and provided for the next-step unsteady routine. In the unsteady optimization, URANS simulations with the mixing plane approach were performed with a large amplitude fluctuating inlet and 37 endwall profiles were created. An efficiency surge of 21.4% was achieved compared to the

baseline under the pulsating conditions. Afterwards, full unsteady simulations, in which turbine unsteadiness was fully resolved, were carried out on selected optimized profiles and results demonstrated that the final unsteady-optimized profile outperforms the baseline design by up to 13 percentage-points. The multi-step optimization strategy unveils that the balance between flow diffusion and acceleration induced by the endwall contouring plays a major role in the performance of high-pressure transonic turbines operating at high inlet Mach numbers. In the baseline turbine, the stator passage acts as a diverging-converging channel, since the endwall contouring occurs in the stator and diffusion-acceleration coexists. In contrast, the optimization geometry has diffusion upstream of the stator such that a converging channel is obtained in the stator passage and flow turning and acceleration can be enhanced. Finally, an engine model shows an improvement of 10 percentage-points when an optimized turbine is integrated. Up to 2 percentage-points of thermal efficiency decrease was found when the unsteady-optimized turbine was replaced by the baseline profile. The effect of stator endwall contouring is especially critical in the medium-to-high overall engine compression ratio regions as it would result in lower cycle efficiencies than deflagration-based engine configurations. The selected optimized turbine was further characterized at a wide range of off-design condition, including different RPM and total-to-static pressure ratio, via a comprehensive performance map. Design of experiments was proposed to replicate the diffusion in the optimized stator endwall geometry in the PETAL linear wind tunnel. The test article consists of three modular components and respects the turbine inlet Re .

A fast-response directional probe was designed and serves as a flow measurement tool. Firstly, a hemispherical (oval in 2D) and pyramidal probe (trapezoidal in 2D) were compared. This analysis led to the selection of the oval shape, due to the benefits on the total pressure recovery. However, the trapezoidal probe evidences higher angle sensitivity. A substantial reduction of the angle sensitivity is observed in the transonic regime. Regarding the frequency analysis, both oval and trapezoidal caused a similar vortex shedding, and the pressure tappings were both excited to a similar amplitude, with a noticeable amplification within the transonic range. Hence, the sharp edges of a conical or pyramidal probe are not better than smooth curves of an oval or hemispherical probe to attenuate the vortex shedding unsteadiness. Secondly, the oval probe including recessed line-cavity systems was selected to investigate in detail the unsteady performance, the effect of the vortex shedding on the measurements, and the acoustic damping. For the considered length, the estimated resonance frequency was about 17.3 kHz. Afterwards, the compact high-frequency

multi-hole probe with sub-surface sensors, recessed from the measurement locations, was evaluated using 3D URANS computation. The numerical simulations indicate that the base pressure tapping is rather insensitive to angle variations and the pressure coefficient changes less than 0.1 from a yaw angle of -16 to 16 degrees. Angular calibration was performed via an in-house data reduction algorithm. A calibration database consisting of 169 RANS cases was built. The resonance frequency of all the pneumatic lines ranges from 13 kHz to 26 kHz, as the recessed length varies. Finally, a bio-inspired probe design was explored to reduce the vortex shedding effect. A periodic wave pattern was imposed on the cylindrical stem of the probe, resulting in an attenuation of vortex shedding amplitude by around 76%.

REFERENCES

- [1] Fan, W., Yan, C., Huang, X., Zhang, Q., and Zheng, L., 2003, “Experimental Investigation on Two-Phase Pulse Detonation Engine,” *Combustion and Flame*, Vol. 133, No. 4, pp. 441-450. DOI: [https://doi.org/10.1016/S0010-2180\(03\)00043-9](https://doi.org/10.1016/S0010-2180(03)00043-9)
- [2] Shao, Y., Liu, M., and Wang, J.-P., 2010, “Continuous Detonation Engine and Effects of Different Types of Nozzle on Its Propulsion Performance,” *Chinese Journal of Aeronautics*, Vol. 23, No. 6, pp. 647-652. DOI: [https://doi.org/10.1016/S1000-9361\(09\)60266-1](https://doi.org/10.1016/S1000-9361(09)60266-1)
- [3] Davidenko, D. M., Gokalp, I., and Kudryavtsev, A. N., 2008, “Numerical Study of the Continuous Detonation Wave Rocket Engine,” *Proceedings of the 15th AIAA International Space Planes and Hypersonic Systems and Technologies Conference*, April 28-May 1, Dayton, Ohio. DOI: <https://doi.org/10.2514/6.2008-2680>
- [4] Roy, A., Ferguson, D. H., Sidwell, T., O’Meara, B., Strakey, P., Bedick, C., and Sisler, A., 2017, “Experimental study of rotating detonation combustor performance under preheat and back pressure operation,” *55th AIAA Aerospace Science Meeting*, January 9-13, Grapevine, Texas. DOI: <https://doi.org/10.2514/6.2017-1065>
- [5] Le Naour, B., Falempin, F. H., and Coulon, K., 2017, “MBDA R&T Effort Regarding Continuous Detonation Wave Engine for Propulsion –Status in 2016,” *21st AIAA International Space Planes and Hypersonics Technologies Conference*, March 6-9, Xiamen, China. DOI: <https://doi.org/10.2514/6.2017-2325>
- [6] Eude, Y., Davidenko, D. M., Gokalp, I., and Falempin, F., 2011, “Use of the Adaptive Mesh Refinement for 3D simulations of a CDWRE (Continuous Detonation Wave Rocket Engine),” *Proceedings of the 17th AIAA International Space Planes and Hypersonic Systems and Technologies Conference*, April 11-14, San Francisco, California. DOI: <https://doi.org/10.2514/6.2011-2236>
- [7] Schwer, D., and Kailasanath, K., 2011, “Numerical Investigation of the Physics of Rotating-Detonation-Engines,” *Proceedings of the Combustion Institute*, Vol. 33, No. 2, pp. 2195-2202. DOI: <https://doi.org/10.1016/j.proci.2010.07.050>

- [8] Schwer, D., and Kailasanath, K., 2011, "Numerical Study of the Effects of Engine Size on Rotating Detonation Engines," *Proceedings of the 49th AIAA Aerospace Sciences Meeting Including the New Horizons Forum and Aerospace Exposition*, January 4-7, Orlando, Florida. DOI: <https://doi.org/10.2514/6.2011-581>
- [9] Zhou, R., and Wang, J.-P., 2013, "Numerical Investigation of Shock Wave Reflections near the Head Ends of Rotating Detonation Engines," *Shock Waves*, Vol. 23, No. 5, pp. 461-472. DOI: <https://doi.org/10.1007/s00193-013-0440-0>
- [10] Frolov, S., Dubrovskii, A., and Ivanov, V., 2013, "Three-Dimensional Numerical Simulation of Operation Process in Rotating Detonation Engine," *Proceedings of the Progress in Propulsion Physics*, Vol. 4, pp. 467-488. DOI: <https://doi.org/10.1051/eucass/201304467>
- [11] Dubrovskii, A., Ivanov, V., and Frolov, S., 2015, "Three-Dimensional Numerical Simulation of the Operation Process in a Continuous Detonation Combustor with Separate Feeding of Hydrogen and Air," *Russian Journal of Physical Chemistry B*, Vol. 9, No. 1, pp. 104-119. DOI: <https://doi.org/10.1134/S1990793115010157>
- [12] Cocks, P. A., Holley, A. T., and Rankin, B. A., 2016, "High Fidelity Simulations of a Non-Premixed Rotating Detonation Engine," *Proceedings of the 54th AIAA Aerospace Sciences Meeting*, January 4-8, San Diego, California. DOI: <https://doi.org/10.2514/6.2016-0125>
- [13] Fievisohn, R. T., and Yu, K. H., 2016, "Steady-State Analysis of Rotating Detonation Engine Flowfields with the Method of Characteristics," *Journal of Propulsion and Power*, Vol. 33, No. 1, pp. 89-99. DOI: <https://doi.org/10.2514/1.B36103>
- [14] Sousa J., Braun J., and Paniagua G., 2017, "Development of a fast evaluation tool for rotating detonation combustors," *Applied Mathematical Modelling*, Vol. 52, pp. 42-52. DOI: <https://doi.org/10.1016/j.apm.2017.07.019>
- [15] Braun, J., Saracoglu, B.H., and Paniagua, G., 2016, "Unsteady Performance of Rotating Detonation Engines with Different Exhaust Nozzles," *Journal of Propulsion and Power*, Vol. 33, No. 1, pp. 121-130. DOI: <https://doi.org/10.2514/1.B36164>
- [16] Braun, J., Saavedra, J., and Paniagua, G., 2017, "Evaluation of the unsteadiness across nozzles downstream of rotating detonation combustors," 55th AIAA Aerospace

- Sciences Meeting, January 9-13, Grapevine, Texas. DOI: <https://doi.org/10.2514/6.2017-1063>
- [17] Paniagua, G., Lorio, M.C., Vinha, N., and Sousa, J., 2014, "Design and Analysis of Pioneering High Supersonic Axial Turbines," *International Journal of Mechanical Science*, Vol. 89, pp. 65-77. DOI: <https://doi.org/10.1016/j.ijmecsci.2014.08.014>
- [18] Daneshyar, H., Edwards, K.J., Horlock, J.H., Janota, M.S., Pearson, R.D., and Shaw, R., 1969, "A Comparison of the Performance of Three Model Axial Flow Turbines Tested Under Both Steady and Pulse Flow conditions," *Proceedings of the Institution of Mechanical Engineers*, Vol. 184, Pt. 1, No. 61, pp. 1119-1134. DOI: https://doi.org/10.1243/PIME_PROC_1969_184_082_02
- [19] Fernelius, M., Gorrel, S., Hoke, J., and Schauer, F., 2013, "Effect of Periodic Pressure Pulses on Axial Turbine Performance," *49th AIAA/ASME/SAE/ASEE Joint Propulsion Conference*, July 14-17, San Jose, CA.. DOI: <https://doi.org/10.2514/6.2013-3687>
- [20] St. George, A., Driscoll, R., Gutmark, E., and Munday, D., 2014, "Experimental Comparison of Axial Turbine Performance under Steady and Pulsating Flows," *Journal of Turbomachinery*, Vol. 136, No. 11, p. 111005. DOI: <https://doi.org/10.1115/1.4028115>
- [21] Rasheed, A., Furman, H.A., and Dean, J.A., 2011, "Experimental Investigations of the Performance of a Multitube Pulse Detonation Engine System," *Journal of Propulsion and Power*, Vol. 27, No. 3, pp. 586:596. DOI: <https://doi.org/10.2514/1.B34013>
- [22] Ni, R.H., Humber, W., and Ni, M., 2013, "Performance Estimations of a Turbine under Partial-Admission and Flow Pulsation Conditions at Inlet," *Proceedings of ASME Turbo Expo: Turbine Technical Conference and Exposition*, June 3-7, San Antonio, Texas. DOI: <https://doi.org/10.1115/GT2013-94811>
- [23] Fernelius, H.M., and Gorrell, E.S., 2017, "Predicting Efficiency of a Turbine Driven by Pulsing Flow," *Proceedings of ASME Turbo Expo: Turbine Technical Conference and Exposition*, June 26-30, Charlotte, North Carolina. DOI: <https://doi.org/10.1115/GT2017-63490>

- [24] Sousa, J., and Paniagua, G., 2015, "Entropy Minimization Design Approach of Supersonic Internal Passages," *Entropy*, Vol. 17, pp: 5593-5610. DOI: <https://doi.org/10.3390/e17085593>
- [25] Sousa, J., Paniagua, G., and Saavedra, J., 2017, "Aerodynamic Response of Internal Passages to Pulsating Inlet Supersonic Conditions," *Computers and Fluids*, Vol. 149, No. 13, pp. 31-40. DOI: [10.1016/j.compfluid.2017.03.005](https://doi.org/10.1016/j.compfluid.2017.03.005)
- [26] Sousa, J., Paniagua, G., and Morata, E.C., 2017, "Thermodynamic analysis of a gas turbine engine with a rotating detonation combustor," *Applied Energy*, Vol. 195, pp. 247-256. DOI: <https://doi.org/10.1016/j.apenergy.2017.03.045>
- [27] Paniagua, G., and De'nos, R., 2002, "Digital Compensation of Pressure Sensors in the Time Domain," *Experiments in Fluids*, Vol. 32, pp. 417-424. DOI: <https://doi.org/10.1007/s003480100355>
- [28] Ainsworth, R.W., Milller, R.J., Moss, R.W., and Thorpe, S.J., 2000, "Unsteady Pressure Measurement," *Measurement Science and Technology*, Vol. 11, pp. 1055-1076. DOI: <https://doi.org/10.1088/0957-0233/11/7/319>
- [29] Sieverding, C.H., Arts, T., De'nos, R., and Brouckaert, J.-F., 2000, "Measurement Techniques for Unsteady Flows in Turbomachines," *Experiments in Fluids*, Vol. 28, pp. 285-321. DOI: <https://doi.org/10.1007/s003480050390>
- [30] Bryer, D.W., and Pankhurst, R.C., 1971, "Pressure Probe Methods for Determining Wind Speed and Flow Direction," Her Majesty's Stationary Office, p. 125.
- [31] Dominy, R.G., and Hodson, H.P., 1993, "An Investigation of Factors Influencing the Calibration of Five-Hole Probes for Three-Dimensional Flow Measurements," *Journal of Turbomachinery*, Vol. 115, No. 3, pp. 513-519. DOI: <https://doi.org/10.1115/1.2929281>
- [32] Villafane, L., Yasa T., Paniagua, G., and Bonfanti G., 2011, "Development of Experimental Techniques for the Characterization of Helicoidal Fin Arrays in Transonic Flow Conditions," *Proceedings of the 47th AIAA/ASME/SAE/ASEE Joint Propulsion Conference*, AIAA-2011-6093, San Diego, USA. DOI: <https://doi.org/10.2514/6.2011-6093>

- [33] Delhaye, D., Paniagua, G., Fernandez Oro, J.M., and De´nos, R., 2011, “Enhanced Performance of Fast-Response 3-Hole Wedge Probes for Transonic Flows in Axial Turbomachinery,” *Experiments in Fluids*, Vol. 50, No. 1, pp. 163-177. DOI: <https://doi.org/10.1007/s00348-010-0908-y>
- [34] Hanke, W., Witte, M., Miersch, L., Brede, M., Oeffner, J., Michael, M., Hanke, F., Leder, A., and Dehnhardt, G., 2010, “Harbor seal vibrissa morphology suppresses vortex-induced vibrations,” *The Journal of Experimental Biology*, Vol. 213, pp. 2665-2672. DOI: <https://doi.org/10.1242/jeb.043216>
- [35] Hans, H., Miao, J.M., Triantafyllou, M., and Weymouth, G., 2013, “Whisker-like Geometries and Their Force Reduction Properties,” *MTS/IEEE-OCEANS*, June 10-14, Bergen, Norway. DOI: <https://doi.org/10.1109/OCEANS-Bergen.2013.6608113>
- [36] Kottapalli, A.G.P., Asadnia, M., Miao, J.M., and Triantafyllou, M.S., 2015, “Harbor Seal Whisker Inspired Flow Sensors to Reduce Vortex-Induced Vibrations,” *28th IEEE International Conference on Micro Electro Mechanical Systems*, January 18-22, Estoril, Portugal. DOI: <https://doi.org/10.1109/MEMSYS.2015.7051102>
- [37] Alvarado, P.V., Subramaniam, V., and Triantafyllou, M., 2013, “Performance Analysis and Characterization of Bio-Inspired Whisker Sensors for Underwater Applications,” *IEEE/RSJ International Conference on Intelligent Robots and Systems*, November 3-7, Tokyo, Japan. DOI: <https://doi.org/10.1119/IROS.2013.6697220>
- [38] Beem, H., Hildner, M., and Triantafyllou, M., 2013, “Calibration and validation of a harbor seal whisker-inspired flow sensor,” *Smart Materials and Structures*, Vol. 22, p. 014012. DOI: <https://doi.org/10.1088/0964-1726/22/1/014012>
- [39] Beem, H.R., Triantafyllou, M.S., 2015, “Wake-induced ‘slaloming’ response explains exquisite sensitivity of seal whisker-like sensors,” *Journal of Fluid Mechanics*, Vol. 783, pp. 306-322. DOI: <https://doi.org/10.1017/jfm.2015.513>
- [40] Pai, Y., Prasad, A., Fernandes, R., and Ricklick, M., 2017, “Preliminary Investigation of Bio-Inspired Cylinders for Improved Thermal Performance of Internal Cooling Channels,” *53rd AIAA/SAE/ASEE Joint Propulsion Conference*, July 10-12, Atlanta. DOI: <https://doi.org/10.2514/6.2017-4977>

- [41] Celik, I.B., Ghia, U., and Roache, P.J., 2008, "Procedure for Estimation and Reporting of Uncertainty due to Discretization in CFD Applications," *Journal of Fluids Engineering*, Vol. 130, No. 7, p. 078001. DOI: <https://doi.org/10.1115/1.2960953>
- [42] Clark, J.P., and Grover, E.A., 2007, "Assessing Convergence in Predictions of Periodic-Unsteady Flowfields," *Journal of Turbomachinery*, Vol. 129, No. 4, pp. 740-749. DOI: <https://doi.org/10.1115/1.2720504>
- [43] Klir, G.J., and Yuan, B., 1995, "*Fuzzy Sets and Fuzzy Logic: Theory and Applications*," Prentice-Hall PTR, Upper Saddle River, NJ. DOI: <https://doi.org/10.1021/ci950144a>
- [44] Delery, J., and Dussauge J.-P., 2009, "Some physical aspects of shock wave/boundary layer interactions," *Shock waves*, **19**: 453-468. DOI: <https://doi.org/10.1007/s00193-009-0220-z>
- [45] Sousa, J., Paniagua, G., and Collado-Morata, E., 2017, "Analysis of the aerodynamic losses in a supersonic turbine," *Proceedings of the ASME 2017 Power Conference Joint with ICOPE-17*, June 26-30, Charlotte, NC. DOI: <http://doi.org/10.1115/POWER-ICOPE2017-3624>
- [46] Moeckel, W., 1949, "Approximate method for predicting form and location of detached shock waves ahead of plane or axially symmetric bodies," NACA-TN-1921.
- [47] Stewart, W., 1955, "Analysis of two-dimensional compressible-flow loss characteristics downstream of turbomachine blade row in terms of boundary layer characteristics," NACA-TN-3515.
- [48] Startford, B.S., and Beavers, G.S., 1955, "The Calculation of the Compressible Turbulent Boundary Layer in an Arbitrary Pressure Gradient-A Correlation of certain previous Methods," Aeronautical Research Council Reports and Memoranda, R. & M. No. 3207.
- [49] Kacker, S.C., and Okapuu, U., 1982, "A Mean Line Prediction Method for Axial Flow Turbine Efficiency," *Journal of Engineering for Power*, Vol. 104, No. 1, pp. 111-119. DOI: <https://doi.org/10.1115/1.3227240>
- [50] Pinilla, V., Solano, J.P., Paniagua, G., and Anthony, R.J., 2012, "Adiabatic Wall Temperature Evaluation in a High Speed Turbine," *Journal of Heat Transfer*, Vol. 134, No. 9, pp. 091601. DOI: <https://doi.org/10.1115/1.4006313>

- [51] Roy, C.J., McWherter-Payne, M.A., and Oberkampf, W., 2003, "Verification and Validation for Laminar Hypersonic Flowfields, Part 1: Verification", *AIAA Journal*, Vol. 41, No. 10, pp. 1934-1943. DOI: <https://doi.org/10.2514/2.1909>
- [52] Lee, J., Tan, C.S., Sirakov, B.T., Im, H-S., Babak, M., Tisserant, D., and Wilkins, C., 2017, "Performance Metric for Turbine Stage Under Unsteady Pulsating Flow Environment," *Journal of Engineering for Gas Turbines and Power*, Vol. 139, No. 7, p. 072606. DOI: <https://doi.org/10.1115/1.4035630>
- [53] Horlock, J.H., 1960, "Losses and Efficiencies in Axial-Flow Turbines," *International Journal of Mechanical Sciences*, Vol. 2, No. 1-2, pp. 48-75. DOI: [https://doi.org/10.1016/0020-7403\(60\)90013-8](https://doi.org/10.1016/0020-7403(60)90013-8)
- [54] Traupel. W., 1977, *Temische Turbomaschinen Zweiter Band Gelanderte Betriebsbedingungen, Regelung, Mechanische Probleme, Temperaturprobleme*, Springer-Verlag Berlin heidelberg New York
- [55] Denton, J D., 1993, "Loss Mechanisms in Turbomachines," *Journal of Turbomachinery*, Vol. 155, No. 4, pp. 621-656. DOI: <https://doi.org/10.1115/1.2929299>
- [56] Juangphanich, P., Maesschalck, C.D., and Paniagua, G., 2019, "Turbine Passage Design Methodology to Minimize Entropy Production-A Two-Step Optimization Strategy." *Entropy*, Vol. 21, No. 6, p. 604. DOI: <https://doi.org/10.3390/e21060604>
- [57] Verstraete, T.T., Alsalihi, Z.Z., and Van den Braembussche, R.A., 2010, "Multidisciplinary Optimization of a Radial Compressor for Microgas Turbine Applications," *Journal of Turbomachinery*, Vol. 132, No. 3, p. 031004. DOI: <https://doi.org/10.1115/1.3144162>
- [58] Denos, R., Arts, T., Paniagua, G., Michelassi, V., and Martelli, F., 2000, "Investigation of the Unsteady Rotor Aerodynamics in a Transonic Turbine Stage," *Journal of Turbomachinery*; Vol. 123, No. 1, pp. 81-89. DOI: <https://doi.org/10.1115/1.1314607>
- [59] Sieverding, C.H., Arts, T., Denos, R., and Martelli, F., 1996, "Investigation of the Flow Field Downstream of a Turbine Trailing Edge Cooled Nozzle Guide Vane," *Journal of Turbomachinery*, Vol. 118, pp. 291-300. DOI: <https://doi.org/10.1115/1.2836639>

- [60] Denos, R., Sieverding, C.H., Arts, T., Brouckaert, J.F., Paniagua, G., and Michelassi, V., 1999, "Experimental investigation of the unsteady rotor aerodynamics of a transonic turbine stage," *Proceedings of the Institution of Mechanical Engineers, Part A: Journal of Power and Energy*, Vol. 213, No. 4, pp. 327-338. DOI: <https://doi.org/10.1243/0957650991537653>
- [61] Yasa, T., Paniagua, G., and Bussolin, A., 2007, "Performance analysis of a transonic high-pressure turbine," *Proceedings of the Institution of Mechanical Engineers, Part A: Journal of Power and Energy*, Vol. 221, No. 6, pp. 769-778. DOI: <https://doi.org/10.1243/09576509JPE467>
- [62] Montgomery, D.C., 1997, "*Design and Analysis of Experiments*," John Wiley and Sons, New York, ISBN978-1118146927
- [63] Deb, K., 2002, "A Fast and Elitist Multiobjective Genetic Algorithm: NSGA-II", *IEEE Transactions on Evolutionary Computation*, Vol. 6, No. 3, pp. 182-197. DOI: <https://doi.org/10.1109/4235.996017>
- [64] Chapman, J., Lavelle, T., May, R., Litt, J., and Guo, T., 2014, Toolbox for the Modeling and Analysis of Thermodynamic Systems (T-MATS) User's Guide, NASA/TM-2014-216638.
- [65] Paniagua, G., Cuadrado, D.G., Saavedra, J., Andreoli, V., Meyer, T., Solano, J.P., Herrero, R., Meyer, and S., Lawrence, D., 2019, "Design of the Purdue Experimental Turbine Aerothermal Laboratory for Optical and Surface Aerothermal Measurements," *Journal of Engineering for Gas Turbines and Power*, Vol. 141, No. 1, p. 012601. DOI: <https://doi.org/10.1115/1.4040683>
- [66] Saavedra, J, Paniagua, G., and Saracoglu, B.H., 2017, "Experimental Characterization of the Vane Heat Flux Under Pulsating Trailing Edge Blowing," *Journal of Turbomachinery*, Vol. 139, No. 6, p. 061004. DOI: <https://doi.org/10.1115/1.4035211>
- [67] Naughton, J., and Brown, J., 1996, "Surface Interferometric Skin-Friction Measurement Technique," *19th AIAA Advanced Measurement and Ground Testing Technology Conference*, June 17-20, New Orleans, LA. DOI: <https://doi.org/10.2514/6.1996-2183>

- [68] Bergh, H., and Tijdeman, H., 1965, "Theoretical and Experimental Results for the Dynamic Response of Pressure Measuring Systems," Netherlands National Aero- and Astronautical Research Institute, Report NLR-TR F.238
- [69] Bhatnagar, L., and Paniagua, G., 2019, "Development of High Speed and High Temperature Atomic Layer Thermopiles," *Proceedings of ASME 2019 Turbo Expo: Turbomachinery Technical Conference & Exposition*, June 17-21, Phoenix, AZ. GT2019-91012
- [70] Fisher, J., Smyser, M.E., Meyer, T.R., Slipchenko, M., Caswell, A.W., Gord, J., and Roy, S., 2019, "Burst-Mode 100 kHz – 1 MHz Velocimetry in Supersonic and Hypersonic Flows," *AIAA SciTech Forum*, January 7-11, San Diego, CA. DOI: <https://doi.org/10.2514/6.2019-1822>
- [71] Richter, A., and Naudascher, E., 1976, "Fluctuating Forces on a Rigid Circular Cylinder in Confined Flow," *Journal of Fluid Mechanics*, Vol. 78, No. 3, pp. 561-576. DOI: <https://doi.org/10.1017/S0022112076002607>
- [72] Whitmore, S.A., and Leondes, C.T., 1991, "Pneumatic Distortion Compensation for Aircraft Surface Pressure Sensing Devices," *Journal of Aircraft*, Vol. 28, No. 12, pp: 828-836. DOI: <https://doi.org/10.2514/3.46105>
- [73] Yasa, T., and Paniagua, G., 2012, "Robust Procedure for Multi-hole Probe Data Processing," *Flow Measurement and Instrumentation*, Vol. 26, pp. 46-54. DOI: <https://doi.org/10.1016/j.flowmeasinst.2012.03.004>
- [74] Chakravarthy, S., Peroomian, O., Goldberg, U., and Palaniswamy, S., 1998, "The CFD++ Computational Fluid Dynamics Software Suite", *AIAA and SAE, World Aviation Conference*, Anaheim, CA. DOI: <https://doi.org/10.2514/6.1998-5564>
- [75] McBride B.J., Gordon S., and Reno M. 2001, "Thermodynamic Data for Fifty Reference Elements", NASA Technical Memorandum 3287/REV1, February. <https://www.grc.nasa.gov/www/CEAWeb/TP-3287-REV1.pdf>
- [76] Paniagua, G., Yasa, T., De La Loma, A., Castillon, L., and Coton, T., 2008, "Unsteady Strong Shocks Interactions in a Transonic Turbine: Experimental and Numerical Analysis," *Journal of Propulsion and Power*, Vol. 24, No. 4, pp. 722-731. DOI: <https://doi.org/10.2514/1.34774>

- [77] Schulein, E., Krogmann, P., and Stanewsky, E., 1996, "Documentation of two-dimensional impinging shock/turbulent boundary layer interaction flow," DLR Report DLR IB 223-96 A 49.
- [78] Schulein, E., 2004, "Optical Skin Friction Measurements in Short-duration Facilities (Invited)," *24th AIAA Aerodynamic Measurement Technology and Ground Testing Conference*, June 28-July 1, Portland, Oregon. DOI: <https://doi.org/10.2514/6.2004-2115>

APPENDIX. SOLVER VALIDATION

Reduced Frequency

The reduced frequency defined in Equation (0.3) was utilized to evaluate how fast the flow properties travel through the stator passage and is quantified by the inlet axial velocity, with respect to the speed of the propagating fluctuations from the upstream diffuser. In Equation (0.1), the axial velocity was first mass-flow-averaged on all cells (n) at each time instant. Afterwards, Equation (0.1) was substituted into Equation (0.2) for a cycle-mass-averaged evaluation over a selected pulsating period (t), which was plugged into Equation (0.3) for the final evaluation of the reduced frequency. In all figures, the reduced frequency is plotted in logarithmic scale.

$$\bar{V}_{ax_in}(t) = \frac{\sum_{i=1}^n V_{ax_in}(t)\rho_i |\overrightarrow{V_{ax_i}} \cdot \overrightarrow{S_i}|}{\sum_{i=1}^n \rho_i |\overrightarrow{V_{ax_i}} \cdot \overrightarrow{S_i}|} \quad (0.1)$$

$$V_{ax_in} = \frac{\int_0^t m(t)\bar{V}_{ax_in}(t)dt}{\int_0^t m(t)dt} \quad (0.2)$$

$$\bar{f} = \frac{f}{V_{1_ax}/C_{ax_S}} \quad (0.3)$$

CFD++

In the transonic and supersonic applications, three-dimensional unsteady Reynolds-Averaged Navier-Stokes (URANS) simulations were performed with the commercial solver CFD++ of Metacomp Technologies. The three-dimensional compressible real gas Navier-Stokes equations implemented in CFD++ [74] are expressed as

$$\frac{\partial Q}{\partial t} + \frac{\partial(F_1+G_1)}{\partial x} + \frac{\partial(F_2+G_2)}{\partial y} + \frac{\partial(F_3+G_3)}{\partial z} = \dot{S} \quad (0.4)$$

Where Q denotes the dependent variable vector, F represents the inviscid flux vectors, and G is the viscous flux vector:

$$Q = \begin{pmatrix} e \\ \rho \\ \rho u \\ \rho v \\ \rho w \end{pmatrix} F1 = \begin{pmatrix} u(e+p) \\ \rho u \\ \rho u^2 + p \\ \rho v u \\ \rho w u \end{pmatrix} F2 = \begin{pmatrix} v(e+p) \\ \rho v \\ \rho u v \\ \rho v^2 + p \\ \rho w v \end{pmatrix} F3 = \begin{pmatrix} w(e+p) \\ \rho w \\ \rho u w \\ \rho v w \\ \rho w^2 + p \end{pmatrix} \quad (0.5)$$

Where τ represents the shear stress vector, and q denotes the heat flux vector:

$$t_{xx} = 2\bar{\mu}_m \frac{\partial u}{\partial x} - \frac{2}{3}\bar{\mu}_m \phi \quad (0.6)$$

$$t_{yy} = 2\bar{\mu}_m \frac{\partial v}{\partial y} - \frac{2}{3}\bar{\mu}_m \phi \quad (0.7)$$

$$t_{zz} = 2\bar{\mu}_m \frac{\partial w}{\partial z} - \frac{2}{3}\bar{\mu}_m \phi \quad (0.8)$$

$$t_{xy} = t_{yx} = \bar{\mu}_m \left(\frac{\partial u}{\partial y} + \frac{\partial v}{\partial x} \right) \quad (0.9)$$

$$t_{xz} = t_{zx} = \bar{\mu}_m \left(\frac{\partial u}{\partial z} + \frac{\partial w}{\partial x} \right) \quad (0.10)$$

$$t_{yz} = t_{zy} = \bar{\mu}_m \left(\frac{\partial w}{\partial y} + \frac{\partial v}{\partial z} \right) \quad (0.11)$$

$$\phi = \left(\frac{\partial u}{\partial x} + \frac{\partial v}{\partial y} + \frac{\partial w}{\partial z} \right) \quad (0.12)$$

$$\dot{q}_x = -\bar{k}_m \frac{\partial T}{\partial x} \quad (0.13)$$

$$\dot{q}_y = -\bar{k}_m \frac{\partial T}{\partial y} \quad (0.14)$$

$$\dot{q}_z = -\bar{k}_m \frac{\partial T}{\partial z} \quad (0.15)$$

Where \bar{k}_m denotes the thermal conductivity. The thermodynamic properties were evaluated based on a real gas model with a temperature-dependent coefficient polynomial for working fluid with the coefficients found in Bride et al.[75]. The Sutherland Law was utilized to estimate the viscosity. Table 1 lists the values of temperature-dependent parameters for air.

Table 0.1: Sutherland law parameters for viscosity and thermal conductivity of air.

	T_{ref}	$\sigma_{\text{viscosity,ref}}$	$C_{\text{viscosity}}^{\text{te}}$	k_{ref}	$C_{\text{thermal conductivity}}^{\text{te}}$
Air	273.11	1.716e-5	111.0	0.0241	194.0

In the first case, a validation of CFD++ was carried out on a transonic turbine. The turbine geometry and boundary conditions were obtained from [76]. The k- ω SST was employed as the turbulence model, with a y^+ lower than 1. The mid-span flow field is illustrated in Fig. 5.1a, characterized by strong trailing edge shocks. Figure 5.2b depicts the mid-span isentropic Mach number distribution. The discrepancy in terms of the location of the shock impingement between the CFD++ prediction and the experimental evidence is less than 0.3%

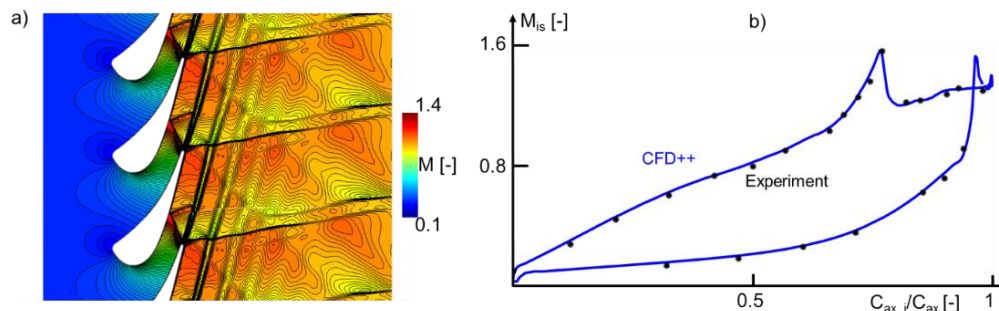


Figure 0.1. At mid-span: a) the Mach contour of the transonic vane. b) Isentropic Mach number distribution.

In the second case, a validation of CFD++ was performed on a Mach 5 ramp with shock-boundary layer interaction. The ramp is 300 mm long with a 10 degrees deflection angle, which induced an oblique shock impinging on a 500 m flat plate. Wall temperature was maintained at 300K. Figure 5.2a displays the computed Mach contour, where an oblique shock reflection was generated due to the top concave corner. Figure 5.2b depicts the comparison of the skin friction coefficient of the bottom wall between CFD++ and the experiments [77][78]. The CFD predicts the separation location with 1.4% discrepancy of the experimental evidence [78]. Figure 5.2c shows a good agreement of the wall static pressure between CFD and experiments.

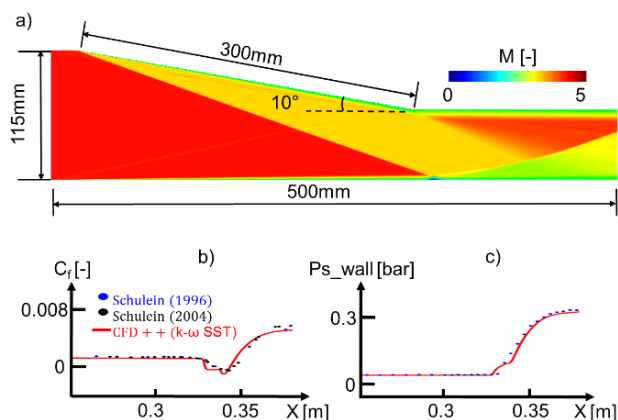


Figure 0.2. a) Steady Mach contour. b) Comparison of skin friction and c) wall static pressure.

ANSYS Fluent

In the subsonic applications, URANS simulations were performed with the density-based solver ANSYS Fluent. The solver was validated against experimental data to replicate the acoustic phenomena in the recessed sensors. The experiments were performed in the Office National d'Etudes et de Recherches Aeronautiques (ONERA) shock tube tunnel in Lille, shown in Fig. 5.3a. Tests were run with orifice lengths of 0.6 and 1.7 mm for several-hole diameters. The recessed pressure sensor is mounted side by side with a flush-mounted reference sensor on the end-plate of the low-pressure chamber of the shock tube [27]. Figure 5.3b displays the numerical grid of the shock tube, with a snapshot of the schematic sketch of the line-cavity configuration. The length of the cavity is 0.05mm. The driver zone was set at 5bar and at 1bar in the driven zone. Figure 5.3c depicts the normalized pressure evaluated via Equation (0.16), retrieved from the reference sensor and recessed sensor. Utilizing the system identification, the resonance frequency of the attached tube-cavity system could be identified. The resonance frequency of each tube-cavity configuration was evaluated and summarized in Fig. 5.3d. Numerical results were compared with experimental data [27] and prediction from two analytical models: Bergh-Tijdeman [68] and Whitmore-Leondes [72]. At high L/D ratios (L=1.7mm), discrepancies between numerical results and experimental data are observed for the hole diameter ranging between 0.35 and 0.48mm, with a maximum of 28.4%. At a diameter of 0.25mm and 0.6mm, the numerical predictions agree very well with experiments. In addition, the numerical results indicate that resonant frequency seems to be locked around 38 kHz with the diameter ranging between 0.35 and 0.6 mm. At low L/D ratios (L=0.6mm), the numerical results generally follow the trend of experimental data. Both numerical and experimental results fluctuate around 80 kHz. Theoretical values predicted by analytical models generally underestimate the numerical and experimental results. The Bergh-Tijdeman [68] model was developed for high L/D ratios with the assumption of negligible non-linear effect and laminar flow. However, in our investigated cases, a strong shock wave was induced due to the large initial pressure ratio, which resulted in non-linear post-shock disturbances in the shock tube. Whitmore-Leondes [72] model assumed that the tube volume was comparable to the cavity volume, which is not suitable for cases with small hole diameter.

$$P_{norm} = \frac{P_s - P_{s_initial}}{P_{s_final} - P_{s_initial}} \quad (0.16)$$

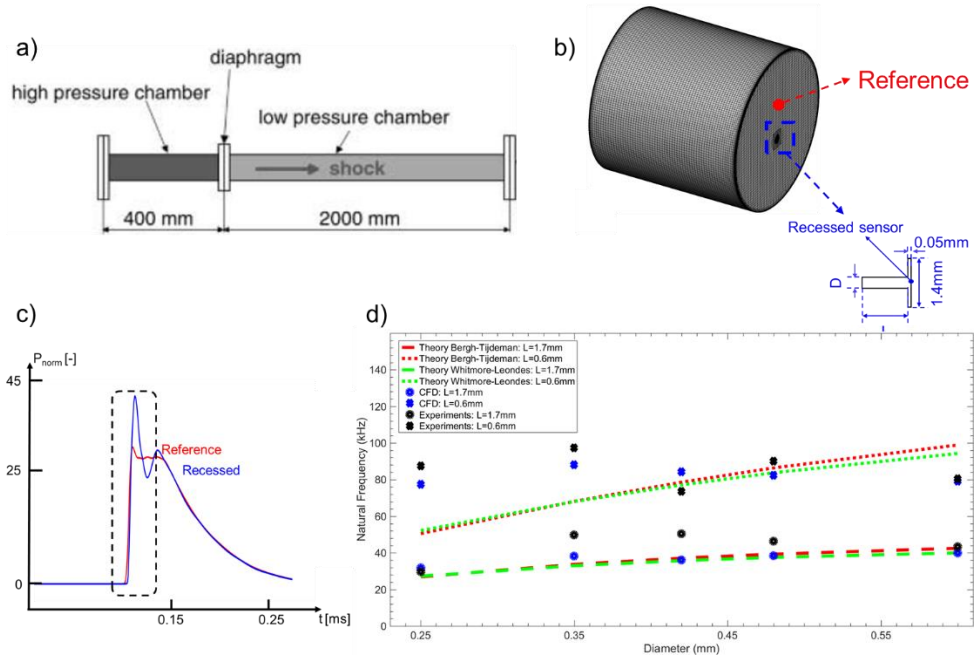


Figure 0.3. a) ONERA shock tube [27]. b) Numerical grid of the shock tube with a zoomed view of line-cavity schematic sketch. c) Normalized pressure from the reference and recessed sensor. d) Resonance frequency of different tube-cavity configurations.

PERMISSION LETTER

Elsevier has granted the permission to reuse Figure 9 on page 50 from Paniagua, G and Yasa, T., 2012, "Robust procedure for multi-hole probe data processing," Flow Measurement and Instrumentation, Vol. 26. License number: 4716031437340.

Springer Nature has granted the permission to reuse Figure 10 on page 423 from Paniagua, G and Denos, R., 2002, "Digital compensation of pressure sensors in the time domain," Experiments in Fluids, Vol. 32. License number: 4716031038122.

ASME has granted the permission to republish most contents from Liu, Z., Braun, J., and Paniagua, G., 2019, "Characterization of a Supersonic Turbine Downstream of a Rotating Detonation Combustor," Journal of Engineering for Gas Turbines and Power, Vol. 141. License number: 1007521-1.

ASME has granted the permission to republish most contents from Liu, Z., and Paniagua, G., 2018, "Design of Directional Probes for High-Frequency Turbine Measurements," Journal of Engineering for Gas Turbines and Power, Vol. 140. License number: 1007524-1.

ASME has granted the permission to republish most contents from Liu, Z., Inhestern, L.B., Braun, J., and Paniagua, G., 2019, "Unsteady Heat Transfer Assessment of Supersonic Turbines Downstream of a Rotating Detonation Combustor," Proceedings of ASME Turbo Expo 2019: Turbomachinery Technical Conference and Exposition, June 17-21, Phoenix, AZ. Paper No: GT2019-91460. License number: 1007525-1.

VITA

Zhe Liu was graduated from Donghua University (China Textile University) in 2013 with a Bachelor degree in built environment and HVAC engineering. Afterwards, he landed in United States to pursue a Master of Science degree in mechanical engineering at Columbia University. In Fall 2015, he was enrolled in the mechanical engineering PhD program at Purdue University and performed research at Zucrow Laboratories.

PUBLICATIONS

Patents

1. Paniagua, G., Cuadrado, D.G., Braun, J., Andreoli, V., Liu, Z., “Directional Probe for High Temperature Flows,” United States Provisional Application; 68020-01; 62/571774

Archival Journal Papers

1. Liu, Z., Braun, J., and Paniagua, G., 2019, “Characterization of a Supersonic Turbine Downstream of a Rotating Detonation Combustor,” *Journal of Engineering for Gas Turbines and Power*, Vol. 141, No. 3, p. 031501. DOI: <https://doi.org/10.1115/1.4040815>
2. Liu, Z., and Paniagua, G., 2018, “Design of Directional Probes for High-Frequency Turbine Measurements,” *Journal of Engineering for Gas Turbines and Power*, Vol. 140, No. 1, p. 011601. DOI: <https://doi.org/10.1115/1.4037640>

Peer Reviewed Conference Papers

1. Liu, Z., Inhestern, L.B., Braun, J., and Paniagua, G., 2019, “Unsteady Heat Transfer Assessment of Supersonic Turbines Downstream of a Rotating Detonation Combustor,” *Proceedings of ASME Turbo Expo 2019*, June 17-21, Phoenix, AZ.
2. Liu, Z., Braun, J., and Paniagua, G., 2018, “Characterization of a Supersonic Turbine Downstream of a Rotating Detonation Combustor,” *Proceedings of ASME Turbo Expo 2018*, June 11-15, Lillestrom, Norway. DOI: <https://doi.org/10.1115/GT2018-76798>
3. Liu, Z., and Paniagua, G., 2017, “Design of Directional Probes for High-Frequency Turbine Measurements,” *Proceedings of ASME Turbo Expo 2017*, June 26-30, Charlotte, NC. DOI: <https://doi.org/10.1115/GT2017-64680>

Conference Proceedings

1. Braun, J., Liu, Z., Cuadrado, D., Andreoli, V., Paniagua, G., Saavedra, J., Athmanathan, V., and Meyer, T., 2019, “Characterization of an integrated nozzle and supersonic axial turbine with a rotating detonation combustor,” *Proceedings of 2019 Propulsion and Energy Forum*, August 19-22, Indianapolis, IN. DOI: <https://doi.org/10.2514/6.2019-3873>

2. Liu, Z., Saavedra, J., Braun, J., and Paniagua, G., 2019, "Numerical analysis on the performance of CTAP measurements in pulse and rotating detonation combustors," *Proceedings of 2019 Propulsion and Energy Forum*, August 19-22, Indianapolis, IN. DOI: <https://doi.org/10.2514/6.2019-4378>
3. Bhatnagar, L., Braun, J., Andreoli, V., Cuadrado, D.G., Liu, Z., and Paniagua, G., 2018, "Developments in High Frequency Directional Probes for High Temperature Applications," *Proceedings of XXIV Biennial Symposium on Measuring Techniques in Turbomachinery*, August 29-31, Prague, Czech Republic
4. Liu, Z., Braun, J., and Paniagua, G., 2018, "Three Dimensional Optimization for Subsonic Axial Turbines Operating at High Unsteady Inlet Mach Number," *Proceedings of 2018 Propulsion and Energy Forum*, July 9-11, Cincinnati, OH. DOI: <https://doi.org/10.2514/6.2018-4480>
5. Liu, Z., Braun, J., and Paniagua, G., 2017, "Performance of axial turbines exposed to large fluctuations," *Proceedings of 2017 Propulsion and Energy Forum*, July 10-12, Atlanta, GA. DOI: <https://doi.org/10.2514/6.2017-4817>
6. Liu, Z., and Paniagua, G., 2016, "On the ability of conventional aerodynamic probes to resolve high frequency phenomena," *Proceedings of XXIII Biennial Symposium on Measuring Techniques in Turbomachinery*, September 1-2, Stuttgart, Germany
7. Liu, Z., and Akbari, P., 2015, "Performance Analysis and Modeling of the Two-Stage Wave Disk Engine," *Proceedings of the 1st Thermal and Fluids Engineering Conference*, August 9-12, New York, NY. DOI: <https://doi.org/10.1615/TFESCI.asp.012761>